PRODUCTION AND STRUCTURAL CHARACTERIZATION
OF
IRON-BORON NANOALLOYS

A THESIS SUBMITTED TO
THE GRADUATE SCHOOL OF APPLIED AND NATURAL SCIENCES
OF
MIDDLE EAST TECHNICAL UNIVERSITY

BY

AMIR FADAIE

IN PARTIAL FULFILLMENT OF THE REQUIREMENTS
FOR
THE DEGREE OF MASTER OF SCIENCE
IN
METALLURGICAL AND MATERIALS ENGINEERING

JANUARY 2014

Approval of the thesis:

**PRODUCTION AND STRUCTURAL CHARACTERIZATION
OF
IRON-BORON NANOALLOYS**

submitted by **AMIR FADAIE** in partial fulfillment of the requirements for the degree of **Master of Science in Metallurgical and Materials Engineering Department, Middle East Technical University** by,

Prof. Dr. Canan Özgen

Dean, Graduate School of **Natural and Applied Sciences**

Prof. Dr. Hakan C. GÜR
Head of Department, **Metallurgical and Materials Engineering**

Prof. Dr. Amdulla Mekhrabov
Supervisor, **Metallurgical and Materials Eng. Dept., METU**

Prof. Dr. M. Vedat Akdeniz
Co-Supervisor, **Metallurgical and Materials Eng. Dept., METU**

Examining Committee Members:

Prof. Dr. Bilgehan Ögel
Metallurgical and Materials Engineering Dept., METU

Prof. Dr. Amdulla O. Mekhrabov
Metallurgical and Materials Engineering Dept., METU

Prof. Dr. M. Vedat Akdeniz
Metallurgical and Materials Engineering Dept., METU

Assist. Prof. Dr. Mert Efe
Metallurgical and Materials Engineering Dept., METU

Assist. Prof. Dr. İlkay Saltoğlu Kalay
Materials Science and Engineering Dept., Çankaya Univ.

Date: 28.01.2014

I hereby declare that all information in this document has been obtained and presented in accordance with academic rules and ethical conduct. I also declare that, as required by these rules and conduct, I have fully cited and referenced all material and results that are not original to this work.

Name, Last name: Amir Fadaie

Signature:

ABSTRACT

PRODUCTION AND STRUCTURAL CHARACTERIZATION

OF

IRON-BORON NANOALLOYS

Fadaie, Amir

M.Sc., Department of Metallurgical and Materials Engineering

Supervisor: Prof. Dr. Amdulla Mekhrabov

Co-Supervisor, Prof. Dr. M. Vedat Akdeniz

January 2014, 120 pages

The purpose of this study was production and structural characterization of Fe-B crystalline /amorphous nanocomposite powders.

In the theoretical part of the study, detailed nanoscale structures of $Fe_{80}B_{20}$ and $Fe_{85}B_{15}$ metallic glasses were investigated using Molecular Dynamics (MD) method as well as several structural analysis tools.

In the experimental part of the study, $Fe_{80}B_{20}$ and $Fe_{85}B_{15}$ crystalline /amorphous nanocomposite powders have been synthesized by using surfactant-assisted high-energy ball milling. Then these powders have been examined using X-ray diffraction (XRD), Scanning Electron Microscopy (SEM), Differential Scanning Calorimetry (DSC) and Vibrating Sample Magnetometer (VSM).

Comparisons have been made for the differences between evolved microstructures via equilibrium solidification, non-equilibrium solidification and solid-state phase transformations during milling operations.

Structural analysis revealed that initially observed Fe_2B and Fe_3B intermetallic phases tend to disappear even at 1-hour milling time and eventually lead to the stabilization of α-Fe nanoparticles and possible formation of amorphous phase by increasing milling time. This resultant structure governs the magnetic behavior of the $Fe_{80}B_{20}$ and $Fe_{85}B_{15}$ nanoalloys.

Keywords: Molecular Dynamics Method, High-Energy Ball Milling, Surfactants.

ÖZ

Fe-B NANOALAŞIMININ ÜRETİLMESİ VE YAPISAL ÖZELLİKLERİNİN BELİRLENMESİ

Fadaie, Amir

Y. Lisans, Metalürji ve Malzeme Mühendisliği Bölümü

Tez Yöneticisi: Prof. Dr. Amdulla Mekhrabov

Ortak Tez Yöneticisi, Prof. Dr. M. Vedat Akdeniz

Ocak 2014, 120 sayfa

Bu çalışmanın amacı kristal/camsı nanokompozit Fe-B tozlarının üretilmesi ve yapısal özelliklerinin belirlenmesidir.

Çalışmanın teorik kısmında, $Fe_{80}B_{20}$ ve $Fe_{85}B_{15}$ metalik camlarının nanoölçekteki yapılarının ayrıntıları Moleküler Dinamik (MD) yöntemi ve çeşitli yapısal analiz araçları kullanılarak incelenmiştir.

Çalışmanın deneysel kısmında, kristal/camsı $Fe_{80}B_{20}$ ve $Fe_{85}B_{15}$ nanokompozit tozlar yüzey etken madde yardımıyla yüksek enerjili bilye öğütümü yöntemi ile üretilmiştir. Daha sonra bu tozlar X-ışını Kırınımı (XRD), Taramalı Elektron Mikroskobu (SEM), Diferansiyel Taramalı Kalorimetre (DSC) ve Titreşimli Örnek Manyetometresi (VSM) kullanılarak incelenmiştir.

Denge katılaşması, dengedışı katılaşma ve öğütme sırasındaki katı hal faz dönüşümleri ile ortaya çıkan mikroyapılar arasındaki farklılıklar karşılaştırılmıştır. Yapısal analizler ilk başta gözlemlenen Fe_2B and Fe_3B intermetalik fazların daha 1 saatlik öğütmenin ardından yokolma eğiliminde olduğunu ve öğütme işleminin sonunda α-Fe nanoparçacıklarının kararlı hale gelmesine ve muhtemelen camsı faz

oluşumuna yol açtığını ortaya çıkarmıştır. Ortaya çıkan bu yapı $Fe_{80}B_{20}$ and $Fe_{85}B_{15}$ nanoalaşımlarının manyetik davranışını etkilemektedir.

Anahtar Kelimeler: Moleküler Dinamik Yöntemi, Yüksek Enerjili Bilye Öğütümü Yöntemi, Yüzey Etken Maddeler.

مادر ای روح خدا

مظهر حق روی زمین

مستر و مستانگر

هم عاشق، هم شمع و پروانه ای

تو امید خانه ای

تو امید هر نفر

تو امید بودن

مونس شبهای سخت

مرهم دردهای تلخ

من چه گویم تا شود لایق تو را

گر نابود در آن خدا

سجده میکردم تو را

اما پدر

هم تو امیدی، هم جلوه قدرت

تو کوه، استواری

ایستاده بر بام زندگی

تو علمدار زندگی

امیر - آنکارا

ix

ACKNOWLEDGEMENTS

I would like to express my sincere appreciation and gratitude to my supervisor, Prof. Dr. Amdulla Mekhrabov and co-supervisor, Prof. Dr. M. Vedat Akdeniz for patiently sharing their extensive wisdom, kind and endless support, continuous guidance and motivation throughout this thesis study.

I cannot adequately express my gratitude and thankfulness to my dear family members Ali Fadaie, Parvin Abdolrahimpour, Saba and Behzad Fadaie for their love, support, patience and being there for me throughout my whole life. I would also like to thank Tufan Güngören and Muratahan Aykol, for their useful suggestions and comments, which allowed me to improve my work throughout this study.

I shall not forget Yashar Fallah Vazirabad, Behnoosh Amandi, Pourng Ezzetfar, Maryam Daneshvar, Farnaz Solatikiya, Mahdi Ghaffarinia, Şükrü Kılık, Burcu Güleryüz and Ehsan Sakhtemansaz to whom I must thank for being the best friends who offered sincere help and encouragement when I needed the most.

I must express my special thanks to my co-workers and friends Mehmet Yıldırım, Mahsuni Yalçın, Bengi Yağmurlu, Saeid Pournaderi, Nagehan Duman, Mine Kalkancı, and Mehmet Ali Recai Önal for their continuous support and motivation during our long hours in the laboratory.

Exhaustion plays havoc on memory; my humblest apologies to those whom I might have forgotten to name.

<div align="right">
Ankara

January 2014
</div>

TABLE OF CONTENTS

LIST OF FIGURES

FIGURES

xvii

LIST OF TABLES

TABLES

CHAPTER 1

INTRODUCTION AND LITERATURE REVIEW

1.1. General Aspects

1.1.1. Clusters

Clusters (or nanoparticles) are aggregates of atoms or molecules, which may contain either a few or many millions of them. The atom or molecules within a cluster may be identical, or different types of atoms or molecules may co-exist in the cluster. Clusters can be examined in different media, such as colloidal suspensions, vapor phase, molecular beams, and isolates either in inert matrices or on surfaces (Haberland, 1994, Baletto and Ferrando, 2005, Johnston, 2002, Martin, 1996).

Clusters can be regarded as a new type of material with potential properties different from both the atoms/molecules and the bulk material. That's why there is growing interest on clusters. The size-dependent evolution of cluster properties, (Jortner, 1992, Johnston, 1998) such as their structure, is one important reason for the interest.

The geometric shape and the energetic stability may indeed strongly depend on the cluster size. For instance, clusters of alkali-metal atoms (up to thousands of atoms) and smaller clusters of copper and silver are known to obey the jellium model, with regards to certain nuclearities (the so-called magic sizes), are relatively stable owing to their filled electronic shells (Baletto and Ferrando, 2005, de Heer, 1993).

1

However, transition metals and some main-group metals, such as aluminum, calcium and strontium, form clusters with magic sizes corresponding to clusters consisting of nested shells of atoms, where the competition between packing and surface energy effects determines the relative stability of a given cluster (Baletto and Ferrando, 2005, Martin, 1996).

The interest in metal clusters continues due to potential applications in catalysis, nanoelectronic and others (Johnston, 2002).

1.1.2. Nanoalloys

Materials scientists mix elements to form intermetallic compounds and alloys in order to extend the range of properties of the presently available metallic systems. Specific properties can be enhanced by alloying due to synergistic effects of different elements. The variation of compositions, structures, and properties of metallic alloys has led to novel applications in electronics, catalysis and in every field of engineering. There is growing interest in alloy nanoclusters or nanoalloys. The interest is focused on developing new materials with controllable properties and nanometer scale structures, and fueled by the flexibility given by intermetallic materials.

In making alloys, bulk or nanoalloy, there are many combinations and compositions that are possible. Bimetallic nanoalloys (A_mB_n) can be generated with controlled composition (m/n) and size (m+n). The cluster-making method (particularly the form of cluster source) and experimental conditions, such as temperature, pressure, may influence the cluster structures and the degree of mixing or segregation. As mentioned before, nanoalloy clusters can be made in different media, such as colloidal suspensions, molecular beams, on surfaces and even inside of pores.

The chemical and physical properties of alloy nanoparticles may be tuned by varying the composition and atomic ordering as well as the size of the clusters. This probably is the main reason for interest in them. In nanoalloys there are not only specific sizes but also specific compositions at which the nanoclusters are especially more stable. That's why these stable sizes and compositions are sometimes called magic sizes and magic compositions. Surface structures, compositions, and segregation properties

(Ruban et al., 1999, Bozzolo et al., 1999) of nanoalloys are of interest as In nanoalloys, the structures and compositions on the surfaces, and segregation (Ruban et al., 1999, Bozzolo et al., 1999) are important in determining chemical reactivity, in particular, the catalytic activity (Schmid, 1999, Molenbroek et al., 1998).

Nanoalloys have the potential to present structures and properties so much different than those displayed by the pure elemental clusters. Binary clusters may show structures quite different from those observed in pure clusters of the same size, as in synergism is in catalysis by bimetallic nanoalloys. Due to finite size effects, nanoalloys may also present properties very different from the corresponding bulk alloys. For example, iron and silver are immiscible in bulk alloys; however, they readily mix in finite clusters (Andrews and O'Brien, 1992).

1.1.3. Isomerism in Nanoalloys

The energy landscapes of nanoalloys are complicated, which presents a fascinating challenge from theoretical point of view. Compared to pure metal clusters, bimetallic nanoalloy clusters presents higher complexity simply because there are two different kinds of atoms. In addition to the regular geometrical isomers (with different geometric structures), this makes it possible to have isomers based on the permutation of unlike atoms. $A_m B_n$ alloy cluster structures with a fixed number of atoms (N=m + n) and composition (m/n ratio) are described by the term "homotops" where the atoms in clusters are arranged geometrically the same way but A- and B-type atoms are arranged differently (Jellinek and Krissinel, 1996, Krissinel and Jellinek, 1997b, Krissinel and Jellinek, 1997a).

As the cluster size increases, the number of different combinations possible that A and B atoms increases drastically. That's why global optimization of geometrical isomers and homotops gets extremely difficult.

A single geometrical isomer of an AB cluster of N atoms will generate homotops,

$$^{N}P_{A,B} = \frac{N!}{N_A! N_B!} = \frac{N!}{N_A!(N-N_A)!} \qquad \text{Equation 1}$$

3

where N_A and N_B are the number of A- and B- atoms, respectively, and N is the total number of atoms ($N = N_A + N_B$). In this relation, point group symmetry is ignored.

To illustrate the huge number of homotops by only 20 atoms, there are 184756 homotops generated by an $A_{10}B_{10}$ cluster; however, one should note that many of these might be equivalent symmetrically. For a given structural isomer of any composition, there are 2^N homotops. This yields roughly 10^6 homotops for a 20-atom cluster.

There are also compositional isomers, having the same number of atoms ($N = N_A + N_B$) and geometrical structure but different compositions (N_A / N_B). They are term as "composomers" (Lordeiro et al., 2003) , in addition to geometrical isomers and homotops mentioned earlier.

1.2. Types and Structures of Nanoalloys

Generally speaking, nanoalloys can be classified according to their mixing pattern (also named chemical ordering) and geometric structure.

1.2.1. Mixing Patterns

As depicted in figure 1, there are four main types of mixing patterns that can be identified for nanoalloys.
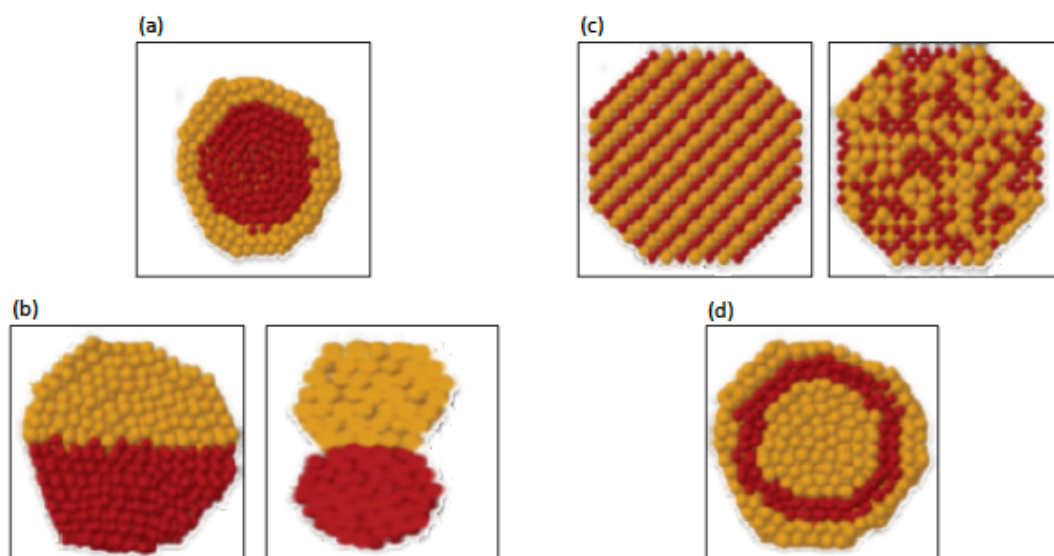
Figure 1 Cross section representation of mixing pattern (a) core-shell, (b) subcluster segregated, (c) mixed, (d) three shell (Ferrando et al., 2008)

First, there are core-shell segregated nanoalloys figure 1(a), where a shell of one type of atom (B) surrounds a core of another (A), though there may be some mixing between the shells. There are numerous examples of this mixing pattern. One can denote these clusters as "$A_{core}B_{shell}$".

Second, there are subcluster segregated nanoalloys figure 1(b). Here there are two possibilities. There may be a mixed interface shared by A and B subclusters (left). It is also possible that only a small number of A-B bonds exist (right). Although possible in principle, there is no specific example known to date.

Third, there are mixed A-B nanoalloys figure 1(c). The mixed nanoalloys can be ordered (left) or random (right). One can use the term "mixed" for the ordered mixed nanoalloys, and "intermixed" for the randomly mixed nanoalloys (solid solution). Random mixing is common to many systems.

Finally, there is the fourth possibility, the multishell nanoalloy formation figure 1(d). In this pattern of mixing, there are layered or onion-like alternating shells of A and B atoms.

In simulations of the growth of Cu-Ag, Ni-Ag and Pd-Ag clusters, metastable multishell nanoalloy formation has been observed (Baletto et al., 2003). There are also studies showing stable arrangements as in Co- Rh (A-B-A type) and Pd- Pt (A-B-A-B type) clusters (Fromen et al., 2006, Cheng et al., 2006). In experiments, it was possible to produce three-shell Pd-Au nanoparticles (Ferrer et al., 2007), where there is an intermixed core surrounded by Au-rich intermediate shell and a Pd-rich outer shell.

1.2.2. Geometric Structures

There are several possible structural types for nanoalloys in analogy with pure metal clusters (Baletto and Ferrando, 2005).

Geometrically, there are crystalline and non-crystalline structures possible figure 2, where the crystalline structures are simply fragments of bulk crystals, such as octahedral or truncated octahedral forms of face centered cubic bulk structure. It is also possible to have non-crystalline structures, such as icosahedral, decahedral, polytetrahedral, and polyicosahedral forms.
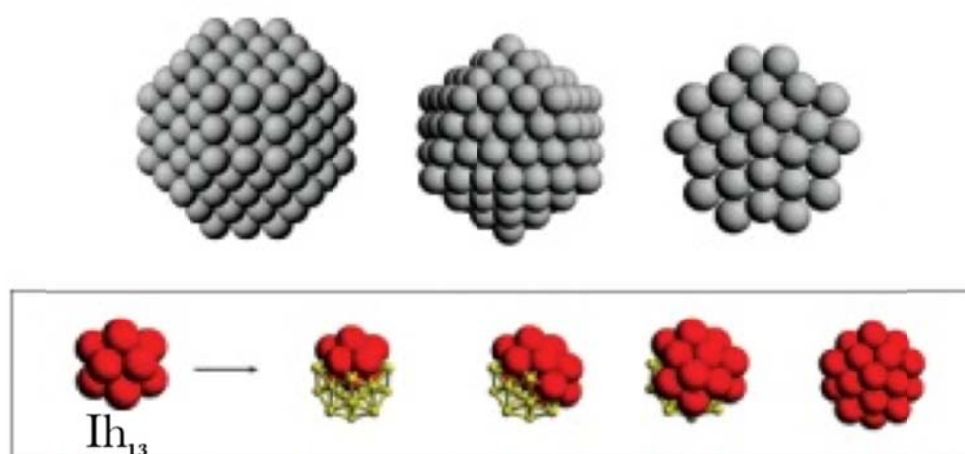
Figure 2 From left to right, top row fcc truncated octahedron, icosahedron, and truncated decahedron, bottom row polyicosahedral cluster composed of interpenetrating elementary icosahedra of 13 atoms (Rossi et al., 2004) here indicate by Ih_{13}. Polyicosahedral structures are a subfamily of polytetrahedral structure because the elementary icosahedron is composed of 4-atom tetrahedral.

Typically, non-crystalline structures take compact shapes presenting efficient atomic packing with some internal strain, both of which arise due to nonoptimal interatomic distances in the structure. For larger sizes, crystalline structures are favored, as the strain energy in non-crystalline clusters increase in proportion to their volumes (Baletto and Ferrando, 2005).

Icosahedra, polytetrahedra, and polyicosahedra are more commonly observed in nanoalloys than in pure metal clusters. These structures are favored especially when there is a large size mismatch between constituent atoms, because small atoms are typically accommodated inside the cluster and reduce the compressive strain (Rossi et al., 2004).

A study (Darby et al., 2002) on models of Cu-Au clusters showed that the icosahedral structure is not the lowest energy structure for pure 55-atom gold clusters; however, substituting just one gold atom with a copper atom stabilizes the icosahedral structure of $Au_{54}Cu_1$.

The stability of certain structural patterns may further increased due to electronic shell closure effects as in another interesting study (Barcaro et al., 2006) where 40-atom Cu -Ag clusters having a specific core-shell polyicosahedral structure is stabilized due to electronic effects. In another study (Rajesh and Majumder, 2006) on 13-atom icosahedral Pb clusters, when an internal Pb atom is replaced by a smaller Mg atom, the energetic stability of the cluster and the gap between the highest and lowest unoccupied molecular orbital has been shown to increase.

1.2.3. Factors Influencing Segregation, Mixing, and Ordering in Nanoalloys

The tendency for segregation or mixing and the level of atomic ordering in binary nanoalloys (A_mB_n) depends on the following factors.

(1) Bond strengths. There is a tendency towards mixing when A-B bonds are stronger than A-A and B-B bonds. If not, there is a tendency in the system towards segregation. Then if A-A bonds are stronger than B-B bonds, A atoms tends to be at the center (core) of the cluster.

(2) Bulk surface energies. If A has a lower surface energy than B, A atoms tend to segregate to the surface to minimize the total energy of the system.

(3) Atomic sizes. Smaller atoms prefer to be in the core, as the spatial relationship between atoms in the core of a cluster is more confined, this is particularly true for icosahedral structures due to the compressive stresses in the core.

(4) Charge transfer. When electrons are transferred from a less electronegative element (most metals) to a more electronegative element, there is a tendency towards mixing of these elements (ionic character of bonding).

(5) Binding energy between cluster and substrate/surfactants. If one of the constituents of the alloy, say A atoms, has a strong binding with the surfactants or the support, then A atoms tend to occupy the surface rather than the core of supported or coated clusters.

(6) Electronic/magnetic effects. Electronic shell structure or electron spin interactions may lead to stabilization of a given cluster size or composition, or certain segregation arrangements.

The atomic arrangement observed in a given A_mB_n nanoalloy cluster is a result of not only the interplay between the factors mentioned above, but also the preparation method and conditions such as temperature and pressure.

1.3. Passivated, Coated, and Supported Nanoalloys

Mainly depending on the production method, nanoalloys can be classified as:

(1) Free/bare nanoalloys. They are uncoated and unsupported. Free clusters and nanoparticles can be generated in the gas phase or by a pulsed cluster beam.

(2) Passivated/coated nanoalloys. In this case, the cluster surface is stabilized by coordination to the surfactant molecules. Coated clusters can be produced in the gas phase or in solution.

(3) Supported nanoalloys. Clusters are supported on external surfaces or internal surfaces (i.e., inside porosities).

1.3.1. Passivated Clusters and Colloids

Colloids are particles (1nanometer- 1micrometer) dispersed throughout another substance. There are several examples known for many centuries (Faraday, 1857, Broglia, 1994) such as stained glass windows, where small colloidal particles are suspended in glass.

It is difficult to investigate free metal clusters, as they are hard to be isolated and handled on a scale like molecules. To be able to study clusters at roughly a uniform size and make use of their distinct behavior in device applications, it is needed to passivate those free clusters with a surfactant coating (passivated /coated clusters). This way coalescence of the clusters can be prevented to occur at high cluster densities.

This can be done in one of two ways, (Bönnemann and Richards, 2001) namely, electrostatic stabilization and steric stabilization. Electrical double layer of ions adsorbed at the particle surface leads to Coulombic repulsion between nanoparticles, which in turn, cause an electrostatic stabilization of the particles. Or the spatial relationship between the clusters and bulky organic molecules stabilizes the free clusters. For example, electrostatic stabilization is observed when preparing sodium citrate gold sols, and steric stabilization occurs when mixing metal clusters with polymers or block copolymers.

1.3.2. Supported Nanoalloys

Nanoparticles can be deposited from a solution or gas phase onto a substrate, such as graphite, silicon, or an inorganic oxide. Particle size selection may be possible when depositing from the gas phase. They can alternatively be deposited in vacuum onto the surface of an inert gas matrix. Using these experimental techniques, individual clusters can be investigated by microscopic methods; however, it is difficult to draw conclusions about structure of free clusters by examining surface-supported clusters. This is because when supported, the geometric or electronic structure of the cluster

may be affected. This is similar to the problems encountered when investigating thin films deposited on substrates or passivated crystalline clusters.

1.3.3. Bimetallic Transition-Metal Carbonyl Clusters

For more than 5o years, transition metal clusters have been extensively investigated, (Schmid and 1994, Johnson, 1980, Mingos and Wales, 1990, Braunstein et al., 1999, Dyson and McIndoe, 2000) thanks to the technique, which allowed stabilizing them sterically by the surface coordination of CO molecules, yielding the so-called transition-metal carbonyl clusters.

More recently, it became possible to stabilize large 10- to 100-atom transition metal, bimetallic and trimetallic clusters.

1.4. Applications of Nanoalloys

Nanoalloys can be tailored for specific and industrially relevant applications and have already found applications in several technologically important areas, such as catalysis (catalytic converters, electrochemical fuel cells) and magnetics (data storage).

1.4.1. Catalysis

Catalytic activity and other properties of small metal particles and clusters can be modified and fine tuned by nanoalloying of two different metals, (Sinfelt, 1973) and modifying the geometric and electronic structures. That's why the field of alloy nanocatalysis is presently a hot topic of study (Schmid, 1999, Braunstein and Rosé, 2008, Thomas et al., 2002). According to Schmid et al. (1991) synergistic effects may arise in bimetallic nanoalloys due to different atom neighborhood relations and this can yield distinct and better catalytic properties as compared to monometallic clusters.

For the design of new catalytic materials, core-shell segregated bimetallic nanoalloys are promising. For example, in petrochemicals industry, Pt-Ir and Pt-Re catalysts are extensively utilized in reforming processes, and in automotive industry, bimetallic and trimetallic clusters containing Pt, Pd, and other metals find applications in catalytic converters.

Bimetallic nanoparticles have been studied for a long time for nanoalloy applications in the field of electrocatalysis (fuel cell applications). In the 1960s, Exxon employees Sinfelt and colleagues have developed supported bimetallic cluster catalysts (Sinfelt, 1983). Later in 1970s, Pt catalysts and Pt-containing bimetallic nanoparticle catalysts found application in commercial prototype phosphoric acid fuel cells (Kunz and Gruver, 1975, Stonehart, 1992). In 1974, Petrow and Allen patented a method for manufacturing bimetallic nanoparticle electrocatalysts, in which colloidal precursors are adsorbed onto carbon black (Stonehart, 1992). Bönnemann and Brijoux (1999) and more recently Russell and Rose (2004), reviewed many applications of bimetallic nanoparticles in electrocatalysis.

1.4.2. Magnetic Properties

When embedding clusters of magnetic 3d elements (Cr, Fe, Co, and Ni) or their mixtures in a nonmagnetic metal or insulating matrix, the material exhibit giant magneto-resistance (GMR) behavior, i.e., its resistance changes greatly when a magnetic field is applied. For example, a GMR effect of up to 50% is observed when iron clusters are embedded in a silver host (Sumiyama et al., 1995). Bimetallic nanoalloys have also been produced by embedding magnetic 3d metals into nonmagnetic 4d (Rh, Pd, Ag) or 5d metals (Pt, Au). GMR materials have potential applications in magnetic sensors and magnetic recording.

A high magnetic moment and anisotropy are required in high-density magnetic recording, and this may be achieved by 3d-4d nanoalloys (Co-Rh and Ni-Rh) where large local magnetic moments of 3d metals and strong spin-orbit coupling of 4d metals are combined (Fromen et al., 2006).

Similarly, when 3d metals and 5d metals are combined as in Fe-Pt and Co-Pt, the nanoalloys formed exhibit high magnetic anisotropy with associated high magnetic susceptibility and coercivity. This makes them good candidates for ultrahigh density magnetic recording media.

1.5.   Methods for Generating Nanoalloys

Nanoalloy clusters can be produced by various methods, in the gas phase or solution, supported on a solid surface, or embedded in matrices. Compared to the methods for producing pure monometallic clusters, (Haberland, 1994, Schmid, 2005), there may be some further difficulties in generating bimetallic (and multimetallic) nanoclusters. There are several reviews of methods for synthesizing metallic nanoclusters (Bönnemann and Richards, 2001, Burda et al., 2005, Schmid, 2005).

1.5.1.   Molecular Beams

Molecular beam techniques made it available to produce and investigate isolated clusters in a cluster beam (Milani and Iannotta, 1999, Binns, 2001).

There are four stepwise processes in generating clusters: (1) vaporization, (2) nucleation, (3) growth, and (4) coalescence/ aggregation. In the first process, atoms or molecules are produced in the gas phase by evaporation. The second process is nucleation of clusters by condensation of atoms or molecules. In the third stage, the cluster nuclei grows, in many cases at supersonic speeds, by further condensation where additional atoms or molecules join the nuclei to make them more stable. However, at this stage, some clusters may shrink or even evaporate completely, or fragment into smaller clusters. In the final stage smaller clusters can merge to form larger clusters.

When clusters pass through a narrow nozzle into vacuum, they experience isenthalpic and adiabatic expansion. Initial condensation occurs in the nozzle where there is a relatively higher pressure and when the clusters formed there enters into vacuum they cool down and condensation continues at a faster pace (supersonic growth), forming a narrow cluster beam in the so called free jet region. There the isolated clusters move at high speed without colliding each other, as they have approximately the same speed and direction. This makes it possible to study the properties of non-interacting "free" clusters (Johnston, 2002).

Depending on the nature of metal atoms to form clusters (melting temperature, partial vapor pressures), there are several options available as the cluster source;

however, mostly the gas condensation type sources are used in recent years as follows (Johnston, 2002, Haberland, 1994, Baletto and Ferrando, 2005, Milani and Iannotta, 1999, Binns, 2001).

(1) Laser vaporization. A laser beam is used to evaporate the target. The target may be either an alloy rod target or a powder mixture of metals chosen. It is also possible to evaporate two monometallic targets simultaneously to form bi-metallic clusters.

(2) Pulsed arc cluster ion source. An intense electrical discharge through the target is utilized to evaporate the constituent elements. The target may be monometallic or a bulk alloy of two or more metals.

(3) Ion sputtering. In this method, a metal target is bombarded by high-energy inert gas ions to generate clusters. Typically, Kr^+ or Xe^+ ions with 10-30 keV energy are utilized at around 10 mA.

(4) Magnetron sputtering. Over the target, argon plasma is ignited by using a potential (dc or rf) and confined by using a magnetic field. The Ar^+ ions are then accelerated onto the target to sputter metal ions off the target.

After producing metallic vapors by any one of the above methods, they can be collided with a cold inert carrier gas and let to expand through a nozzle (Cottancin et al., 2000) to obtain a cluster beam.

1.5.2. Chemical Reduction

Metallic salts dissolved in some solvent can be chemically reduced to produce colloidal particles of metals and alloys. This process generally involves surfactants or polymeric ligands, which passivate the surface of the clusters formed (Bönnemann and Richards, 2001, Toshima and Yonezawa, 1998). Initially published by Faraday (1857) this method was later improved and systematized by Turkevich et al. (1951).

Colloidal metal particles, in general, consist of a metallic core and a surrounding ligand shell. For example, alkylthiols ($CH_3(CH_2)_nSH$) and thioethers ($CH_3(CH_2)_nS(CH_2)_mCH_3$) form strong bonds with late transition metals, such as

silver, palladium, platinum and in particular gold. This provides quite stable colloidal particles.

Turkevich have proposed a formation mechanism for colloidal nanoclusters. The proposed mechanism involves three steps: (1) nucleation, (2) growth, and (3) subsequent agglomeration. Later research proved that this mechanism is essentially a correct depiction of what happens. First, relatively stable particles (nuclei) that are more likely to grow than to dissolve are formed. These seed particles, mostly smaller than 1 nm, then grows further to form stable nanoclusters (Turkevich et al., 1951).

Colloids may form at the interface between two phases, in which case the metal salt is dissolved in an aqueous layer, and surfactant and reducing agent are in an organic layer (Binder, 2005).

Another method to generate clusters is by utilizing inverse/reverse micelles. A micelle is an approximately spherical aggregate of surfactant molecules, dispersed in a liquid colloid where the ionic head groups at the center with the tails extending out forms a hollow space at the center. The head groups on inner surface make it chemically attractive to metal ions, while the tails on the outer surface interact with the surrounding organic solvent. The particle size and its distribution can be controlled by adjusting micelle size and experimental conditions, such as solvent, surfactant, and reducing agent.

By changing the nature of the passivating ligands, the solubility properties of the metal colloids can be controlled (Bönnemann and Richards, 2001). For example, water-soluble colloids (hydrosols) may be produced with hydrophilic ligands forming a passive surface on the clusters. Furthermore, by utilizing lipophilic ligands, lipid-soluble metal colloids (organosols) in organic solvents can be produced.

1.5.2.1.   Co-Reduction

Reducing agents, such as H_2, N_2H_4, $NaBH_4$ can be utilized in preparing bimetallic colloids by reducing certain salt mixtures in solution phase (Bönnemann and Richards, 2001, Burda et al., 2005, Bönnemann and Brijoux, 1999, Toshima and

Yonezawa, 1998). In this process, first the core is formed by precipitation of the metallic element having the highest redox potential. Then a shell is formed around the core by deposition of the other metal (V. Goia and Matijevic, 1998). A good example would be co-reduction of palladium and silver, where palladium has the higher redox potential. This reduction process yields a core-shell structure with palladium at the center and silver outside.

In this co-reduction process, if one uses a surfactant that bonds much more strongly to the metal with higher redox potential, then the other metal is reduced first and core is formed by precipitation of the metal with the lower redox potential. This leads to a stable arrangement with a reverse order. For example if ammonia is added to the above process, ammonia will preferentially bind to palladium, which core-shell structure with silver at the center and palladium outside (V. Goia and Matijevic, 1998).

One can produce alloyed bimetallic clusters, if the two metallic elements have high mixing enthalpies and there is not much difference between their redox potentials (V. Goia and Matijevic, 1998, Henglein and Giersig, 1994).

An interesting example is the cubic core-shell bimetallic clusters with a manganese core are covered by a shell of Nickel as demonstrated by V. Goia and Matijevic (1998). First a cubic core-shell structure is produced where the manganese carbonate cubes is coated by a $Ni(CO_3) \cdot Ni(OH)_2$ double salt shell. Then the shell can then be calcined to form the core-shell bimetallic oxide cluster with a core Mn_2O_3 and a shell of NiO. Finally, through a 6-hour reduction process in hydrogen gas at 350°C, Mn_2O_3 and NiO are reduced yielding the bimetallic clusters.

Another interesting example may be ellipsoidal $Fe_{core}Sn_{shell}$ bimetallic clusters. First a shell of SnO_2 is coated on the surface of alpha-Fe_2O_3 particles with ellipsoidal morphology. Then the shell is calcined at 750 °C to form a tin oxide shell around iron oxide core. Finally, through a reduction process at 350 °C in H_2 atmosphere, $Fe_{core}Sn_{shell}$ particles are produced but with Fe_3Sn_2 at the interface between core and shell (V. Goia and Matijevic, 1998, ul Haq and Matijević, 1998).

1.5.2.2. Successive Reduction: Reaction of Preformed Clusters

A core-shell structure can also be obtained by depositing another metal onto a preformed cluster of one metal via the "seed-germ" process (Schmid and 1994). In this process either there are no surfactant molecules involved or they are weakly coordinated with the surface of the clusters. The preformed clusters are reduced in the presence of salts of a second metal (Schmid, 1999, Schmid et al., 1991). An analogous process is the "living metal polymer" idea through which all-possible onion-type trimetallic A-B-C nanoparticles can be produced as postulated by Watzky and Finke (1997).

1.5.2.3. Reduction of Co-Complexes

A complex containing two different metallic elements can be reduced to make bimetallic nanoclusters in a single step process (Toshima and Yonezawa, 1998). For example, Pd-Ag and Pt-Ag bimetallic nanoclusters have been experimentally produced likewise (Torigoe and Esumi, 1993).

1.5.3. Thermal Decomposition of Transition-Metal Complexes

Low-valent transition-metal complexes has been thermally decomposed to synthesize several nanoparticles, where the transition-metal complexes are usually organometallic compounds and clusters or noble-metal salts, and the resultant nanoparticles are especially of one or two of the more noble metals in the complex (Bönnemann and Richards, 2001, Bönnemann and Brijoux, 1999, Esumi et al., 1990). By thermolysis with polyvinylpyrrolidone or other stabilizing ligands, better results are achieved (Bradley et al., 1996).

By vacuum heating precursor organometallic clusters anchored within silica micropores, for example, at 200°C for two hours, bimetallic nanoparticles, such as Ru_6Sn, Ru_5Pt, $Ru_{12}Ag_4$ and $Ru_{12}Cu_4$, has been produced by Thomas et al. (2002). This thermolysis process was done usually with phosphine or carbonyl ligands. The size of the silica micropores usually ranges between 3 nm and 30 nm figure 3. The numbers of atoms in the metal nanoparticles are the same as the number of metal atoms within the precursor complexes. As the complexes contain only a small

number of metal atoms, the nanoparticles are quite small and range between 1 nm and 1.5 nm. Thus all of the metal nanoparticles reside on the surface and act as nanocatalytic sites. They show high catalytic activities and frequently high selectivities for certain single-step low temperature hydrogenations at 60-100°C (Thomas et al., 2002). Colloidal catalysts, as they are prone to coalescence and sintering, remains highly active for shorter times compared to nanocatalysts. Nanocatalysts last longer as that are fastened to the silica support. The nanocatalyst particles are coordinated to silica, not surprisingly, via oxygen atoms, as demonstrated by X-Ray Absorption Spectroscopy.
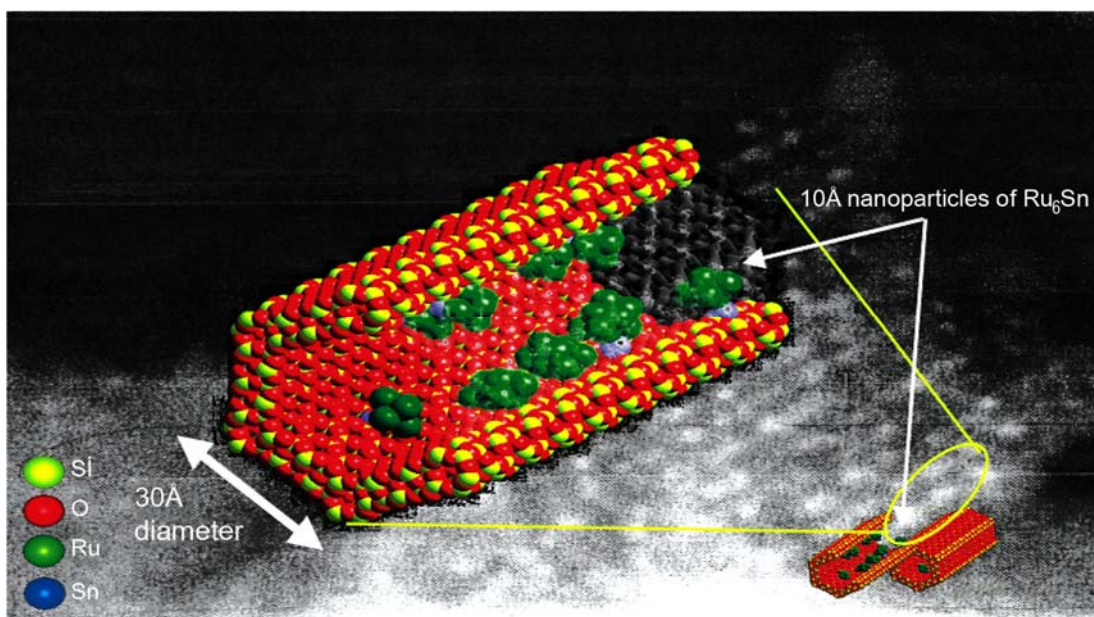
Figure 3 Computer graphic illustration of the Ru_6Sn nanoparticles adsorbed in a zeolite-superimposed on an enlarged SEM image of the same system (Thomas et al., 2002)

By alcohol reduction of solutions containing $AgNO_3/PdO_x$ and CuO_x/PdO_x, several different Pd_nAg_m and Cu_nPd_m colloids have been generated, respectively (Rao et al., 2000). Cu_nPd_m colloids can also be prepared by thermal decomposition of acetate mixtures in high-boiling solvents. Pt-Ag colloids have been produced by reduction of

oxalate salts with sodium borohydride. Also by thermal evaporation of the metals in a vacuum, bare nanoalloys, such as Ni-Cu, Ni-Pd, Cu-Pd and Ag-Au, have been produced.

Shifts relative to the bulk metals have contributions not only due to mixing but also because of size effects, as indicated by the core-level binding energies measured by X-ray photoelectron spectroscopy (Harikumar et al., 1997).

1.5.4. Ion Implantation

Due to their optical, magnetic, and catalytic properties, there is growing interest on metal nanoclusters embedded in insulating matrices. For example the 3rd-order susceptibility $\chi(3)$ of the matrix is exceeded by that of the nanoclusters. This causes the refractive index to be intensity dependent and higher. This may lead to production of optical switching devices (Mattei et al., 2005). Implanted solid-solution bimetallic nanoclusters can be produced by first implanting one metal than implanting the other (not implanting simultaneously), as demonstrated by Ag-Au, Cu-Pd, and Cu-Au nanoalloys produced by ion sequential implantation in silica using 100 keV ion beams.

1.5.5. Electrochemical Synthesis

Electrochemical Synthesis is a useful method to produce metallic nanoparticles in solution (Bönnemann and Richards, 2001) and there are several studies that have demonstrated its usefulness.

By using two sacrificial bulk metallic anodes in a single electrolysis cell, production of Pd-Ni, Fe-Co, and Fe-Ni nanocolloids have been demonstrated (Reetz et al., 1995). Pt, Rh, Ru, and Mo are relatively less soluble as anodes. Binary nanoclusters among them can be produced by reducing their salts at the cathode.

Core-shell layered bimetallic nanoparticles can also be generated electrochemically, as in the example of $Pt_{core}Pd_{shell}$ (Kolb et al., 1996), where the Pt core can be considered as a "living-metal polymer" on which the Pd atoms are deposited figure 4 (Bönnemann and Richards, 2001).

In electrochemical synthesis of a couple of two metals, the one, which is more reactive, act as the reducing agents for the other (more noble) metal. For example, Pd-coated Fe nanoparticles have been produced (Wang and Zhang, 1997), as the Fe^{2+}/Fe^0 couple has an electrode potential E^0=-0.45 Volt, while electrode potential E^0 for $[PdCl_4]^{2-}/Pd^0$ is +0.59 Volt.
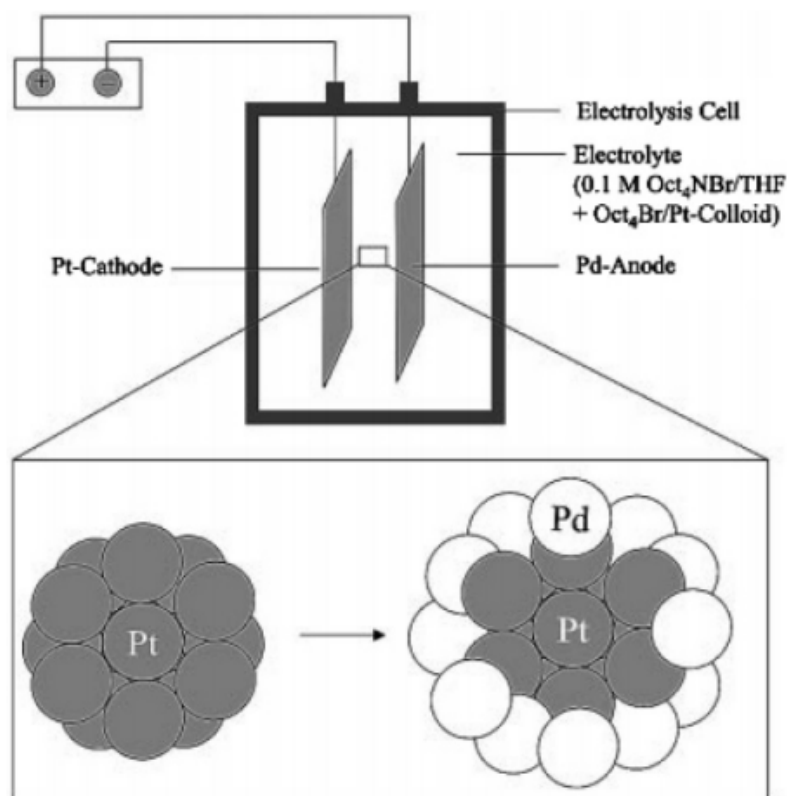
Figure 4 Schematic representation of an electrolysis cell for the preparation of layered PdPt nanocolloids (Bönnemann and Richards, 2001).

1.5.5.1. Electrodeposition at Liquid−Liquid Interfaces

The liquid-liquid interfaces between two immiscible liquids are characteristically smooth and has no electrode surface effects. That's the reason why there is growing interest on the nanoparticles of noble metals generated by electrodeposition at such

interfaces. There have been studies on forming silver, gold, platinum and palladium nanoparticles at interface between hydrocarbon and aqueous phases (Cheng and Schiffrin, 1996, Platt et al., 2002).

Although the presence of nanoparticles decreases the interfacial tension, it is still high the interface between oil and water is high. This allows for a very dynamic supramolecular assembly, which in turn helps any interfacial defects present to be heaed quickly (Binder, 2005).

Although platinum is nobler than palladium and requires a larger over potential, nanoparticles of palladium forms more easily and more quickly than platinum nanoparticles. This may be because palladium has a higher surface energy than platinum (Platt and Dryfe, 2005).

It has also been observed that palladium particles act as seeds and promote platinum deposition. As shown by SEM and XRD studies, when palladium is co-deposited with platinum, aggregates ranging between 0.2 μm and 0.5 μm in diameter are formed by 4 nm or smaller particles (Platt and Dryfe, 2005). EDX studies indicate that the deposits are made up of both platinum and palladium; however, it is not certain if there are Pd and Pt clusters within aggregate form or actually a Pd-Pt nanoalloy has been generated.

1.5.6. Radiolysis

In order to produce nanoclusters of transition metals by reduction of metal ions, a useful technique is radiolysis of aqueous solutions, which has been used to generate several different nanoalloys including Ag-Au, Ag-Cu, Ag-Pd, Ag-Pt, Au-Pd, Au-Pt, Pt-Ni and Pd-Cu. (Remita et al., 1996, Belloni et al., 1998, Belloni and Mostafavi, 2008, Treguer et al., 1998).

In this technique, γ-ray irradiation of water produces solvated electrons, which in turn lead to reduction of the metal ions present in the water and formation of clusters upon their coalescence. When using this technique to form bimetallic nanoparticles, the metal that is more readily reduced is the nobler one.

On the other hand, whether a core-shell or alloyed structure will be obtained is determined by several other factors, including (1) the radiolysis rate which is proportional to the dose of γ-rays, (2) the amount and ratio of the metallic elements dissolved in the water, (3) how fast is the electron transfer between ions, (4) the coordination between the ligands and the metal ions (Belloni et al., 1998, Belloni and Mostafavi, 2008).

For example, higher doses of γ-rays leads to an alloyed structure rather than forming $A_{core}B_{shell}$ structure. However, in certain alloy systems, particularly those with atomic ordering, mixing behavior is observed at low-to-medium doses of γ-ray irradiation (Cu-Pd alloys with tendency to form the ordered Cu_3Pd and CuPd superlattices and Ni-Pt alloys with ordered Ni_3Pt superlattices) (Belloni et al., 1998).

Metal electrodes used in the chlorine-soda process has been manufactured by graft Pt-Ru and Ni-Ru nanoclusters on either titanium or nickel by the radio lytic method (Amblard et al., 1991) .

Another good application was formation of certain metallic clusters on silver halide emulsions for photographic development process where these clusters (for example, Ag-Au, Ag-Cu, and Ag-Cu-Pd) act as highly active development leading to high-resolution (Belloni et al., 1998).

1.5.7. Sonochemical Synthesis

In sonochemical synthesis, high-intensity ultrasound is applied on an aqueous solution to generate nanoparticles. For example, by utilizing this method on an aqueous solution of gold and palladium ions, Au-Pd nanoparticles have been produced where the particles are sized at abut 8 nm as measured by TEM and have a core-shell structure with a gold core as indicated by EDX studies (Mizukoshi et al., 2000).

Compared to radiochemical method, sonochemical synthesis produces nanoparticles with different morphologies, namely smaller particles having a core-shell type structure. This is partly determined by certain aspects of the method: good stirring,

presence of a microjet stream and cavitation bubbles producing shock waves as they are collapsed (Mizukoshi et al., 2000).

In another study producing Au-Pd nanoclusters with core-shell structure, successive deposition was proved to be more effective than simultaneous deposition (Canxia et al., 2003).

1.5.8. Biosynthesis

Biomineralization originates from the mineral growth dictated by biomolecules (Mann, 2001). Frequently, first the nanoparticles are formed, then the self-assembly of templating macromolecules leads the nanoparticles to organize into ordered arrays (Brayner et al., 2005).

The technological importance of biomineralization is due to efforts to develop bottom-up techniques for the organization of the nanoparticles on micrometer, sub-micrometer, nanometer, and multiple length scales.

1.5.8.1. Biomimetic Synthesis

Biomimetic materials are materials developed using inspiration from nature. For the nanoscale organization of inorganic materials, several methods have been developed for biomimetic synthesis (Mann, 2001, Mann, 1996).

In controlling the growth of nanoparticles, several different biological systems have been used, including the three major macromolecules essential for all known forms of life, namely nucleic acids (e.g., DNA), proteins and carbohydrates (e.g., polysaccharides, which are polymeric carbohydrate molecules), and combinatorial phage display peptide libraries (Brayner et al., 2005).

For example, S layers are regular, quasi-2D protein crystals, which upon in vitro recrystallization, may be utilized to produce crystals in the form of sheets or tubes. It has been reported that they have been utilized as a template for the growth of arrays of Pt or Pd nanoparticles via in situ chemical reduction and electron-beam-induced growth in a TEM apparatus (Mertig et al., 2001).

Nanocomposite materials by FePt nanoparticles and DNA molecules have been produced by a process which utilized DNA molecules to dictate the assembly of the preformed nanoparticles and resulted in a larger spacing between the nanoparticles and modified magnetic behavior (Srivastava et al., 2007).

1.5.8.2. In-Vivo Biogeneration of Nanoparticles

Certain microbes have been investigated as they are capable of reducing certain metal salts to their metallic states (Lloyd and Lovley, 2001).

For example, divalent palladium ions in an aqueous solution have been reduced to cell-bound zerovalent Pd nanoparticles using bacterial hydrogenases (Macaskie et al., 2005) leading to nanoparticles varying greatly in size down to 5 nanometers.

The resultant particles showed ferromagnetic behavior and manifested high catalytic activity in hydrogenation. These microbially reduced Pd nanoparticles also proved to act as an effective catalyst when neither the bacteria nor chemically reduced Pd nanoparticles were effective alone for reducing Cr(VI) to Cr(III) (Mabbett and Macaskie, 2002).

Among several potential industrial use of biogenerated nanoparticles are bioremediation of contaminated water, soil or industrial wastes, where hazardous substances are broken down into less toxic or non toxic substances, reclamation of precious metals such as palladium and platinum, and formation of Bio-Pd^0 catalysts which can be used as a bioinorganic catalyst in various applications (Macaskie et al., 2005).

By adding a suspension of alfalfa (medicago sativa) into a solution of nickel and titanium ions, and microbially reducing the resultant mixture, small Ni-Ti bimetallic clusters ranging between 2 to 5 nanometers have been generated (Liu et al., 2006).

1.6. Amorphous Metal–Metalloid Alloy Nanoparticles

Recently much consideration has been paid on metal-metalloid alloy amorphous nanoparticles (ANPs) in practice, because they are considered as potential catalysts

and among them generally Ni–B and Ni–P ANPs have been examined and reported (Wu et al., 2007). Because of their technical importance, amorphous alloy are investigated for more than 50 years. On the other hand, amorphous alloy nanoparticles have received attention since 1980 because of their unique isotropic structure and high concentration of the coordinately unsaturated sites leading to the high catalytic activity and selectivity superior to their crystalline counterparts (Wu et al., 2007). It was known that the amorphous alloy nanoparticles have great catalytic properties because of their unique short-range order structure. Consequently the understanding and clarity of the microscopic structure of the amorphous alloy nanoparticles is quite important.

Investigation of as-prepared Ni–B and Ni–P ANPs via X-ray diffraction (XRD) and selected area electron diffraction (SAED) techniques showed a broad peak at around 45° appearing in XRD profile, which demonstrates the typical amorphous structure of the samples (Yoshida et al., 1982). Broad and diffusive rings of SAED pattern also confirm and aid as an additional indication of an amorphous structure of the samples (Peter et al., 2001). Moreover it was found by scanning electron microscopy (SEM) and transmission electron microscopy (TEM) techniques that Ni–B amorphous nanoparticles prepared via chemical reaction has a spherical morphology (Deng et al., 1999), on the other hand, those prepared by electroless plating has a flower-like morphology (Deng et al., 1999).

The structure of amorphous alloy nanoparticles is normally disordered but in some cases partially ordered nano-domains can be found. For instance in the amorphous Ni–P alloy nanospheres, nano-domains with a short-range lattice were found, in which the lattice distance is consistent with that of the crystalline Ni (Xie et al., 2005). Xie et al. (2005) reported that the nanodomains are similar to the bulk in terms of their composition and the nanodomains were considered as short-to-medium range structure. Furthermore the superior catalytic characteristics of the amorphous alloy nanoparticles is due to their surface properties. The effects of B and P on the catalytic properties have been under debate but it is considered that they contributed to the modification of catalyst structure (Okamoto et al., 1979). The relationship between surface properties and catalytic activity of the amorphous alloy

nanoparticles are strongly affected by that surface concentration of the active metal, and adsorption and desorption processes (Wu et al., 2007).

The high B concentration in amorphous alloy nanoparticles caused the lower surface concentration of the active metal (Li et al., 2003), which, in some cases, maybe a disadvantage. For example, in Ni-B alloy, the lower surface content of Ni resulted a low productivity per weight of catalyst. To solve this problem, a high surface concentration of active Ni was achieved by electroless plating.

1.7.   Atomic Mechanism of Glass Formation in Nanoparticles

Our knowledge of the atomic mechanism of glass formation in nanoparticles is still restricting while liquids and ANPs of different materials have been studied intensively. As the glass formation phenomena is, in general, unknown, studies on this field are so attractive (Hoang and Odagaki, 2011). Lennard-Jones-Gaus (LJG) interaction potential was used to study the glass formation in the simple monatomic nanoparticles by Molecular Dynamics (MD) simulations in a spherical model with a free-like surface including 4457 identical atoms (Hoang and Duy, 2011). To achieve the model, the melt was cooled toward glassy state. In order to monitor the mechanism of glass formation, spatio-temporal arrangement of the solid-like and liquid-like atoms in nanoparticles was used. To identify the solid-like atoms that occur randomly in supercooled area, Lindemann freezing-like criterion was used (Stillinger, 1995, Hoang and Duy, 2011). Consequently some part of the atomic mechanism, observed in bulk glass, was also present in the case of nanoparticles (Hoang and Odagaki, 2011). In other words, during the cooling process from the melt in supercooled region, first solid-like atoms were formed at the interior of nanoparticles. At first step the solid like atoms were scattered in the system, although their tendency is to form a cluster figure 5a and 5b. As the process continues, the solid-like atoms increase in the system and they are tending to form a compact atomic arrangement figure 5c. Further cooling into the supercooled region resulted in merging of the small-sized clusters to form coarse clusters and single solid-like atoms to form a single percolated cluster. This cluster grows very fast by joining

more than 80% of the solid-like atoms at T_g in order to form glassy phase figures 5d and 6.

(a) T = 1.4.   (b) T = 1.2.

(c) T = 1.0.   (d) T = 0.7.
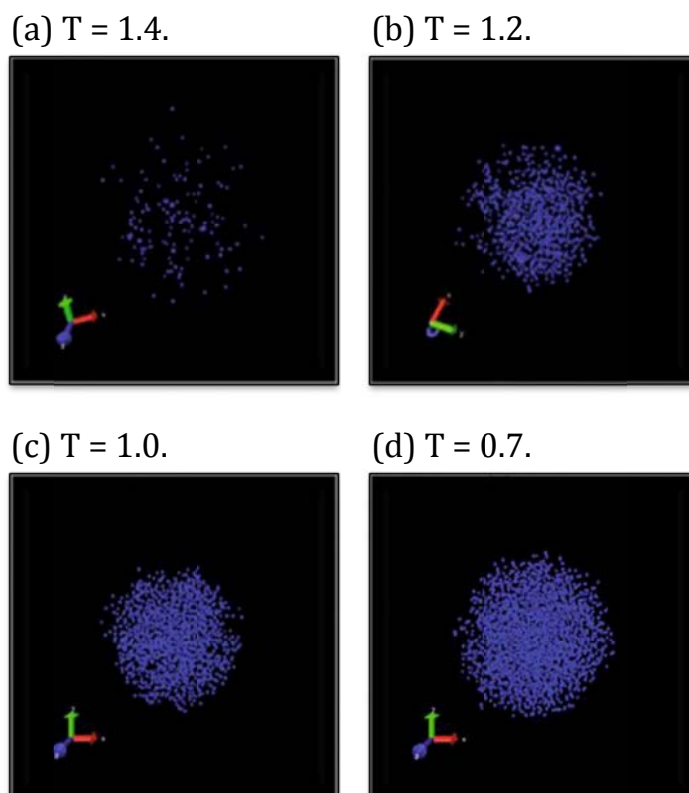
Figure 5 3D visualization of the occurrence of the solid-like atoms in nanoparticles. Note that glass transition temperature Tg = 0.5
(temperature is given in the LJ reduced units) (Hoang and Odagaki, 2011).
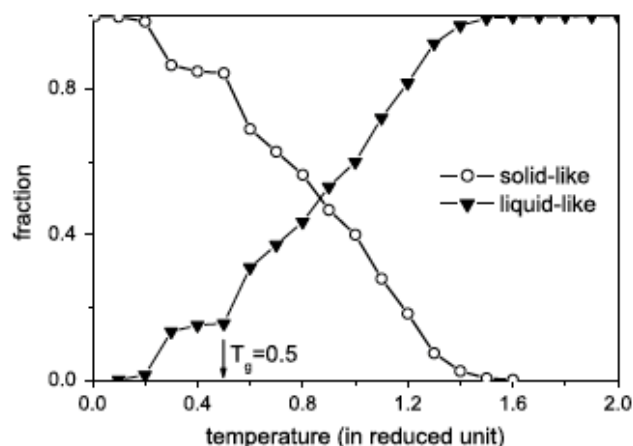
Figure 6 Temperature dependence of fraction of the solid-like and liquid-like atoms in the LJG nanoparticles upon cooling from the melt (Hoang and Odagaki, 2011).

While atomic mechanism of a glass formation in nanoparticles is similar to the bulk in some cases this phenomena shows heterogeneous-like behavior in nanoparticles and homogeneous in bulk. Because solid-like atoms in nanoparticles were formed in interior and then by decreasing temperature the solid-like domain grows outward to the surface figure 5. Solidification happened similar to the bulk when temperature is much lower than T_g figure 6.

Also it was reported by Hoang and Duy (2011) that in the LJG nanoparticles, radial density profile varies around a constant value in the inner part and fall down to zero in the outer shell. On the other hand, in the interior part atomic mobility is constant and rises up by increasing radial distance in the surface shell. Compared to the bulk dynamics of atoms, it is much faster, because T_g was reduced. Moreover diffusion constant of atoms in nanoparticles depends on temperature by Arrhenius law at high temperature region, but at lower temperatures it deviates from the law (Hoang and Duy, 2011).

Although liquid-like atoms in the glassy state (at $T \leq T_g$) prefer to occupy the outer shell, it was discovered that they do not form a pure liquid-like surface. Instead, the surface was formed by a mixture of the solid-like and liquid-like atoms in the way

27

that their densities are equal (Hoang and Duy, 2011). This is different from the common belief that naturally a liquid-like layer forms during pre-melting of the solids, including that of ice. This should be carefully investigated and also the terminology of "glasses with liquid-like surfaces" should be revised (Jones, 2003).

1.8. Fe-B Type Amorphous Nanoalloys

Traditional metallic glasses have seen considerable interest as a catalyst in hydrogenation reactions due to their high specificity and surface properties, as well as the mechanical and magnetic properties (Deng et al., 1999). The main reason for this is that metallic glasses are much more effective than their crystal equivalents, due to an excess of unsaturated bonds in the structure of metallic glasses and their favorable adsorption surface structures. The reason why glassy metal alloys have still not put in effective use as a catalyst is the trouble in making fine powder like crystalline materials. Today, studies in this direction are just begun to develop. Efforts to meet the industrial needs of surface-area started with the production of metallic nano-alloys really at the "nano" size (Rajesh et al., 2007). The first known nanoalloy has been obtained by consolidating $Pd_{70}Fe_3Si_{27}$ droplets from molten state by Jing et al. (1989). However, this alloy (and some of its counterparts today) nanoparticles has a sintered bulk structure where consolidated metallic glass nanoparticles stays together but separated by a glass/glass interface. But, thanks to the developments in the chemical methods, ultra-fine particles of amorphous alloys precipitated from metal salt solutions nowadays, have larger catalytic activity due to their high surface area and they have been obtained in binary and ternary systems such as Fe-B (Rajesh et al., 2007, Fernández Barquín et al., 2007), Ni-B (Jiang et al., 2005, Li et al., 2006, Wen et al., 2008), Co-B (Li et al., 2008), Ni-P (Shen et al., 1996, Wang et al., 2009), Co-Pt (Lata Rao and Sundar Manoharan, 2004), Fe-P-B (Rajesh et al., 2008b) and Ni-Co-B (Lee and Chen, 1999) These alloys have different structures than their ribbon-shaped amorphous counterparts (equivalents). Like their crystalline counterparts in solution in figure 7, they are composed of amorphous alloys precipitated from metal salt solutions.
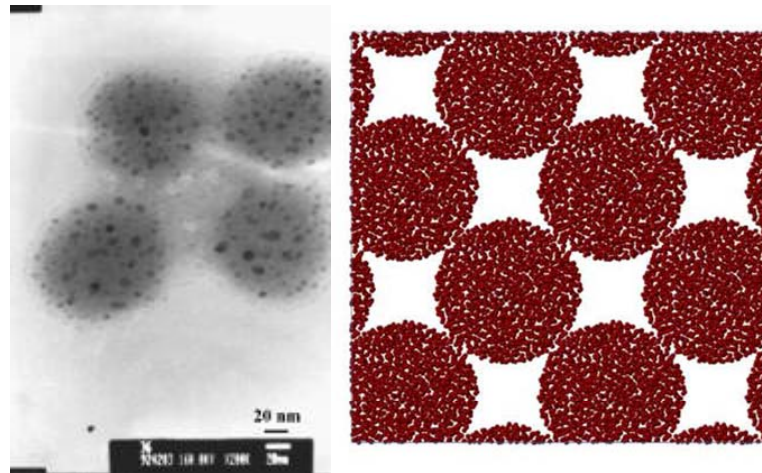
Figure 7 TEM image of Fe-P-B based metallic glass nanoalloys in $FeCl_2$ and H_2O. The image on the left is from (Rajesh et al., 2008a). The image on the right is a snapshot from a simulation of a similar arrangement in Cu-Zr-Ge system (Sopu et al., 2009).

The structure of the metallic glass nanoalloys is even less known than their intermetallic counterparts, and with each passing day their unforeseeable aspects come up. Fore example, a metallic glass nanoalloy, in contrast to known metallic glasses, may exhibit a sharp heat peak when melting (Aguado and López, 2005). Delogu (2010) has explored whether there is a limiting particle size for amorphous metallic glass nanoparticles to crystallize, and observed, even in short time scales in the order of nano-scale as in MD simulations, crystallization takes place immediately under 3 nm in Cu-Zr nanoalloys. In addition, one of rare studies that examines the effect of cooling rate on the structure of metallic glass nanoalloys has been carried out on a mono-atomic hypothetical system (Van Hoang et al., 2008), and this study couldn't examine in depth whether there is any structural effects of cooling rate.

To date, the most extensive and innovative study of a metallic glass have been accomplished by Vardeman and Gezelter (2008) in Ag-Cu system. Hence, it is inevitable to include this study in detail in this summary. The prominent aspects of the 2008 study by Vardemann ve Geltzer'are as follows:

- The molecular simulations they carried out simulate the "laser excitement" synthesis method.

- The particles are not in free space. The particles are modeled in a "solvent" with a viscosity that provides experimental cooling rates under simulation conditions. For this the particle surfaces work with Langevin dynamics.
- In spite of its importance, the theoretical gap on the topic of metallic glass nanoalloys in the literature is striking. It is thought that the extensive structural examination to be accomplished in this project in order to model metallic glass nanoalloys, will greatly contribute to the published knowledge and subsequently to industry and will pave the way for many other studies.

Fe-B binary metallic glasses are an important example in the transition metal and metalloid glasses group among these materials. This metallic glass group is not only interesting because of the unsatisfied bonds and disordered structures they have, but also has been the topic of many research studies due to their soft magnetic properties. FeB binary metallic glasses can be produced by melt spinning rapid solidification method; but these alloys have limited fields of usage due to their geometrical shapes and sizes (Jing et al., 1991, Cowlam and Carr, 1985). It is thought that this problem can be overcome by producing amorphous nanoparticles or metallic glasses with nano-crystallized amorphous/crystalline composite structure. On this topic, there are limited studies in literature.

1.9.   The Aim Of The Study

Following the recent introduction of nanoalloys to engineering applications, in addition to the limited parameters; temperature and composition employed for phase tuning in conventional alloys, there emerged a third parameter; namely, particle size, which made the properties attainable from materials nearly unlimited. As mentioned previously Nanoalloys, having diverse fields of applications to take part in mentioned fields of applications, it is required that synthesis conditions; i.e., structure-property relations can be predicted in advance. Therefore this study aims at modeling and production of metallic glass and intermetallic based nanoalloys. The studies of amorphous nanoalloys have been initiated in Fe-B system, which is a model system for studying magnetic metallic glasses.

For this reason in theoretical study attempt have been done to:

- Investigate stable structural configurations for amorphous $Fe_{80}B_{20}$, $Fe_{85}B_{15}$ nanoalloys
- Investigate the effect of temperature and particle size on:
    - Radial distribution functions (atomic distribution variation)
    - Surface energy for both systems
    - Morphology of the systems

The experimental part also have been done to:

- Synthesize of $Fe_{80}B_{20}$, $Fe_{85}B_{15}$ crystalline /amorphous nanocomposite powder by using surfactant-assisted high-energy ball milling
- Establish a relationship between structures, size of nanoparticles and their morphology on the magnetic properties of this nanoalloy
- Study and compare the differences in evolved microstructure via solidification and solid-state phase transformation under equilibrium and non-equilibrium processing conditions.
- Finally the results of theoretical modeling and simulations have been compered with experimental observations for nanoalloys that were produced by wet mechanical nanoalloying

CHAPTER 2

THEORETICAL STUDY

2.1. Computer Simulation

Due to certain distinct behavior that nanoparticles exhibit in comparison to corresponding bulk materials, they attracted great attention by researchers. Several examples of such interesting behavior can be given. For example, in bulk form, copper is a ductile metal; however, when smaller than 50 nm, copper nanoparticles attain a very high level of hardness. Another example is the quantum confinement in semiconductors which occurs for particles smaller than approximately 10 nm, which are called quantum dots and exhibit remarkable properties, such as emitting different colors of light depending on their sizes (Klimov, 2007) and having a very high quantum yield (Merbach and Toth, 2001). Super-paramagnetism observed in nanoparticles of magnetic materials (Merbach and Toth, 2001) is another good example.

There have been extensive studies on certain physical, chemical and thermodynamical properties, as well as distinct behavior of nanoparticles, which lead to recent efforts in utilizing nanoparticles in various industries including electronics, energy, environment, food, cosmetics, healthcare and biomedical industries.

However, most of these studies have focused on computer-based simulation because of the difficulties in experimental approaches, particularly the long processing times and the high production costs.

On the other hand, fast improvement of the computational capability of modern computers and accessible and improved computational methods, such as Molecular Dynamics (MD) simulations, there have been numerous publications on theoretical studies on nanoalloys and nanoparticles in recent years.

2.2. Introduction to Molecular Dynamics (MD) Simulation

In this part, a brief summary is given of the key issues necessary to carry out a molecular dynamics simulation, discussing about the intermolecular potential for molecules composed of atoms and the factors that influence the size of systems, and length of runs, in order to calculate statistical properties

Molecular dynamics simulations have been focused on understanding the properties of materials in terms of their structure and the microscopic interactions between their molecules. This is the bridge between theory and conventional experiments, which allowed us to learn something that cannot be found out in other ways. Molecular dynamics (MD) and Monte Carlo (MC) are two important simulation techniques.

In this study our work is based on molecular dynamics (MD). The main advantage of MD in comparison to MC is that it provides a path to dynamical properties of the system. Computer simulations provide microscopic and macroscopic connection in terms of length and time scales. Determination of the interactions between molecules will give us the exact estimation of bulk properties.

Models developed based on current theoretical knowledge can be compared with experimental results, through which, simulations help us to test models and theories behind.

Furthermode, simulations makes it possible to study cases for which an experiment cannot be carried out because of difficult or impossible conditions such as very high pressures or temperatures.

Eventually to directly compare with experimental results, a good model of molecular interactions is essential. On the other hand, a perfectly realistic molecular model is not required, and a model covering only the essential physics may be suitable.

2.2.1. Molecular Interactions

Molecular dynamics simulation involves numerical solution of the classical equations of motion, which for a simple atomic system may be written as

$$m_i \ddot{r}_i = f_i \qquad \qquad \text{Equation 2}$$

$$f_i = -\frac{\partial}{\partial r_i} u \qquad \qquad \text{Equation 3}$$

For this reason we must have the capability of calculating the forces f_i acting on the atoms, and these are usually taken from a potential energy $u(r^N)$ where $r^N = (r_1, r_2, \dots r_N)$ indicate the complete set of 3N atomic coordinates.

In empirical potentials, equations with parameters are fitted against known physical properties such as elastic constants and lattice parameters. (e.g. Lennard-Jones potential, Morse, etc).

On the other hand, semi-empirical potentials make use of the matrix representation from quantum mechanics as well as empirical formulae to determine the energy contributions. (e.g. EAM, tight-binding potentials, MEH.)

Ab-initio (first principles) methods use full quantum-mechanical formulae to calculate the potential energy of a system of atoms or molecules. Ab-Initio produces a large amount of information that is not available from the empirical methods, such as density of states information.
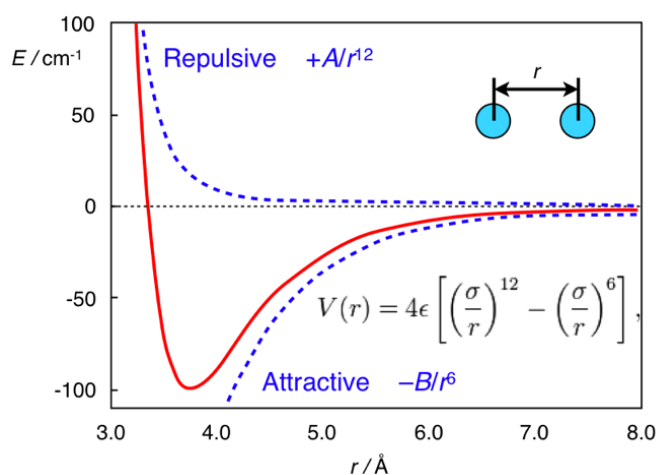
Figure 8 Typical two-body interactions (Lennard-Jones, van der Waals, MEH etc.)

2.2.2. Periodic Boundary Conditions

Atoms are on the surface; therefore the surface will affect the measured properties extremely. Even for 10^6 atoms, the sum of the atoms occupying the surface is 6% of the total, which is, though small, very important (i.e., it is nontrivial). Here we consider this problem as cubes surrounded by the replicas of itself. We can use the minimum image convention that each atom interacts with the nearest atom or image in the periodic array, as long as the potential range is not too long.

Whenever an atom leaves the main simulation box during the simulation, attention can be directed on to the incoming image. This is indicated in figure 9. Of course, when considering properties that are affected by long-range correlations, it is essential to keep in mind the artificial periodicity imposed.
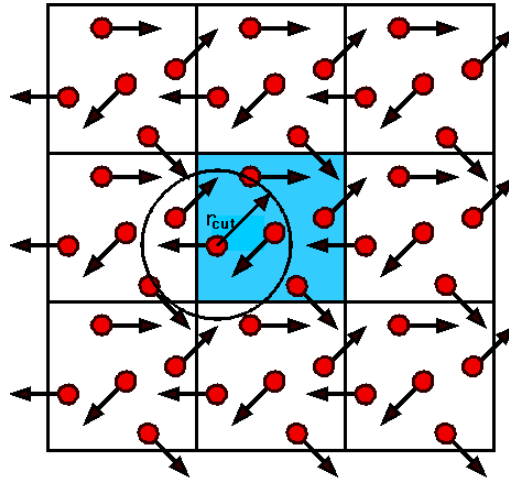
Figure 9 Periodic boundary conditions. As a particle moves out of the simulation box, an image particle moves in to replace it. In calculating particle interactions within the cutoff range, both real and image neighbors are included.

2.2.3. Neighbor Lists

An enormous number of pairwise calculations is needed to compute the non-bonded contribution to the interatomic forces in an (MD) simulation. We assume each atom i and loop over all other atoms j to determine the minimum image separations r_{ij}. Let us assume that the interaction potentials are of short range, $v\,(r_{ij})= 0$ if $r_{ij} > r_{cut}$, the potential cutoff. In this case, the program omits the force calculation, avoiding expensive calculations, and considers the next candidate j. However, the time to examine all pair separations is proportional to the number of distinct pairs, $\frac{1}{2}N(N - 1)$ in an N-atom system, and for each pair one must calculate at least r_{ij}^2; this still takes a lot of time.

The purpose for employing only the nearby pairs of atoms is saving precious computational time. Such a technique was recommended by Verlet (1967) to increase the speed of the program. A certain number of atoms are surrounded by the potential cutoff sphere, of radius r_{cut}, and they are also surrounded by a larger sphere of radius r_{list}, as indicated in figure 10.

Figure 10 The potential cutoff range (solid circle), and the list range (dashed circle), are indicated. The list must be reconstructed before particles originally outside the list range (black) have penetrated the potential cutoff sphere.

At first stage of simulation, a list of all neighbors of each atom is formed for which the pair separation is within r_{list}. Then as the simulation proceeds just pairs being in the list are checked in the force routine and this list reconstructed from time to time. It is essential to check and reconstruct the list before any unlisted pairs have passed through the safety zone (the shell between the list range and potential cut-off range) and come within the interaction zone (potential cut-off range). This can be done automatically if a record is kept of the distance moved by each atom since the last update. The choice of list cutoff distance r_{list} is arbitrary. Larger list will requires list reconstruction less frequently; however, it will not give as much of a savings on CPU time as smaller lists. The selection of a size for this list r_{list} can be made easily by experimentation.

Another method used for larger systems is dividing the simulation box (extension to non-cubic cases is possible) into a regular lattice of $n_{cell} \times n_{cell} \times n_{cell}$ figure 11.
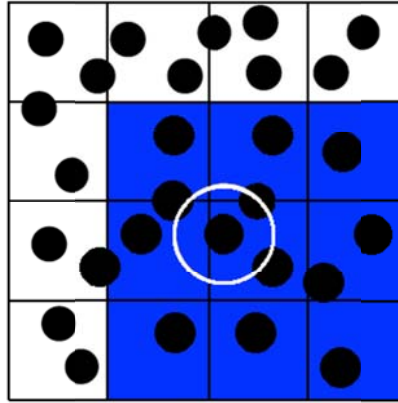
Figure 11 The cell structure. The potential cutoff range is indicated. In searching for neighbors of an atom, it is only necessary to examine the atom's own cell, and its nearest-neighbor cells (shaded).

The side of the cells was chosen $l_{cell} = L/n_{cell}$ greater than the potential cutoff distance r_{cut}. Searching through the neighbors is a rapid process in these cells, since there is a distinct list of atoms in each of those cells. It is needed to just look at atoms in the same cell as the atom of interest, and in the nearest neighbor cells. The cell structure may be set up and used by the method of linked lists (Knuth, 1973, Hockney and Eastwood, 2010). At the first step the atoms are organized into suitable cells. This is a fast process and can be repeated at all steps.

Then to scan over the contents of cells and compute the pair forces, pointers are employed in the force routine. Then, the contents of cells are scanned over and the pair force pointers are computed. This is a very efficient and proper method for large systems with short-range forces. As the examined area is cubic in contrast to the Verlet list, which is spherical, some excessive work is done.

2.2.4. Time limitation

Molecular dynamics simulation is a step-by-step arrangement of the molecules by time. There is limitation on time and length scales on the simulation process and results must be analyzed considering this fact. Simulation time correspond to

picoseconds to nanoseconds in real time which is proportional to $t \sim 10^3 - 10^6$ MD steps; although, in some cases, it may extend up to microseconds (Duan and Kollman, 1998).

Therefore, to trust and use the averages calculated in the simulations, one must ensure that the simulation reaches the equilibrium. Also to predicet the level of errors, the simulation averages must analyzed statistically. Consequently, the time of the simulation depends on the system and the physical properties that we are interested. A simulation is reliable when the simulation time is much longer than the relaxation time of the quantities that we are interested in. Figure 12 shows the scale in simulation.
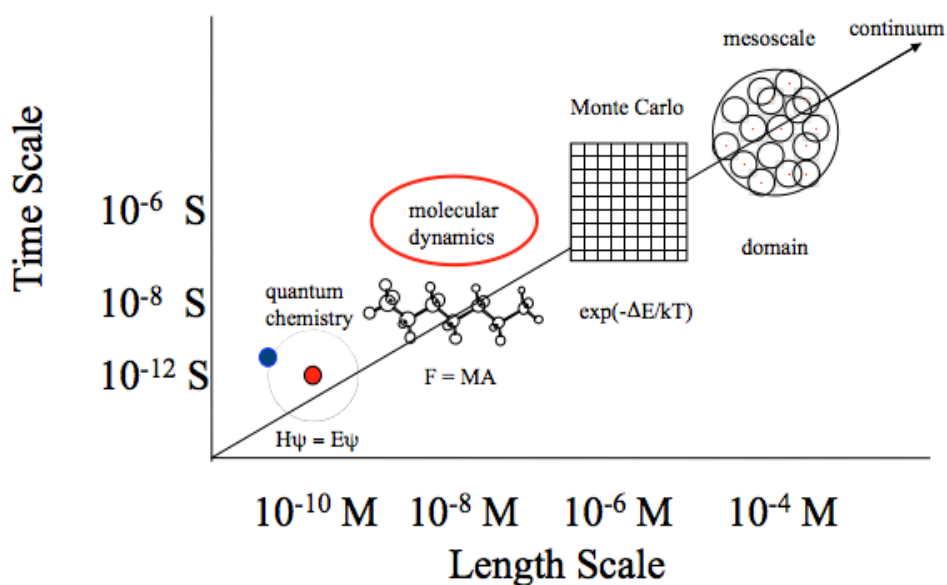
Figure 12 Time scale in simulations

2.3. Modeling Of Amorphous Nanoalloys

Within the scope of this study, one of the most important components in establishing the structure-property relations of amorphous-crystalline nanoalloy particles is the

study of amorphous nanoalloy particles. Amorphous nanoalloy particles have not ranked high in the literature to date, but nowadays they started to gain importance and will become a very important class of materials in the near future. Due to their short-scale structures, nanoparticles have a non-equilibrium behavior and can exhibit quite different properties compared to bulk specimens. Amorphous metallic alloys exhibit electronic, magnetic, mechanical and such other behavior different than their bulk and crystalline counterparts. This shows that combining nano-scale and amorphous structure properties may present many unprecedented novel behaviors. It can be thought that having these two structural properties together can make it more difficult to inspect these materials and complicate the explanation of related mechanisms. In this context, theoretical methods and simulations carried out establish a very important step understanding the formation mechanisms of amorphous nanoalloys.

2.4. Methodology

2.4.1. Building Amorphous Nanoparticles

The method to follow in realizing the (MD) simulation of a crystalline nanoparticle is to form the alloy with the cell structure decided and, if desired, to run thermal relaxation simulations to eliminate the surface tension. Of course, it should not be forgotten that it is accepted that the crystal structure of the alloy is the same as its bulk counterpart. Although this may not hold true for particles with less than 100 atoms, particles with more than 100 atoms generally maintain the crystal structure of their bulk counterpart.

As the particles to be studied in this study are at least 1 nanometer in diameter, these nanoparticles are assumed to have the same cell structure. On the other hand, simulation of amorphous nanoalloy particles may require a slightly different procedure than their crystalline counterparts. This is because producing amorphous nanoparticles by cooling down from a liquid phase have importance in imitating the production of real alloys. In this context, the procedure to be followed is as follows:

- Carrying out a bulk (periodic) simulation from which the amorphous nanoparticle is extruded figure 13.

- Melting the extruded nanoparticle.

- Equilibrating the molten nanoparticle, bring it to room temperature in stages at a cooling rate as decided.
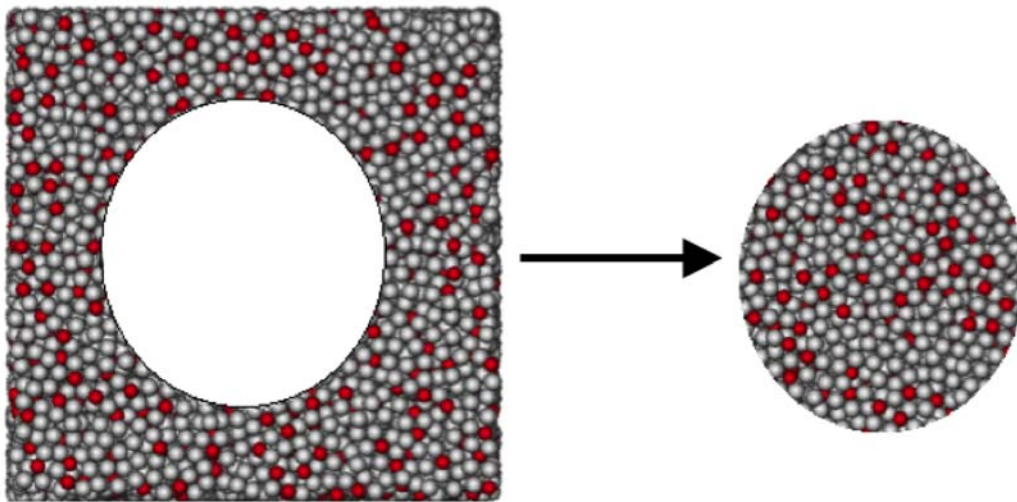
Figure 13 The first particle is cut out of a bulk (periodic cell) for the amorphous nanoparticle simulations.

The reason for following this procedure is, by eliminating the local atomic memory effects that may come from the crystalline counterparts or the structure in the solid phase, to bring the system from liquid to solid in a completely stochastic manner, and if there is to form a local atomic order, this atomic order to form by itself and not to be influenced by the past of the alloy. It is known that in amorphous alloy simulations, systems in liquid phase not brought to equilibrium to a sufficient degree, maintain the local atomic configurations originating from the solid phase not broken down during the melting stage. The time scales that is applicable in molecular dynamics and similar methods, is much different than the time scales involved in the

real experiments. In reality, for the liquid to come into equilibrium, there is enough time in all-practical conditions; however, a time period in the order or nanoseconds is not sufficient for the complete decomposition.

Another important point in the second stage is that, as the atoms on the surface of the nanoalloys have unsatisfied bonds, with an elevation of temperature, these surface atoms may achieve very high-level vibrations and blast off at high speeds from the particles. This cause the chemistry of the particle to change, and in turn, considerably reduce the trace ability and comparability of structural, thermodynamic and dynamical variables. In order to prevent this, when the particles are molten they are taken inside a virtual "sheath". The only external effect by this sheath on the system is the vapor pressure it produces on the particle. The sheath has been designed as a sphere, which is 1-2 Å greater than the particle, and it provides the atoms escaping from the surface to be re-integrated with the particle.

During the preliminary studies, it is observed that the vapor pressure does not have a large effect on the results, but is very beneficial in eliminating the probable errors and problems in (MD) simulations and analyses. This sheath has been formed by application of a force inwards at a distance from the particle surface. The force has the following form.

$$F(r) = -K(r-R)^2 \qquad\qquad \text{Equation 4}$$

In this formula, F, K, r, and R represent the force the sheath applies on the particle, force constant, particle radius and sheath radius, respectively. The last of the stages mentioned above is also of considerably high importance. It is required that, when the particle is cooled down from liquid to solid phase, the cooling rate must be absolutely computable, and for this, it should be cooled in stages with equal steps. For getting structural and thermodynamic data at predetermined temperatures during this cooling operation, the system is required to reach equilibrium at those temperatures due to the nature of constant temperature (NVT, NPT, etc) MD

simulations. For this reason, the cooling procedure is carried out in stages as shown in figure14.
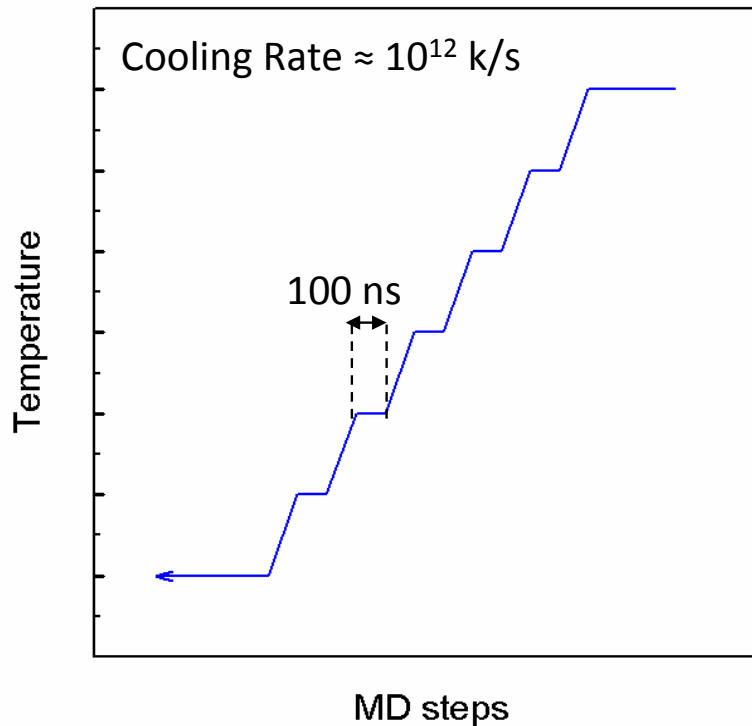
Figure 14 Liquid-to-glass cooling procedure to produce amorphous nanoparticle and a bulk (periodic) system setting a reference.

2.4.2. Glass Transition Temperature of Amorphous Nanoalloys

As thermodynamic variable, the glass transition temperature is still not completely understood. Today discussions go on whether glass transition is a kinetic phenomenon or it really is a "second-order" phase transition. The main reason for these discussions is that glass transition has not been explained at atomic level or electronic level as solidification, melting, vaporization, sublimation, magnetic and electronic transitions and such other transformations.

The chaotic appearance of amorphous materials at the mesoscopic level, the great variation of structural properties among systems, the difficulties in making and repeatability of the measurements (structural, thermal, viscosity, etc. particularly in undercooled liquid region) make it difficult to throw light on this phenomenon. From this point of view, it is not surprising that there is no information today on the structure of nanoalloy metallic glasses.

When talking about amorphous nanoalloys two important matters come to mind. First matter is as follows. Glass transition and amorphous structure are topics, which are more complex compared to crystals and not examined in detail at all by the "physics/chemistry sciences". Adding on top of these, the constant size and surface area, the behavior that may be exhibited will further complicate these studies. The second matter is that, even if these alloys can be produced experimentally, neither they exactly follows the thermodynamics laws, which work at the macro levels, nor they enable thermal/ spectroscopic/ dynamical analyses in respect to stability at room temperature. Therefore, as of today, the only systematic way to examine the properties of amorphous nanoalloys is goes through theoretical methods.

2.4.3. Study of the Relation between the Surface Energy and Atomic Structure in Amorphous Nanoparticles

Surface energy (SE) is maybe the most important physico-chemical properties of any nanoparticle system. This is because the potential applications of nanoparticles (catalyst, transporter, etc.) are directly related with the level of surface tension. Furthermore, as SE reflects the stability of the surface, it influences the stability of the particle, tendency to oxidation or degradation, and such other properties. In this regard, it is inevitable to examine the nanoparticles that we analyzed structurally for the change of surface energy with particle size and temperature.

As they contain a limited number of atoms, nanoalloy particles or, in general, nanoparticles of any kind, may not always follow the definitions of thermodynamic variables. Therefore, it will be useful to describe how the parameters and values used here have previously been calculated. In surface energy calculations carried out in this study , SE has been calculated as shown below.

$$\gamma = \frac{1}{4\pi r^2}\left(E_p - \frac{N_p}{N_b}E_b\right) \qquad\qquad \text{Equation 5}$$

Here, r represents the nominal radius of the particle, Ep and Eb represent the energy of the particle and its bulk counterpart, respectively, Np and Nb represent the number atoms present in the particle and its bulk counterpart, respectively.

The reason why the particle radius was taken as nominal, the particles, particularly small ones (1-2 nm), do not necessarily maintain their spherical shapes and become deformed. Relatively larger particles maintain sphericity in most of the time.

In condensed matter (liquid, solid, etc.), the change of surface energy with temperature is correlated with the excess surface entropy as follows:

$$\frac{d\gamma}{dT} = -S_{surf}^{E} \qquad\qquad \text{Equation 6}$$

2.4.4. Voronoi Analysis in Amorphous Nanoalloys

A proper way for examining the atomic structure may be to break it into parts at different scales and, starting with the smaller parts, to produce a cumulation of information at each scale. The smallest structural unit that we are interested is a single atom and the local surroundings that touch it. This phenomenon can be mathematically formulated by compartmentalizing the 3-dimensional Euclidean space into convex polyhedral via Voronoi analysis.

Voronoi analysis gives the statistical distribution of the polyhedral structure that is formed by the atom and its neighbors around. This statistical distribution is given by the commonly used polygonal notation <n3, n4, n5, n6, n7, n8, ...> where the number ni represents, in that polyhedron, the number of the edge surfaces having i corners.
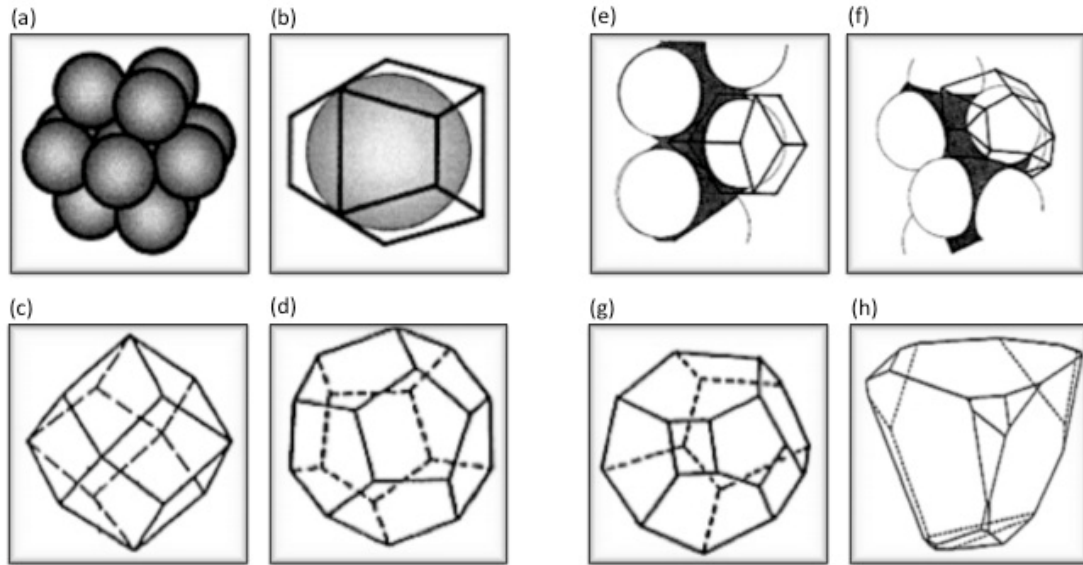
Figure 15 Voronoi polyhedra: (a) hcp packing of spheres (3+6+3 touching neighbors), and (b) the corresponding Voronoi polyhedron in the shape of truncated hexagonal prism, (c) Voronoi polyhedron corresponding to fcc packing arrangement (4+4+4 touching neighbors), (d) Voronoi polyhedron corresponding to dodecahedral arrangement (1+5+5+1 touching neighbors); (e) in crystalline polyethylene, comprising one carbon and two hydrogen Voronoi polyhedra, and (f) in amorphous polyethylene, (g) and (h) examples of atomic Voronoi polyhedra for random, disordered packing, (e) with 8 touching neighbors, (h) with 6 touching neighbors (Stachurski, 2003)

Voronoi polyhedral are the counterparts in the amorphous structure of the Wigner-Seitz cells in crystal structure.

2.5. Molecular Dynamics (MD) Simulations of Amorphous Iron-Boron Nanoalloys

$Fe_{80}B_{20}$ system has been previously examined by MD simulations by Aykol who worked in our research laboratory (NOVALAB) under supervision of Prof. Dr. Amdulla Mekhrabov and Prof. Dr. Vedat Akdeniz. In this study, the aim was to examine $Fe_{85}B_{15}$ system by the same methodology used by Aykol. However, before proceeding to the $Fe_{85}B_{15}$ system, the study on $Fe_{80}B_{20}$ system has been repeated to gain experience and a good understanding of the methods developed in our research laboratory. In this study, I reproduced exactly the same results as Aykol. As these results originally belong to Aykol, here I share his results with permission.

47

Amorphous $Fe_{80}B_{20}$ alloy has been selected to study due to its soft magnetic behavior in tape and bulk forms, very high strength and hardness and acceptable ductility.

If the amorphous structure can be maintained to some degree in the nanoparticle scale, we think that $Fe_{80}B_{20}$ and $Fe_{85}B_{15}$ nanoalloy particles will exhibit considerably interesting behavior magnetically and electrically.

In the experimental part of this project, the same nanoalloys has been produced using high-energy ball milling method and it is observed that very useful data have been produced along with the simulation part of the study.

2.6. Results and Discussions

2.6.1. The structural Properties of Amorphous Iron-Boron Nanoalloys (Radial Distribution Functions)

Phase transformations in nanoparticles quite different than their bulk counterparts in all measurable properties that they exhibit. One of the most important of these properties is the radial distribution function (RDF), which shows the spatial distribution of atoms with respect to each other. In figure 16, partial RDF's of 4 nm $Fe_{80}B_{20}$ nanoalloy particle at several different temperatures was shown same thing was shown for $Fe_{85}B_{15}$ in figure 17. Even though the outer parts (shells) of the particles are in molten state at high temperatures, probably due to the atomic order of the inner parts of the particle, this atomic order is generally maintained even in the liquid state.

At high temperatures, the peak positions remain the same, only that they become shallower as expected from a liquid structure. As the temperature is lowered, the wells between the peaks get deeper but their positions remains constant. In all of the Fe-Fe, Fe-B and B-B RDF's, particularly the near neighbor peaks shows not much of a shift; however, their heights change significantly.

But of course there are certain peaks showing apparent tendencies. For example, second and third peaks, which give characteristic information on amorphous metals, exhibit significant shifts with temperature. The second peak of Fe-Fe RDF shows

changes in the relative positions of the non-neighboring atoms but within the same cluster. As the temperature is lowered this peak shifts towards left, which means the clusters of the existing configurations get increasingly compact structures.
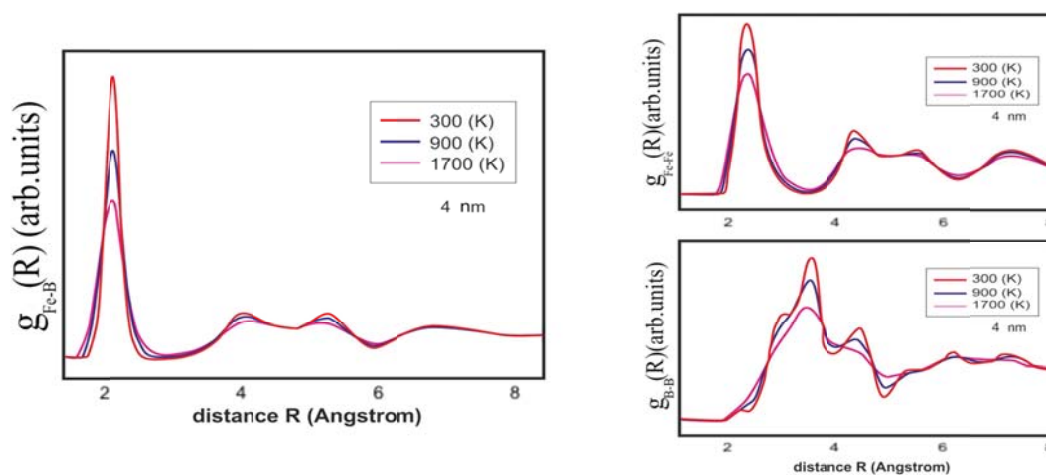
Figure 16 Change of the partial RDF's with respect to temperature for 4 nm sized $Fe_{80}B_{20}$ nanoalloy particles Fe-B, Fe-Fe and B-B (Akdeniz et al., 2013).
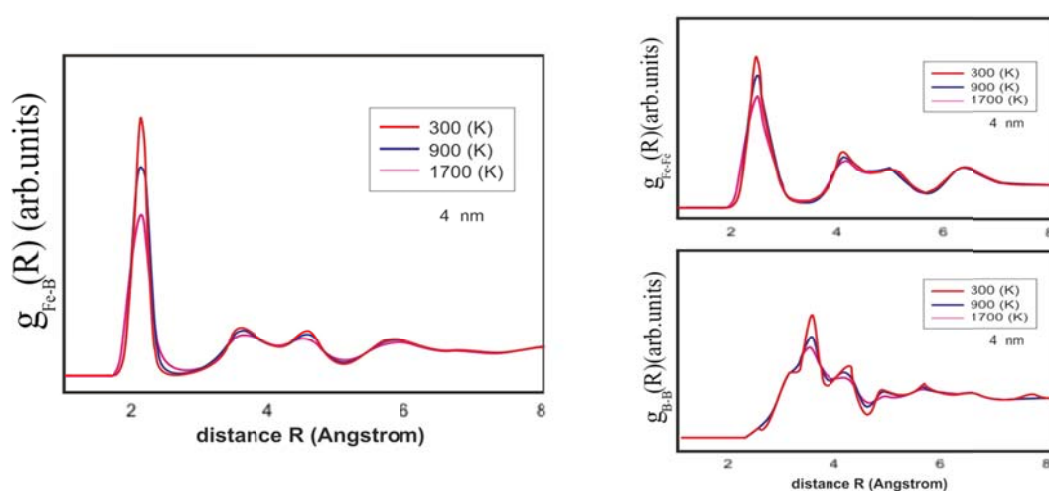
Figure 17 Change of the partial RDF's with respect to temperature for 4 nm sized $Fe_{85}B_{15}$ nanoalloy particles Fe-B, Fe-Fe and B-B.

2.6.2. Morphological Study of the Amorphous Fe-B Nanoparticles

The amorphous nanoparticles, which are much less stable than the crystal nanoparticles, exhibit quite different properties morphologically too. In $Fe_{80}B_{20}$ alloy, at 300 K, the particle loses its spherical shape starting from the initial stages and takes an ellipsoid form in progress of time.

Consistent with our group earlier studies on bulk alloys, nanosize phase separation causes Fe atoms in excess to cluster and to diffuse to the particle surface, through which Fe and B regions are separated from each other figure 18.
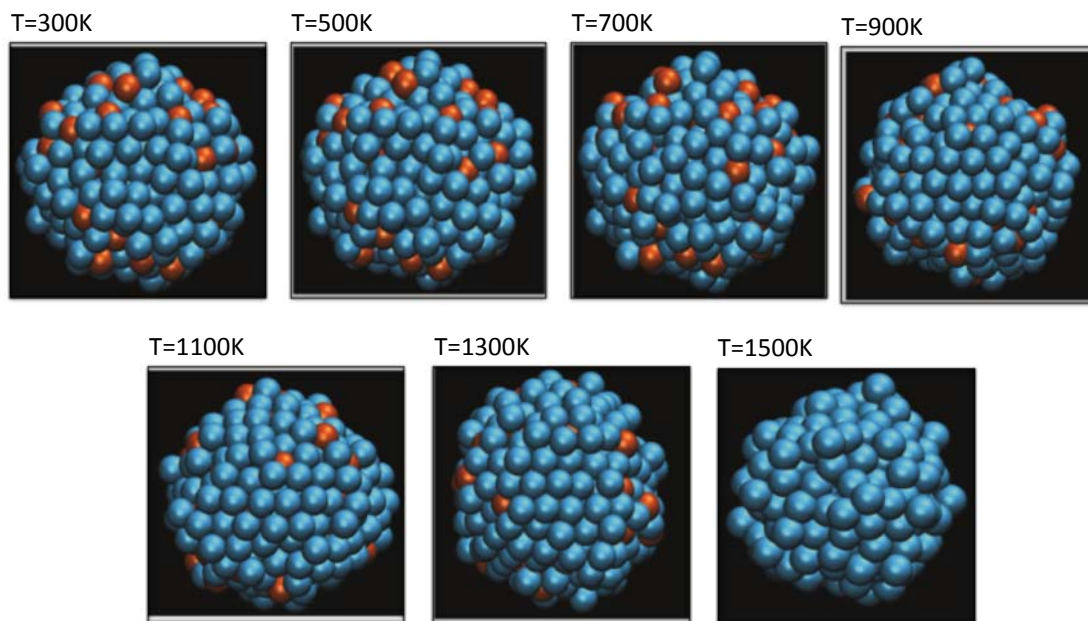
Figure 18 The structural transformations of the nanoparticles as the temperature rises. The Fe atoms gathered on the surface is shown (Akdeniz et al., 2013).

This separation starts at a temperature of 300 K and becomes more pronounced at higher temperatures. At temperatures lower than 900 K, the Fe regions show more

disordered structure than the other parts. Even though Fe-Fe binary potentials stabilize the bcc structure in bulk alloys, this closed packed structure is stabilized in cluster and unsatisfied Fe bonds and definitely start at the surface.

This crystallization shows the bond energy of the system is reduced. Starting from a temperature of 1300 K, Fe atoms start to escape from the nanoparticles surface.

At that temperature, some Fe atoms gather at the surface of the particle and forms closed packed arrangements. At 1500 K and above, this arrangements break down and the surface liquefies.

2.6.3. The Atomic Distribution Profile From The Core To The Surface In Amorphous Iron-Boron Nanoalloy Particles

In order to observe which types of atoms are concentrated in which parts of the particle and if there is a chemical decomposition, core-to-surface profiles of atom types are made for $Fe_{80}B_{20}$ and $Fe_{85}B_{15}$ nanoalloys of several different temperature.
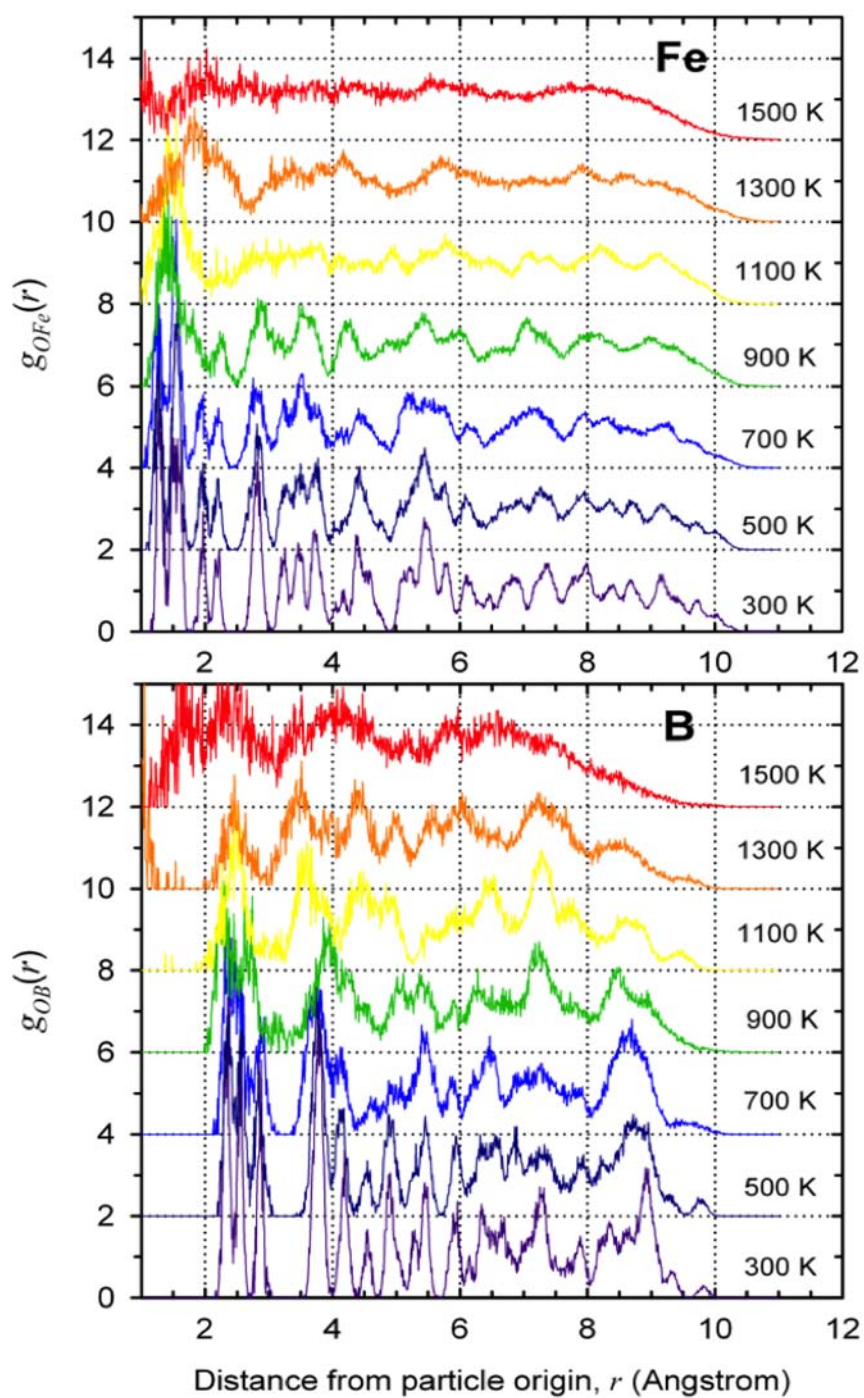
Figure 19 Atomic distribution profiles of Fe and B atoms from the core to the surface in a 2nm $Fe_{80}B_{20}$ nanoparticle (Akdeniz et al., 2013).
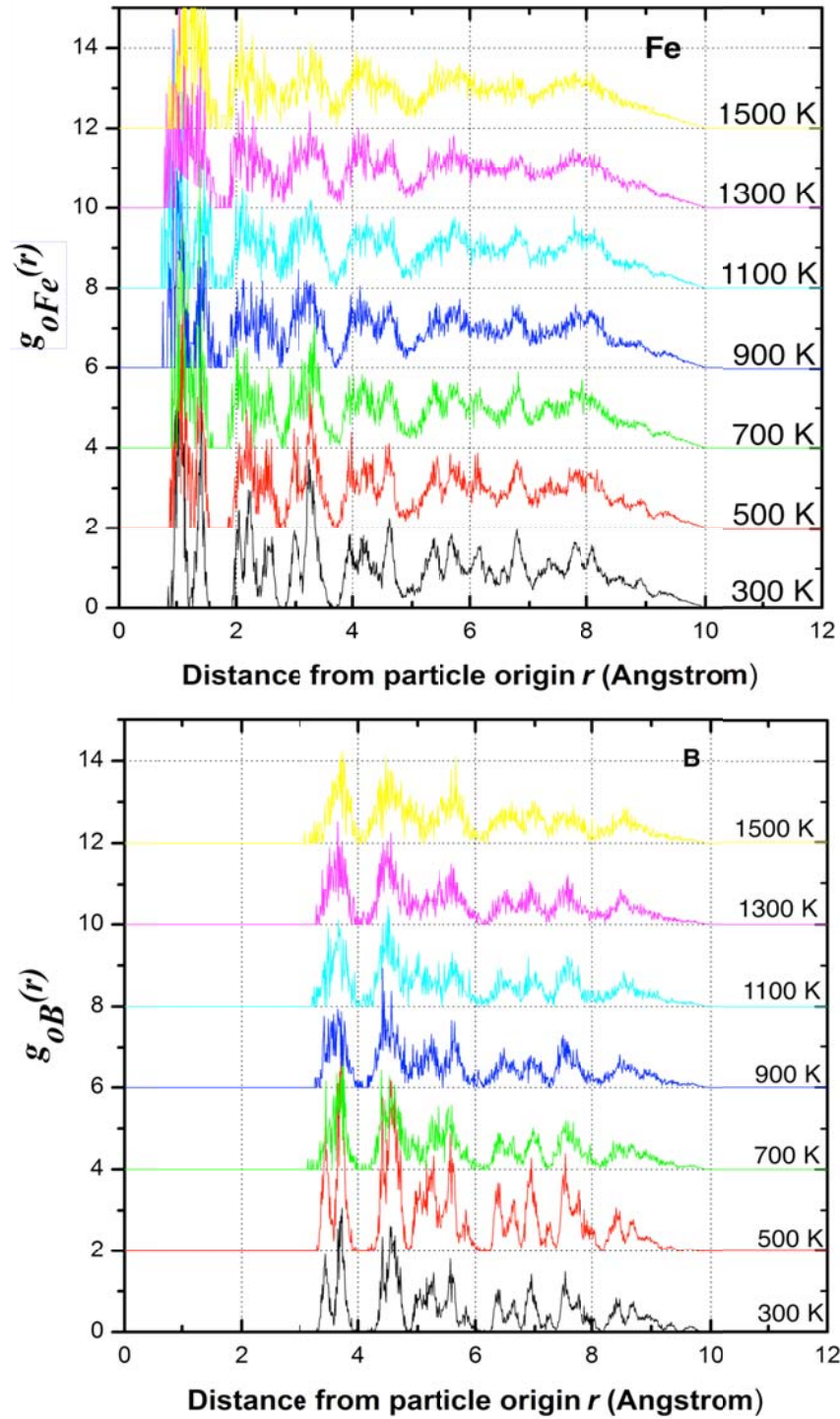
Figure 20 Atomic distribution profiles of Fe and B atoms from the core to the surface in a 2nm $Fe_{85}B_{15}$ nanoparticle.

The profiles shown in figure 19 and 20 are defined quite similar to the radial distribution function. The only difference is that, the first component in the radial distribution function is defined as the instantaneous geometric center; the other component is determined as either Fe or B. This can be summarized as calculation of O-Fe and O-B RDF's (O: geometric origin). Origin is taken as a fixed atom and the atomic density is calculated on this basis.

$$g(r)_{O-A} = 4\pi r^2 \rho\, dr$$

<div align="right">Equation 7</div>

In this formula O is the center of the particle taken as the origin, r is the distance from the origin, and ρ is the number of atoms per unit volume calculated at this distance.

This analysis is done by a computer program written in GNU Octave and it calculates gO-A(r) function, which we define as an analog of RDF function. GNU Octave is a high-level interpreted language, primarily intended for numerical computations. It provides capabilities for the numerical solution of linear and nonlinear problems, and for performing other numerical experiments)

The distinctive property of gO-A(r) function from RDF function is the first component in the partial radial distribution function is defined as the origin, and the other component is taken as one of atoms. The most important result here is that it is easy to observe the differences in the way that the atoms are distributed within the particles as the temperature is varied. As can be seen in figure 18,19 and 20, at high temperatures, B atoms are placed beneath the surface and whole surface is surrounded Fe atoms in molten state. Accordingly a core-shell structure with B core and Fe shell is observed at high temperatures.

2.6.4. Study of the Relation between Surface Energy and the Atomic Structure in Amorphous Iron-Boron Nanoparticles

Again a general observation for the condensed matter (solid or liquid) is that the slope is negative, in other word, SE is decreased as the temperature rises.

$$\frac{d\gamma}{dT} = -S_{surf}^{E} < 0 \qquad\qquad \text{Equation 8}$$

When compared to the atoms located at the inner parts, the atoms on the surface having smaller number of neighbors and a looser structure. So it explains why the surface atoms form regions with higher entropy than the inner atoms. In crystalline materials this kind of behavior is observed.

We expect considerably interesting results in this part of the study. As shown in figure 21,and 22 $Fe_{80}B_{20}$ and $Fe_{85}B_{15}$ alloys, either in bulk or nanoparticle form, exhibit a positive slope particularly in the liquid phase and up to the glassy phase as in.

$$\frac{d\gamma}{dT} = -S_{surf}^{E} > 0 \qquad\qquad \text{Equation 9}$$

This behavior, which is in contrast with the conventional materials, is found interesting and deemed worthy to examine. In nanoalloy $Fe_{80}B_{20}$, $Fe_{85}B_{15}$ particles in amorphous/liquid structures and bulk alloys, surface topology exhibit significant changes when compared to the topology of the atoms located at the inner parts, different atomic arrangements and more closed packed configurations exist on the surface. Only in this way, surface entropy can reach lower levels compared to inner parts of the material and the $-S_{surf}^{E} > 0$ case can take place.

In addition to this, another anomaly is with the differences between the levels of surface energies. As can be seen in figure 21 and 22, the bulk system has the highest surface energy at all temperatures, in figure 21, 4 and 6 nm particles have roughly the same level of surface energy, and lowest surface energy is observed in the smallest particle at a size of 2 nm.

In order to understand both anomalies, it is necessary to shed light on the underlying structural phenomena.
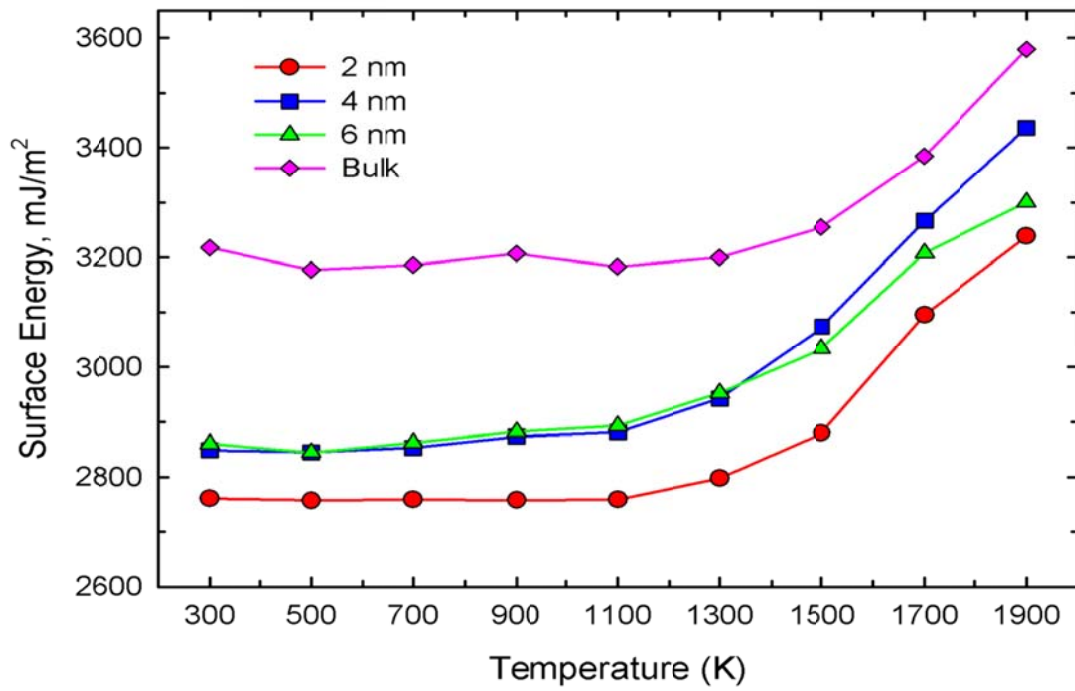
Figure 21 Change of surface energy with temperature in $Fe_{80}B_{20}$ nanoalloy particles (Akdeniz et al., 2013).
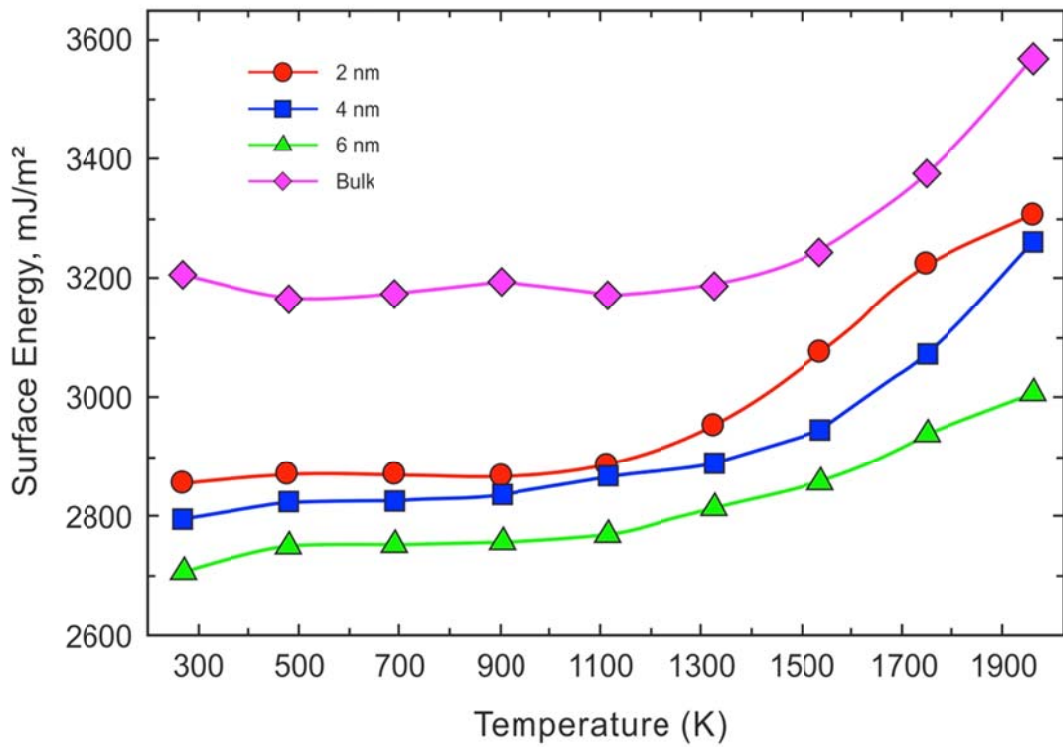
Figure 22 Change of surface energy with temperature in $Fe_{85}B_{15}$ nanoalloy particles.

2.6.5. Morphological Dynamics Of Amorphous Iron-Boron Nanoalloy Particles

Nanoalloy particles, particularly because they are amorphous, are in a more unstable state then their crystalline counterparts. In this regard, it is apparent that these particles, during MD simulations, will seek several ways to become more stable like changing shape, density, atomic configuration, etc. This effect can first be seen in the changes in particle geometry starting already in the liquid state. In figure 23, 24, 25 and 26 the change of the geometric form with time of 2 nm $Fe_{80}B_{20}$ and $Fe_{85}B_{15}$ nanoalloy particle is compared with its 6 nm counterpart. Particle with 2 nm size shows a significant change compared to its state when it was cut out from the bulk structure. First of all, the particle loses its sphericity, and takes a structure with straight features, which is formed with facets. This means that the particle is at a size, which makes it possible to transform geometrically to a more stable structure from its initial form. In contrast, the 6 nm particle, even when it is in molten state, does maintain its sphericity; however, it exhibits changes in the atomic concentrations on the surface. Hence, the 6 nm particle does not have the freedom to geometrically adapt as the 2 nm particle. Therefore, even in the liquid state, the surface of the small particle takes a more stable form, and its surface energy per unit area is lower than that of the large particle. In the 6 nm particles, it is probable that the surface takes a topologically more stable form than the bulk interior; therefore it, too, has negative entropy S_{surf}^{E} although the level of surface energy per unit area is still higher than that of the 2 nm particle.

This effect was carried to the glassy phase and this can easily be seen on the surface energy – temperature curve in figure 22. This can be clearly understood by visually examining the geometry of the 2 nm particle now in the glassy state. The 2 nm particle is in a nonspherical form at room temperature just as in the liquid state, and it features phase separation in density at an atomic level and surface rearrangements following this phase separation. The particle is separated into two regions, one with high Boron concentration and the other with high Iron concentration, and possesses significant similarities with bulk simulations of this type of alloys. The extra energy added to the system by a fixed surface area makes such nano-scale phase separation even more probable. On the particle surface with high Boron content, rearrangements

take place as pentagons of Fe around a Boron atom. On the other hand, on the region with high Iron content, closed packed iron facets are formed apparently. As these closed packed arrangements are not present at the inner parts of the particle, topologically the surface has lower entropy than the inner parts of the particle and S_{surf}^{E} has a negative value. In large particles, this type of phase separation is not observed and therefore iron atoms cannot form ordered atomic configurations and facet-like geometries. That's why surface energy of a small particle is at a lower level than that of larger particles. As can be understood from the surface energy – temperature curve in figure 21 and 22, 4 and 6 nm sized particles do not show much of a different surface energy behavior than each other. This effect is observed only in the 2 nm particle, which enables facet formation, shape deformation and great changes in the surface topology.
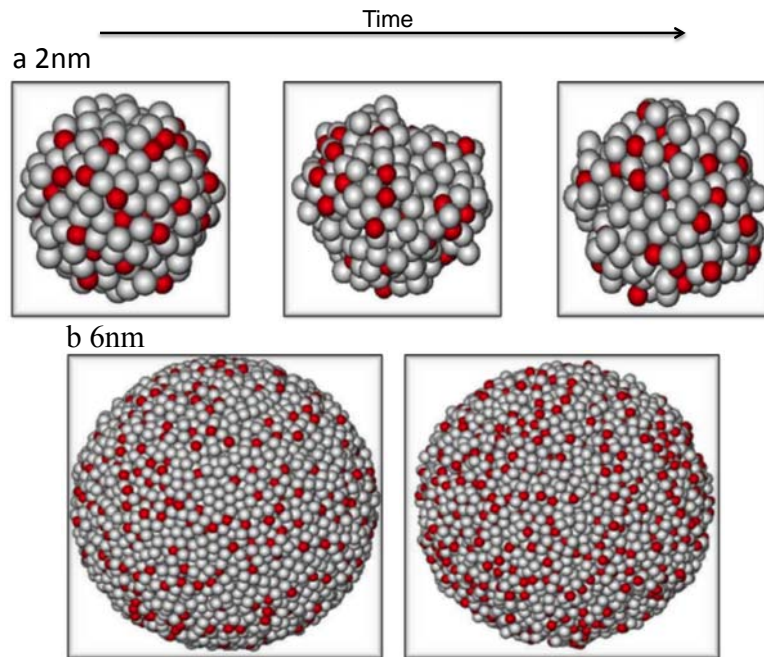
Time

a 2nm

b 6nm

Figure 23 The changes exhibited by $Fe_{80}B_{20}$ nanoalloy particles in liquid state in time for (a) 2nm and (b) 6 nm in diameter. 2 nm particles goes through a geometric deformation and takes a shape that better suits it. On the other hand, 6 nm particle maintains its spherical form and shows only minor changes in surface density (Akdeniz et al., 2013).
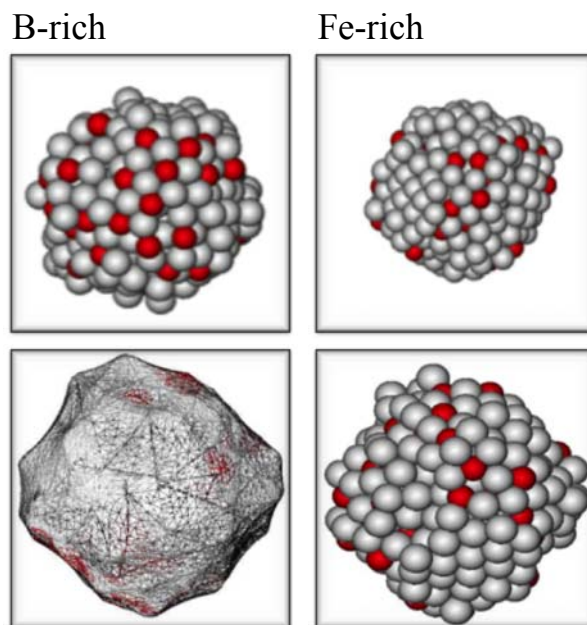
B-rich   Fe-rich

Figure 24 Chemical (atomic) phase separation exhibited by 2 nm $Fe_{80}B_{20}$ nanoalloy particle. B-rich and Fe-rich regions are shown and ordered atomic arrangements are apparent. For this reason, particle lost its sphericity and took a faceted structure (Akdeniz et al., 2013).
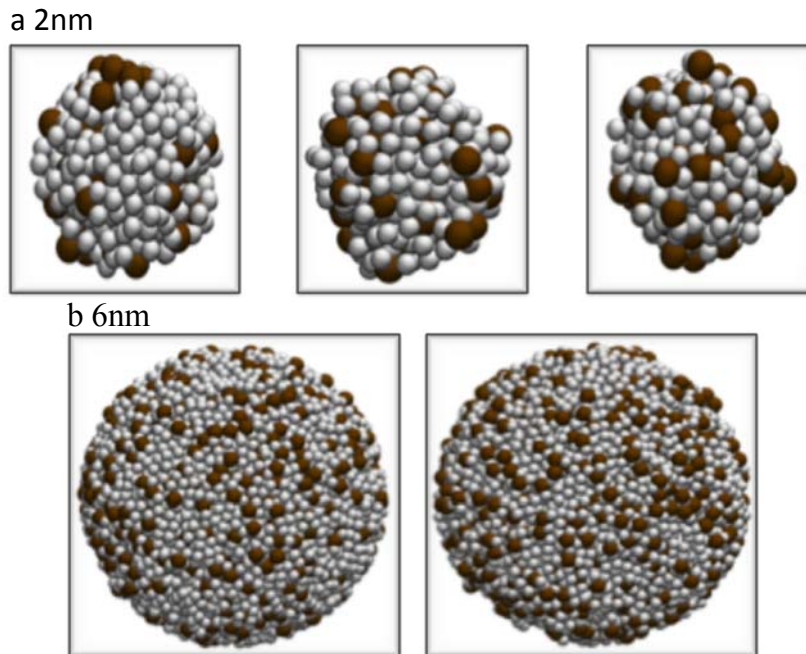
a 2nm

b 6nm

Figure 25 The changes exhibited by $Fe_{85}B_{15}$ nanoalloy particles in liquid state in time for (a) 2nm and (b) 6 nm in diameter. 2 nm particle goes through a geometric deformation and takes a shape that better suits it. On the other hand, 6 nm particle maintains its spherical form and shows only minor changes in surface density.
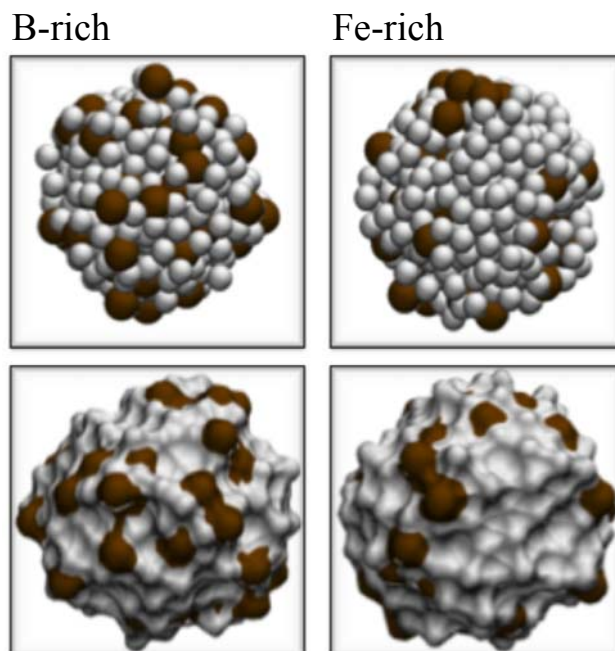
B-rich   Fe-rich

Figure 26 Chemical (atomic) phase separation exhibited by 2 nm $Fe_{85}B_{15}$ nanoalloy particle. B-rich and Fe-rich regions are shown and ordered atomic arrangements are apparent. For this reason, particle lost its sphericity and took a golf balls structure.

2.6.6. Voronoi Analysis in the Amorphous Iron-Boron nanoalloy particles

Fe-centered Voronoi analyses of 4 nanoalloy particles in liquid and amorphous state are given in figures 27 <0,2,8,4> and <0,3,6,4> polyhedra and following derivatives (<0,2,8,5>, <0,3,6,5> and <0,3,6,6>) are polyhedra that represent deformed body centered cubic (deformed BCC) structures in Voronoi diagram of Fe. Also observed are structures like deformed icosahedral (D-ICO) <0,1,10,2> and <0,2,8,2> structures. Pure BCC <0,6,0,8> and pure icosahedron <0,0,12,0> structures are observed but they are rather low in numbers. Their deformed forms are the predominant ones.
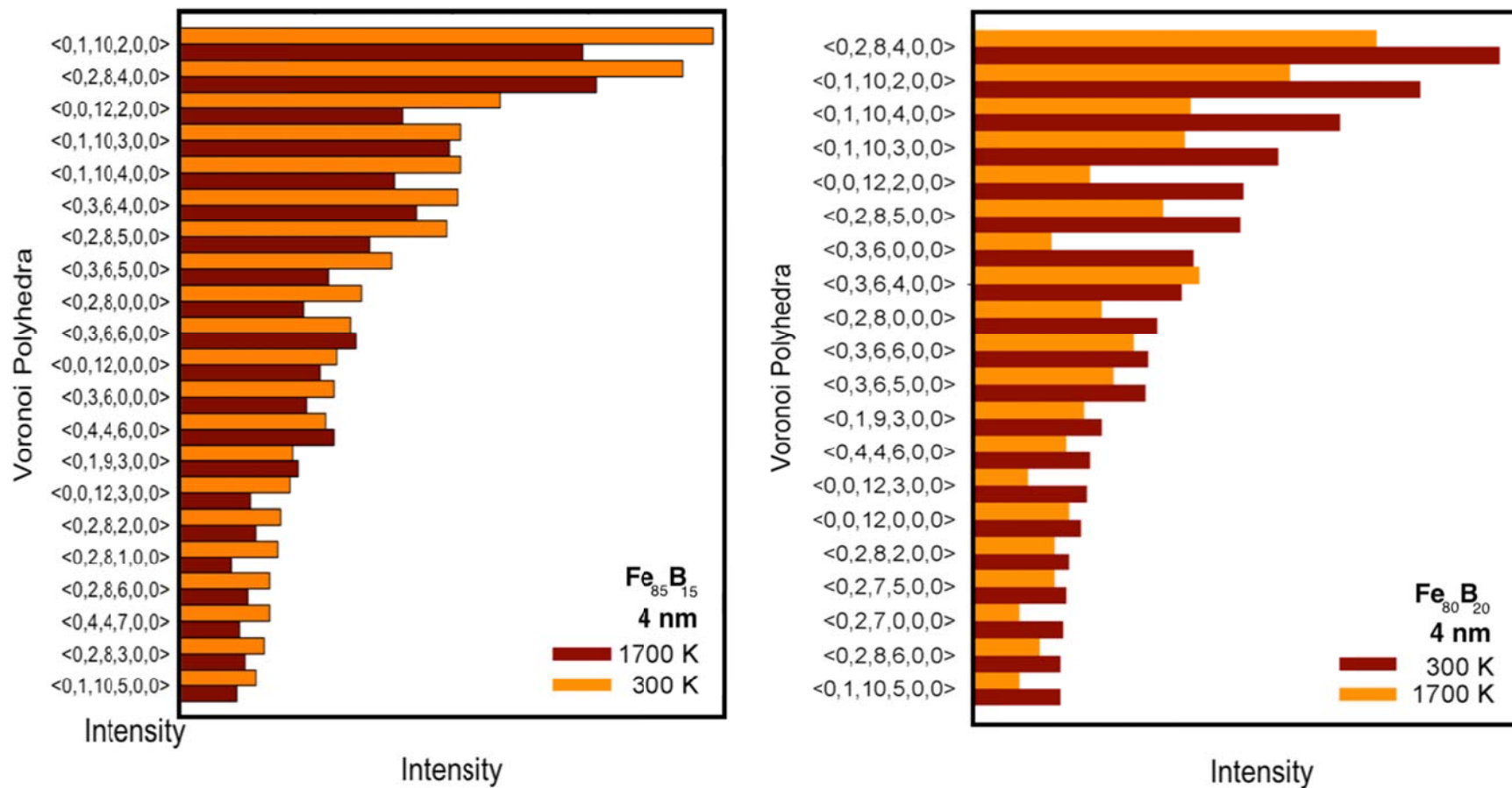
Figure 27 Fe-centered Voronoi analysis of 4 nm sized $Fe_{80}B_{20}$ (Akdeniz et al., 2013) and $Fe_{85}B_{15}$ nanoalloy at temperatures 1700 K (liquid) and 300 K (glass)

CHAPTER 3

EXPERIMENTAL STUDY

3.1.   Introduction

Ball milling process is a typical grinding method, which were used to broken down the coarse powder to finer particles under the impact of the balls figure 28. It is usually used to prepare nanostructure materials and produces the particles with a very wide size range from several microns up to few nanometers. The effort always down to break up the nanoparticles with the required size from the rest. To obtain this goal several methods were employed like filtering, sedimentation etc. The main problem in filtering technique is the jamming of the filter however if the size selection could be possible in this technique it seems very useful and attractive method for nanoparticle production. Ball milling could be use for producing the particles, which cannot be produced with other technique, this is one of the advantages of this method. Also with it metastable phases can be produced, which would not be possible in other techniques this is another advantages of this technique. Moreover, the process would be much easier, and has outlooks for commercialization since several industries carry the ball milling facilities for high volume processing of materials.
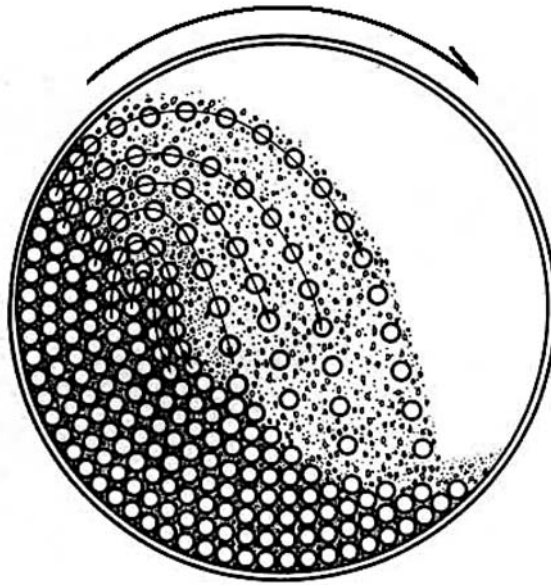
Figure 28 Schematic of inside planetary ball mill

Both milling and cold-welding happens simultaneously during the milling process but with different extents as a result required particle sizes could be achieved by controlling these two.

Depend on the type of mill which were used the impact of the balls can be adjusted. In case of dry milling just balls and powder are put in to the bowel. Then due to the Van der Wall forces agglomeration of the particles were happened. By reducing the particles size the surface energy and hence the Van der Wall forces increase dramatically. Consequently the particles willing to remain agglomerated with other particles. As the milling precede most of these small particles get alloyed with other particles and bigger particles produced. The size rang is very from 5 to 100 microns with nano-sized grains depending upon the material in this method. Also the distribution of the obtained particles size is very wide.

The effect of alloying can be reduced if the milling was accomplished in the presence of appropriate solvents. To further reducing the effect of alloying surfactant must be added to solvent. These two, solvent and surfactant, are named surface-active agents (Cao, 2004, Suryanarayana, 2001). Surfactant covers the surface of the particles that

interferes with cold welding and reduces the surface tension of solid material. Also it lower the required energy for creating the new surfaces then it helps to producing the finer powders (Cao, 2004, Suryanarayana, 2001) Moreover it also helps to scattering of the particles in the solvent.

3.2.   History

The surfactant first time was used with ball milling in 1965 to dispersed Fe_3O_4 nanoparticles (50-240 nm) in heptane as a solvent and oleic acid as a surfactant, in order to form a low viscosity magnetic fluid for space applications (Papell, 1965).

Same technique extensively used for preparation of ferrofluids (Rosensweig, 1970, Lutful et al., 1999). Ferrofluids are magnetic nanoparticles, which coated with surfactant in a solvent and forms a colloidal suspension. Kaczmarek et al. (1990) and.Jayasuriya et al. (1993) investigated how different type of cationic and anionic surfactants affect on the Co-Fe-Si-B and Nd-Fe-B powders during milling and found that surfactants do help in achieving smaller particle size however did not make any notice about shaping of nanoparticles.

Tajima et al. (1995) investigated the effect of milling using surfactants on hard magnetic $Sm_2Fe_{17}N_3$ and has made a notice about magnetic 50 nm nanoparticles dispersed in the solvent yet no comprehensive dissection was displayed on it. The phase structure was discovered to be same at both nanoparticles and the beginning raw material, which is advantageous. SmCo nanoparticles (<25 nm) have been prepared by ball milling using phenoxyundecanoic acid surfactant Kirkpatrick et al. (1996) reported low coercivities for Sm-Co nanoparticles.

Liu and McCormick (1999) prepared Sm_2Co_{17} nanoparticles using mechanochemical process, the nanoparticles by this method exhibited very wide size distribution, which is typical of ball milling.

Beside all advantageous the ball milling method have some disadvantageous inherently like greater degree of contamination mainly from the milling balls and vial, development of defect structure or amorphization of the powder, and formation of metastable states due to impact of the balls (Suryanarayana, 2001), therefore this

method used to produce amorphous powder extensively. Controlled annealing procedures can eliminate these defects. To optimization of the process type of surfactants, its amount and other ball milling parameters like milling time, balls to powder ratio, extent of filling of the vial, milling temperature etc. can be varied. Proper selection of the surfactant is very necessary since it can be decompose and react with powder during milling and form compounds, which are dispersed in the powder particles as inclusions.

Carbohydrates, which contains hydrogen, carbon, and oxygen and Hydrocarbons by containing hydrogen and carbon are introduce carbon and oxygen in to the system that led to form oxides and carbides, which dispersed in the matrix (Suryanarayana, 2001). Also rare-earth compound like Nd-Fe-B and Sm-Co can form oxides easily, which can weaken the hard magnetic properties.

3.3. Amorphization

Mechanical Alloying (MA) and Mechanical Milling (MM) is used to prepare the amorphous phases; however it is not completely clear what is the mechanism of amorphization by these methods. Previous study (Ermakov et al., 1981, Ermakov et al., 1982) supposed that the reasons of melting of powder particles were the very high rate of plastic deformation and consequent rise in the powder.

Figure 29 shows the schematic free energy diagram. It indicates the criteria to be met for solid-state amorphization.

Metastable Crystalline Phase
Disordered Intermetallic
Layered system of two metals
Intermetallic phase + H_2 gas
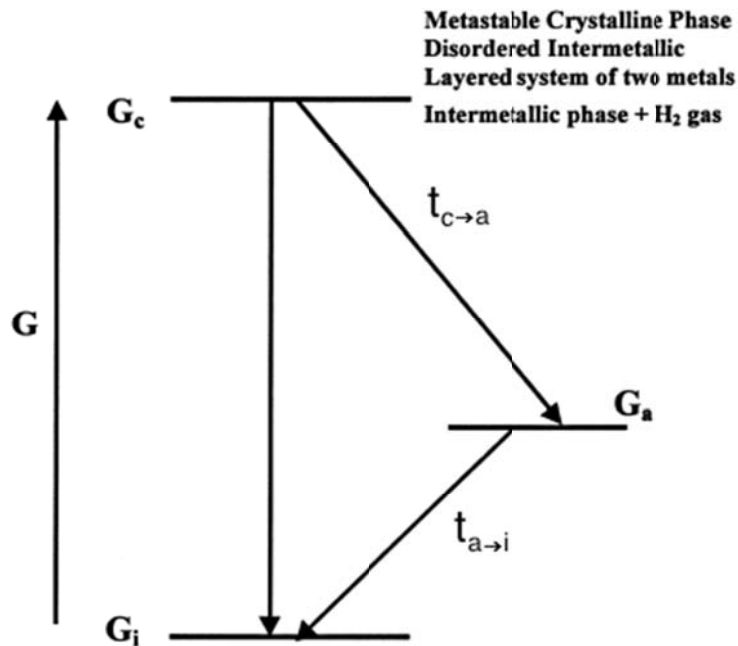
Figure 29 Schematic free energy diagram indicating the criteria to be met for
solid-state amorphization.

Formation of the amorphous phase is done by subsequent quenching of the liquid by
heat conduction into the less deformed, and hence cooler, interior regions of the
particles. Temperature measurements and calculations of energy input show that the
temperature increase is not large enough to melt the powder particles. Furthermore, if
assume that this mechanism were correct, the ranges of glass- forming composition
in mechanically alloyed and rapidly solidified alloys should be the same; but it is not
true. Researchers think that amorphization during MA and MM is not purely a
mechanical process and during MA and MM a solid-state reaction similar to that is
observed in thin films (Schwarz and Johnson, 1983). In addition it is conceived that
built-up of structural defects such as vacancies, dislocations, grain boundaries, and
anti-phase boundaries are in charge of destabilization of the crystalline phase.
Increase in free energy of the system (Gaffet et al., 1992) is due to ceaseless decrease
in grain size (and consequent increase in grain boundary area) and the lattice
expansion. Enthalpy of fusion is two times of the stored energy during MA, while
during cold rolling or wire drawing stored energy is only a small fraction of it

(Eckert et al., 1992). The free energy of the intermetallic system is raised by defects to a level higher than that of the amorphous phase; consequently the amorphous phase could be formed easily. It is reported that when the strain in the slow defusing species reaches a maxim level, amorphization occurs (Murty et al., 1992). For the ordered alloys, amorphization was reported to occur when the LRO parameter is <0.6 with a corresponding volume of expansion of about 2% (Massobrio, 1990). Amorphization has been caused by irradiation of crystalline materials by energetic particles and electrons when the following criteria are obeyed:

- The intermetallic compound has a narrow or zero homogeneity range,
- The order disorder transition temperature of the intermetallic, Tc is higher than the melting temperature, T_m
- The two components (elements) are separated by more than two groups in the periodic table,
- The intermetallic has a complex crystal structure
- The fraction of A atoms. $(f_A \geq f_B)$ is $\geq 1/3$.

When the above criteria were generally followed, intermetallic have also been amorphized by MM. Several exceptions change the above empirical rules. For instance, amorphization of compounds with reasonably wide homogeneity ranges. Or amorphization of a number of compounds with $f_A=1/4$ It is important to notice that the above criteria may only be used as guidelines and not that if they are obeyed, amorphization will be occurred.

Estimated elastic mismatch energy stored in an ordered solid solution is calculated by Beke et al. (Beke et al., 1991b, Beke et al., 1991a). This estimation is done when long-range chemical order of an ordered solid solution is destroyed. In this study they prove that amorphization is expected to occur because Tc> Tm (see the second condition above) and the ratio of the elastic mismatch energy to the ordering energy is high enough.

This is a valid criterion in many cases of amorphization observed by irradiation. Many attempts to estimate the ability of an alloy to become amorphous under MA/MM conditions have been made. Zhang (Zhang, 1993) used atomic sizes and

heats of formation and plotted .(R_A - R_B.)/R B (where R_A and R_B are the atomic radii of the components A and B, respectively) against ΔH, heat of formation of the amorphous phase, and observed that a straight line separate the regions between an amorphous phase and non-amorphous phase. Its equation is given by:

$$(R_A- R_B = \Delta R)/R= 0.068\Delta H + 0.716$$ Equation 10

The proportion of correct predictions for the glass-forming alloys and non-glass-forming alloys were 89.2% and 71.4% respectively. Amorphization is assumed through a theoretical model in which it is realized as an interstitial impurity formation during MA (Chakk et al., 1994). It was supposed that amorphization commence when impurity atoms penetrated into interstitial sites and distorted the lattice locally. The LRO of the lattice was destroyed when the local distortions reached some critical value, (destabilization of the crystalline phase) and an amorphous phase formed. The minimum concentrations of solute atoms, which is needed to amorphized a binary alloy system by MA, is strongly related to the atomic size ratio of the constituents (Egami and Waseda, 1984). For example, in fcc-based metal systems, an amorphous phase was formed by MA when the atomic size ratio was 0.68-1.83 and for bcc-based metal systems it was 0.66-1.31. It is shown that amorphization is promoted by large negative values of the interaction parameter ω_{AC} promote (Omuro and Hiromi, 1995). The interaction parameter ω_{AC} is given by the equation:

$$\omega_{AC} = RT\varepsilon_C^A$$ Equation 11

Where R is the gas constant, T is the absolute temperature, and ε_C^A is the interaction coefficient defined as $\varepsilon_C^A = dln\gamma_C/dX_A$ where γ_C is the activity coefficient and X_A is the atom concentration of component A.

3.4. Planetary Ball Mills

Planetary ball mill is one of the most popular mills for ball milling and mechanical alloying (MA) figure 30a. With this type of mill a few hundred grams of the powder

can be milled at a time. Fritsch GmbH in Germany and Gilson Co., in the US and Canada fabricated this type of milling equipment. Planet-like movement of its vials is the reason to call them planetary ball mill. These are designed on a rotating support disk. A particular drive method causes them to rotate around their own axes. This movement produces a centrifugal force, which acts on the vial contents, involving the materials to be ground and the grinding balls. While the supporting disk and vials rotate conversely, the centrifugal forces alternately act in like and opposite directions. This moves the balls downward on the wall of the vial milling the materials. This is called friction effect figure 30b. The balls then move freely inside of the vial chamber and collide against the opposite inside wall. This is called impact effect figure 30b.
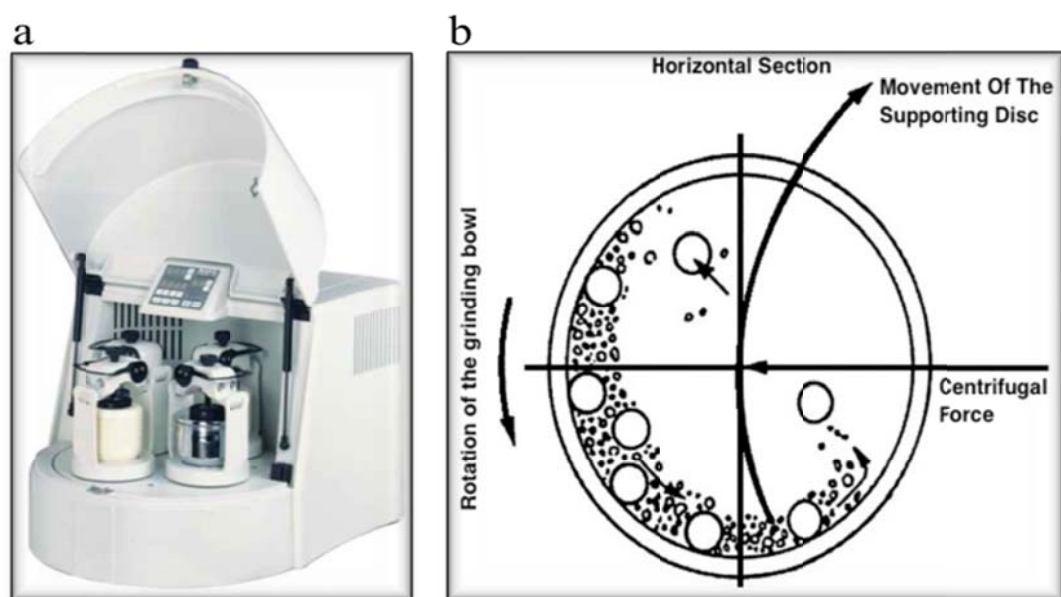
Figure 30 Fritsch Pulverisette P-5 four station ball mill. (b) Schematic depicting the ball motion inside the ball mill.

While the disk and the vial rotation speeds could not be independently controlled in the earlier versions, it is possible to do so in the modern versions. Grinding vials and

balls are available in eight different materials - agate, silicon nitride, sintered corundum, zirconia, chrome steel, Cr±Ni steel, tungsten carbide, and plastic polyamide.

In this study it is aimed to synthesize nanoalloy particles in FeB systems by using wet high-energy ball milling method with use of surfactants. Three different combinations of atmosphere controlled bowls and balls for the mill Fritsch Pulveristte 7 Premium Line were procured to employed in this study.

Initial experiments have been carried-out with the aim of learning about the equipment and setting the process parameters. In this regard, the experiments are being carried out within the capabilities of our laboratory. For these experiments we started to grind high purity 10-micron α-Fe powder. In this grinding process, the following parameters are experimented:

Figure 31 Fritsch Pulveristte 7 Premium Line High Energy Ball Mill, stainless steel bowls/balls with no controlled atmosphere**.**

Determination of Safety Measures: During high-energy ball milling, the most important points to remember are preventing overheating (> 80 – 90 °C) of the equipment and to prevent the excess pressure (> 20 bar) that may arise within the mortar.

When grinding for the first time for a new set of experiments:

- Sample
- Surfactant
- Amounts of Solvent
- Grinding time
- Cooling time
- Determination of grinding period
- Making the experiment flowchart / timesheet
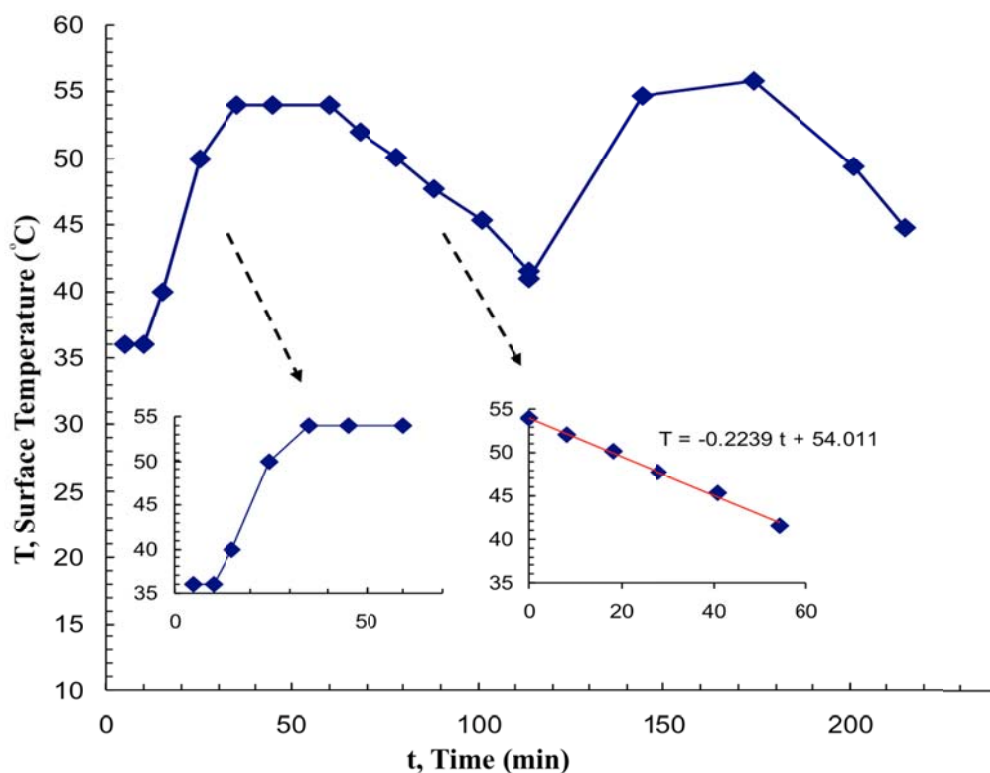
Figure 32 Periodic temperature measurements during grinding by Fritsch Pulverisette 7 Premium Line mill and standard (no gas control) stainless steel bowls/balls Increasing plots show the temperature levels during grinding and decreasing plots show the temperature levels during cooling periods.

In periodic temperature measurements carried out on bowl-ball-solvent-powder combinations used, the temperature does not reach the unwanted levels and is stabilized at around 55 °C for grinding operations exceeding 40 minutes, as can be seen in figure 32.

The cooling curve for the bowl also follows a linear trend, thus it is possible to predict the amount of cooling for any given period of time by using the linear equation given in figure 32. In light of these data, for the present experiment combination, we decided that cycles including 1 hour grinding and hour cooling could be carried out with no danger. These experiments were only to learn about the equipment and practice its performance.

73

3.5. Grinding Pure Iron Powders

During the initial experiments carried out in order to learn about the equipment, to determine the safety measures and to prevent overheating and excess pressure in the bowl, grinding processes were experimented with high purity α-Fe powders.

In this study, in order to determine the process parameters, such as grinding time, type and amount of the solvent and rotation speed, and to research the effect of these parameters on particle size, particle shape and magnetic properties, high purity iron powders are ground under controlled atmosphere.

3.5.1. Grinding Process Using High Energy Ball Mill

The iron powders (Alfa Aesar) ground in this study were higher than 99% in purity and 70 μm in average particle size, figure 33. Grinding process was carried out in a high energy ball mill (Fritsch Pulveristte 7 Premium Line) with two stainless steel bowls (45 ml) and stainless steel balls, figure 31. For each of the stainless steel bowls, 180 stainless steel balls, each 5 mm in diameter and 0.51 gr in weight), were used. Ball-to-powder ratio is taken as 1:10. 0.05-ml/powder ethanol (C_2H_5OH) is used as solvent. In order to prevent the powders to oxidize, the bowls were filled with spectroscopic quality Argon gas at a pressure of 2 bars. The powders were ground for a total of 20 hours at 250 rpm in 10 minute grinding cycles.

After each 10-minute cycle, the equipment is cooled by waiting 10 minutes in order to prevent overheating. After the completion of the overall grinding process, the bowls were left to cool down to room temperature. Then the bowls were opened and the powders were collected in the laboratory environment.
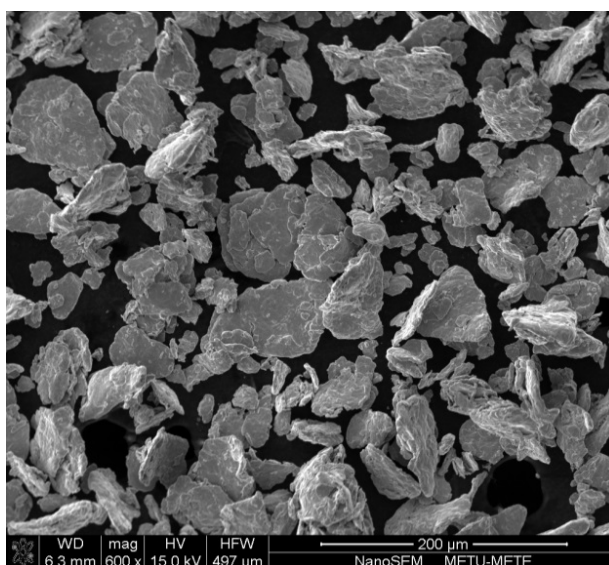
Figure 33 Scanning Electron Microscopy image of the initial iron powders.

3.5.2. Characterization

The grinding process has been interrupted after grinding for certain time periods, and sufficient amount of powder was taken out of the bowls for characterization processes before continuing grinding. The phase analysis of the ground powders was carried out using X-Ray diffraction. Diffractograms were obtained in a range of $2\Theta=20\text{-}100°$ with Cu-Kα radiation at a wavelength of 1.540562 Å using a Rigaku D/Max diffractometer. The particle size of the ground powders were calculated from diffraction peaks using the Scherer equation; where t is the crystallite size, λ is the x-ray wavelength, β is the line broadening at half the maximum intensity (FWHM) of the (110) peak, and Θ is the Bragg angle. Broadening of the diffraction peaks due to the instrument have been determined using the certified standard reference material (silicon) that came with the diffractometer. The microstructure and morphology studies were carried out using a FEI Nova Nano 430 FEG model scanning electron microscope (FEGSEM). The powders were attached to the aluminum sample holder using double-sided adhesive conductive carbon tapes. The magnetic properties of the

powders were examined using ADE Magnetics EV9 model vibrating sample magnetometer (VSM), which can operate with a magnetic field up to 3 Tesla.

$$t = \frac{0.9\lambda}{\beta\cos\theta}$$

Equation 12

3.6. Grinding Iron-Boron Powders

3.6.1. Experimental Method

3.6.1.1. Grinding Process by High Energy Ball Mill

The grinding process have been carried out using a Fritsch Pulveristte 7 Premium Line high energy ball mill with two 45 ml atmosphere-controlled stainless steel bowls and stainless steel balls. $Fe_{80}B_{20}$ and $Fe_{85}B_{15}$ powders, previously prepared by arc melting and pulverized, into the bowl number 1 and bowl number 2, respectively. Here, the aim is to produce nanoalloys from alloys readily prepared.

The Fe-B alloys have been prepared from pure components in their elemental forms by arc melting method. In this method, the sample is molten on a water-cooled copper plate under high-purity argon atmosphere by a non-consumable tungsten electrode. Raw materials were %99.97 pure iron and %99.25 pure boron. During melting process, Zr is used as the oxygen getter and for better homogeneity of the Fe-B alloy the sample has been turned upside down and re-molten 3 to 4 times. The sample prepared by arc melting was then molten and cast into a copper mold to produce 150 mm long cylindrical samples with 3 mm diameter by suction casting process. The cylindrical sample obtained was then cut into 4-5 mm thick slices using a Buehler Isomet Model 4000 Linear Precision Saw. These slices were then pulverized using jaw crushers.

For each of the stainless steel bowls, 180 stainless steel balls (each 5 mm in diameter and 0.51 grams in weight) have been used. The ball-to-powder ratio was selected as 1:13. Hence, in each bowl, initially there was 7.030 grams of powder. 6.208 ml Heptane (C_7H_{16}) has been used as the solvent. Oleic acid ($C_{18}H_{34}O_2$) and Oleylamine

($C_{18}H_{37}N$) are the surfactants used in the wet grinding process. The total amount surfactant in the bowl was 10% of the initial weight of powder and the surfactants were used in equal amounts. In order to prevent the powders from being oxidized, the bowls were filled with spectroscopic grade argon gas at a pressure of 1.2 bar. The powders were ground for a total of 30 hours at 400 rpm in 15-minute grinding cycles. After each 15-minute grinding cycle, the equipment was left to cool in order to prevent overheating of the equipment. In order to improve the efficiency of the grinding process, in each cycle the direction of rotation is reversed.

After the completion of each grinding cycle, the bowls were left to cool down to room temperature and they were then opened in lab conditions, a certain amount of colloidal solution was taken out using an injection syringe, and closed to continue the grinding process. The colloidal solution taken out is then subjected to centrifuge at 1000 rpm for 5 minutes in order for separation of the powders in the liquid. Then powder was washed with heptane three times and each time heptane added to powder then subjected to centrifuge at 5000 rpm for three minute then the powder were dried at 100 °C for 4 hour

3.6.1.2.   Characterization

The grinding process has been interrupted after certain time periods of grinding in order to sample sufficient amount of powder for characterization processes and then the grinding operation re-started. The phase analyses of the ground powders have been accomplished by X-ray diffraction. Diffraction curves were taken with Cu-Kα radiation at a wavelength of 1.540562 Å for 2Θ=20-100° using a Rigaku D/Max diffractometer and an older model Rigaku diffractometer. The microstructural and morphological examinations of the particles were done using a FEI Nova Nano 430 FEG model scanning electron microscope (FEGSEM). The powders were attached to the aluminum sample holder with a double-sided adhesive conductive carbon tape. The magnetic properties of the powders were examined using ADE Magnetics EV9 model vibrating sample magnetometer (VSM) operating at up to 3 Tesla magnetic field. In addition to this general procedure, in order to determine the equilibrium phases in solid-phase achieved by slow cooling rates, and to be able to compare the

solid-phase phase transformations, thermal analysis have been carried out using DSC (SETARAM).

CHAPTER 4

RESULTS AND DISCUSSIONS

4.1.   Grinding Pure Iron Powders

X-ray diffractograms for iron powders, before grinding and after grinding in ethanol for different time periods, are given in figure 34. As known, pure iron (α-Fe) has a body centered cubic (BCC) crystal structure. The diffraction lines (peaks) measured were indexed in the order of (110), (200), (211) and (220), according to the rule that says sum of the Miller indices of crystal planes in a BCC structure is always even (h+k+l=2n). When the diffractograms of the ground powders are compared with that of the unground Fe powder, up to 12 hours grinding, one observes no additional peaks that belongs to another material (oxide, impurity, etc.) and no shift of the existing peaks towards lower or higher Bragg angles. However, after grinding for 16 and 20 hours, low intensity peaks that belong to Fe_2O_3 (hematite) compound has been observed figure 35. The intensity of the Fe_2O_3 peaks significantly increases with increasing grinding times. Iron oxide formation is caused by the reaction between iron powders and the oxygen in the ambient when the bowels are opened after grinding operation.
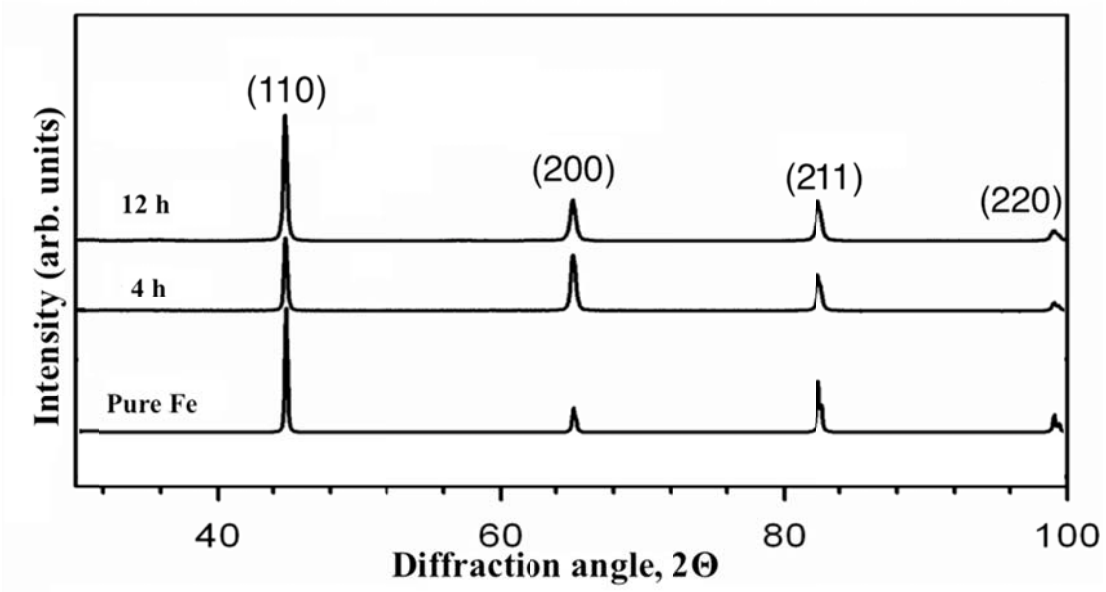
Figure 34 X-ray diffraction curves for pure iron powder and iron powder ground with ethanol for different time periods
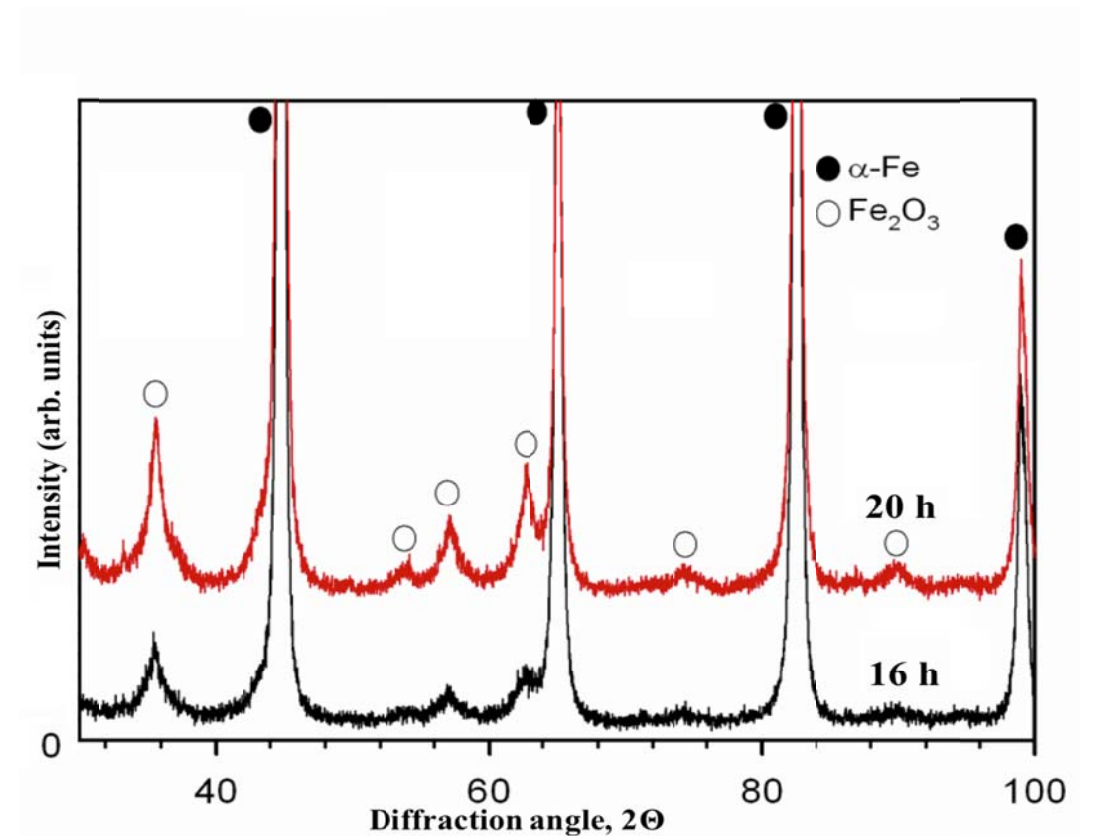
Figure 35 X-ray diffraction curves showing Fe_2O_3 formation in iron powders ground for 16 and 20 hours

Another result that came up with the X-ray diffraction analysis, the increase in the width of the diffraction peaks with longer grinding times. This shows that particle size is reduced with increasing grinding times. This is clearly shown in the detailed view of the (110) diffraction peak given in figure 36. The crystallite size calculated by the Scherer equation is 35 nm in unground Fe powders, and it is observed that the crystallite size is reduced down to 23 nm as the grinding time is increased Table 1.
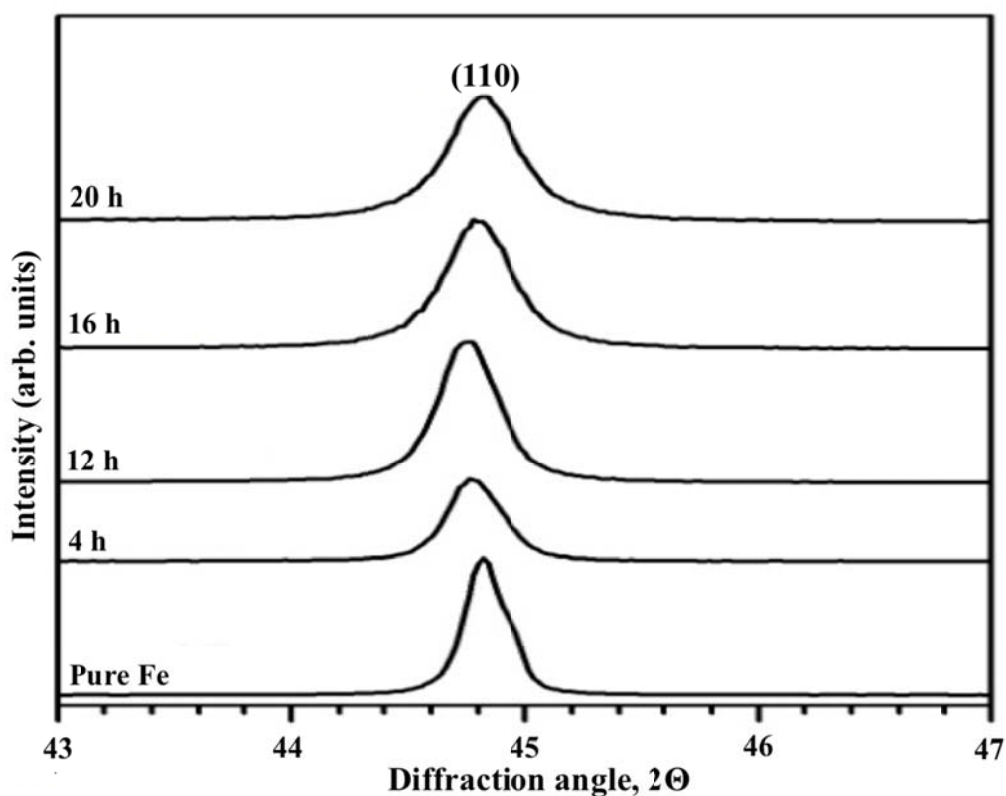
Figure 36 Detailed diffraction curves belonging to (110) peak which shows that line broadening increases with increasing grinding times for pure Fe powder and Fe powders ground with ethanol for different time periods

Table 1 The crystallite sizes, as calculated by the Scherer equation with respect to grinding times.

Grinding Time (h)	Crystalline Size (nm)
0	35.1
4	30.8
12	28.1
16	25.1
20	23.5

After grinding, in order to determine the particle morphology (spherical, cubic, stick, etc), size and distribution (whether there is any agglomeration), to have elemental analysis and to inspect phase formation and distribution in the microstructure and interfaces, scanning electron microscopy studies have been carried out and the microstructures obtained are given in figure 37. In microstructure analyses, significant decrease in the particle size with grinding time is observed, and even nano-sized particles were encountered in 20-hour ground powders.
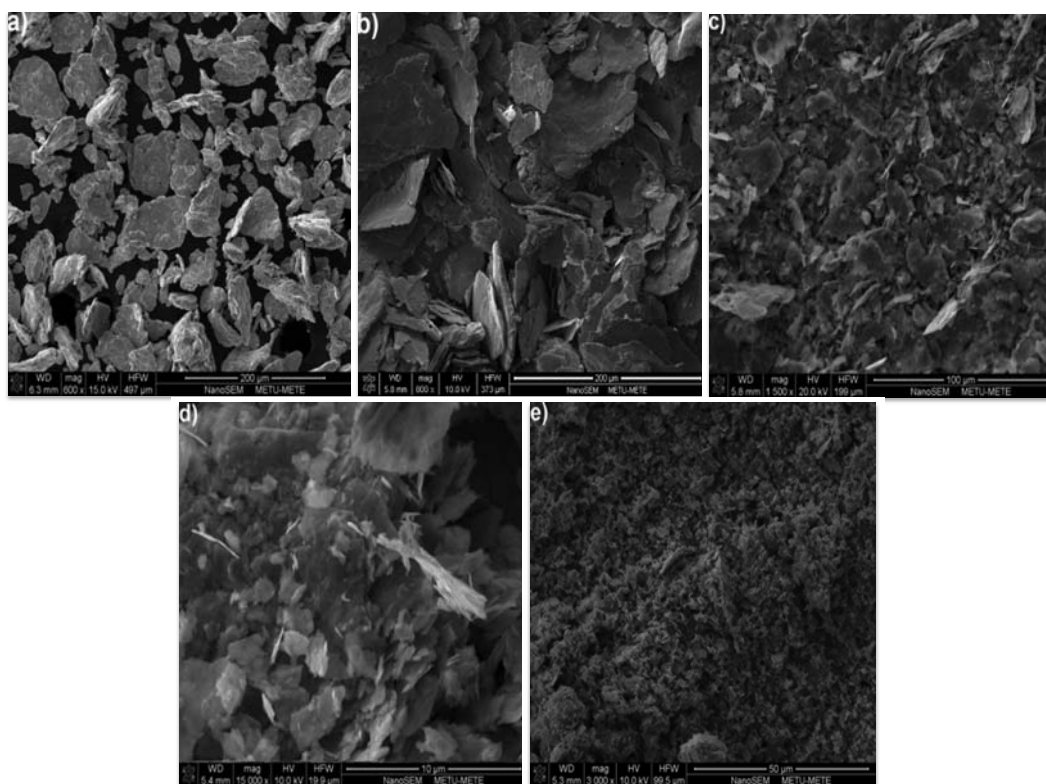
Figure 37 Electron micrographs of (a) pure Fe powder and Fe powders ground with ethanol for (b) 4 hours, (c) 12 hours, (d) 16 hours, (e) 20 hours

Elemental analyses have been carried out during electron microscopy studies in order to examine the chemical composition of the particles and to observe the oxidation that arose figure 38. Carbon peak due to the carbon tape is observed in all of the analyses. Moreover, 12-, 16- and 20-hr ground powder particles are observed to have oxide, even though not much. The amount Fe and O by weight calculated according to elemental analyses results are given in Table 2. Accordingly, the amount of oxygen in the structure is increased by increasing grinding times.
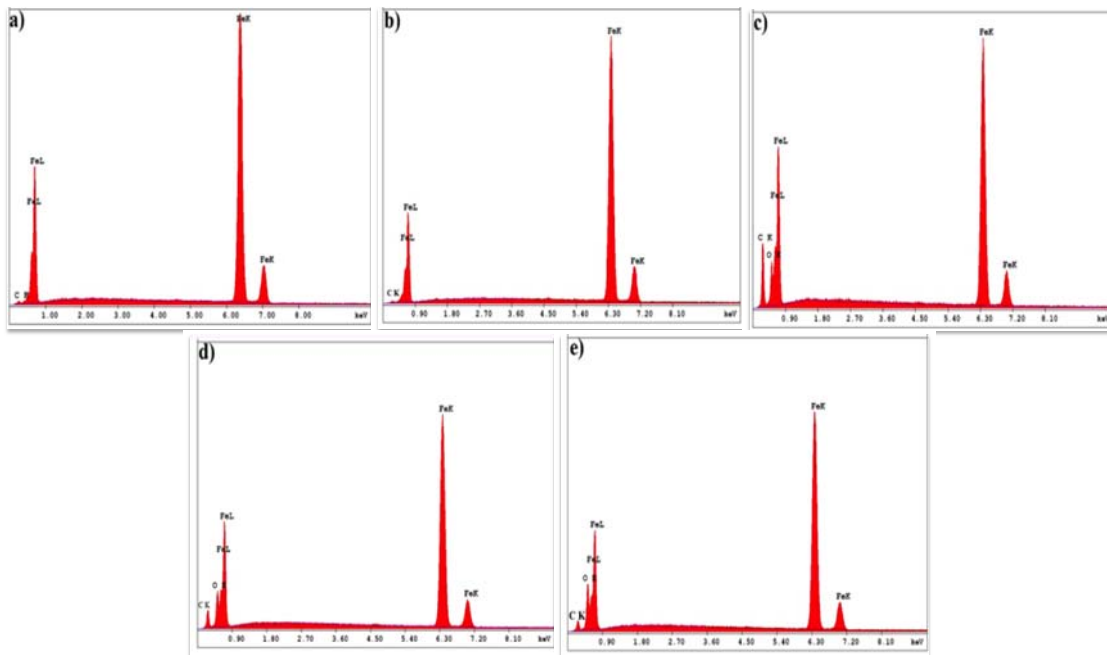
Figure 38 Elemental analysis curves for (a) pure Fe powder and Fe powders ground with ethanol for (b) 4 hours, (c) 12 hours, (d) 16 hours, (e) 20 hours.

Table 2 Elemental analysis results of pure Fe powder and Fe powders ground with ethanol for different time periods.

Grinding Time (h)	0	4	12	16	20
Fe (Weight percent)	97.97	97.57	92.89	91.47	90.54
O (Weight percent)	0	1.43	6.52	7.11	8.46
C (Weight percent)	2.03	1.00	0.55	1.42	1.00

The effect of grinding time on the magnetic properties of the particles has been examined through the hysteresis curves in figure 39 and magnetic parameters Table 3 calculated from these curves. All powders, unground and ground for different times, exhibit soft magnetic behavior with high saturation magnetization and high permeability. But, as the grinding time increases, the oxide formation, which is shown by phase analysis and microstructural research, caused the saturation magnetization to decrease and remanent magnetization and coercivity to increase.
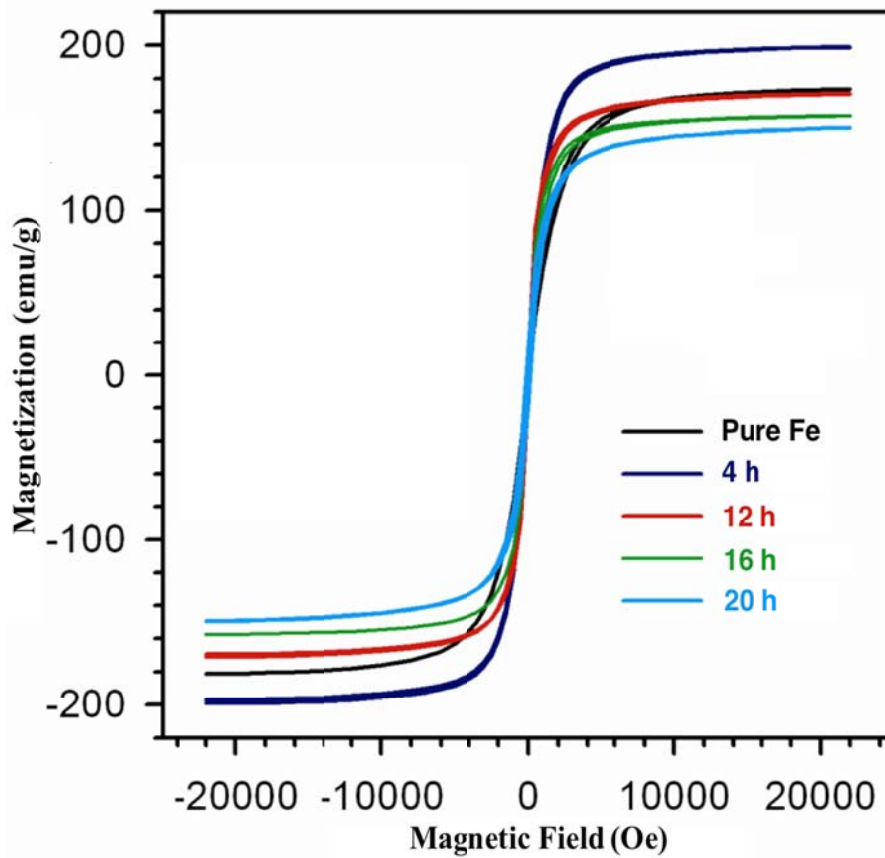
Figure 39 Hysteresis curves belonging to pure Fe powder and Fe powders ground with ethanol for different time periods

Table 3 Values of magnetic parameters of pure Fe powder and Fe powders ground with ethanol for different time periods.

Grinding Time (h)	Saturation Man., M_s (emu/gram)	Man., M_r (emu/gram)	Squareness, S (M_r/M_s)	Coercivity H_c (Oe)
0	177.40	0.05	0.00	0.60
4	199.18	2.78	0.01	18.83
12	170.85	9.60	0.06	54.97
16	157.36	10.78	0.07	88.77
20	150.08	17.13	0.11	134.21

Materials having soft magnetic properties can easily be magnetized and demagnetized. Furthermore, this type of materials has a single-phase microstructure with no impurities of defects, which in turn, makes it easier for the magnetic domains

85

to move during magnetization and demagnetization. The oxide that forms after grinding operation makes it difficult for the magnetic domains to move. The increase of magnetization and Coercivity with increasing grinding times figure 40 is caused by the slowing down of magnetization and demagnetization by increasing amount of oxides.
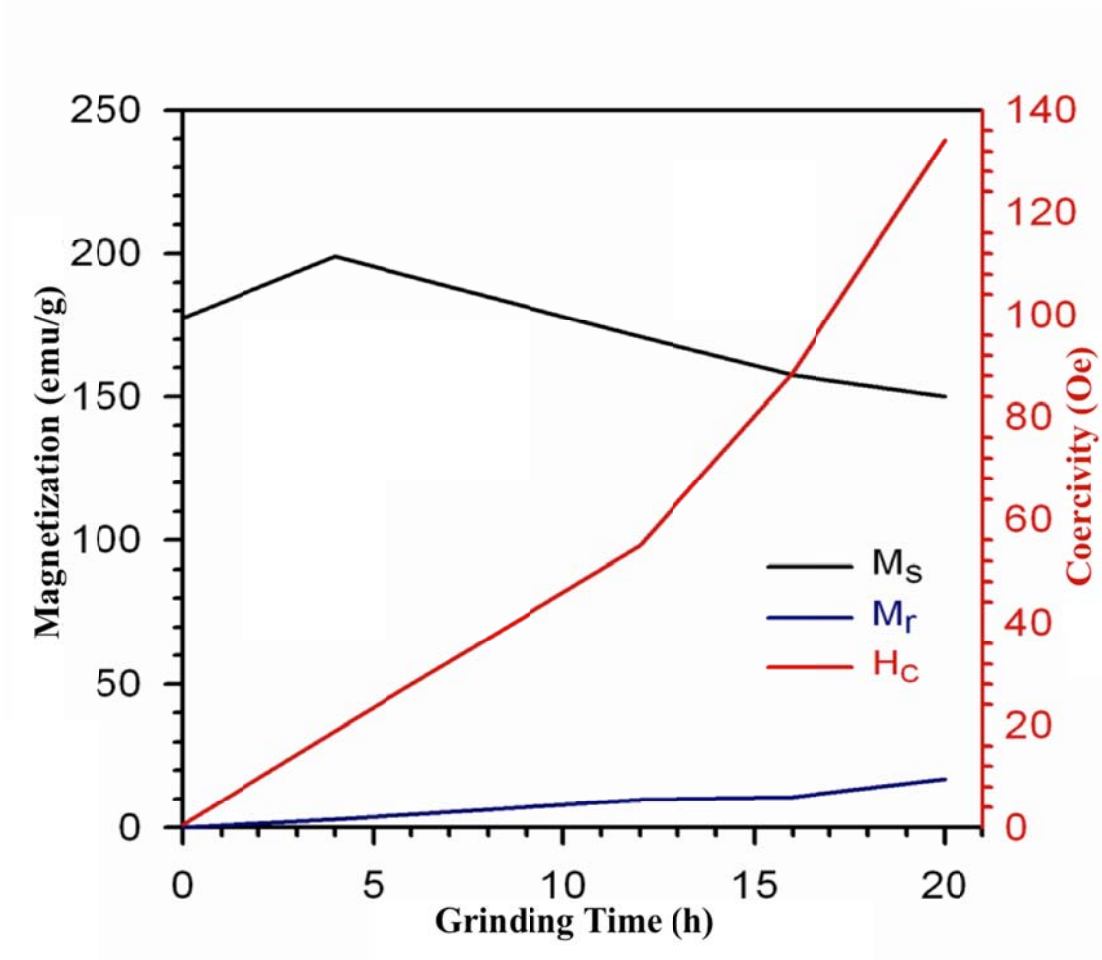
Figure 40 The change of saturation magnetization, remanent magnetization and Coercivity with grinding times for pure Fe powder and Fe powders ground with ethanol for different time periods.

4.2. Grinding Iron-Boron Powders

Figure 41 are the x-ray diffraction curves of $Fe_{80}B_{20}$ and $Fe_{85}B_{15}$ powder samples, which were taken out of the grinding bowls at certain intervals during grinding up to 30 hours using a ball mill, following production by arc melting and pulverization by jaw crushers. According to the Fe-B phase diagram, figure 42, $Fe_{80}B_{20}$ alloy consists of a pure iron phase, which is known as the α-Fe with BCC structure at room temperature transforming to an FCC structure at a temperature of 912°C, and an Fe_2B intermetallic eutectic structure. Fe_2B intermetallic phase has a space group of I41/amd and a tetragonal structure with cell parameters a=b=5.105, c=4.251. (Kapfenberger C., 2006, R. Bellissent, 1995). When the x-ray diffraction results are examined, unstable phases forms after one hour of grinding; however, they disappeared after longer grinding times. After longer grinding times, Fe_2B peaks start to disappear and after 60 hours of grinding α-Fe peaks remain as the dominant ones. This shows that, during grinding, both alloys become amorphous and glassy phases form. It is estimated to be composite structure with α-Fe crystals and amorphous phases. Thermal analyses were carried out in order to confirm the formation of glassy phases, Furthermore, grinding was continued up to 60 hours in order to see whether the system will go through complete amorphisation or not.
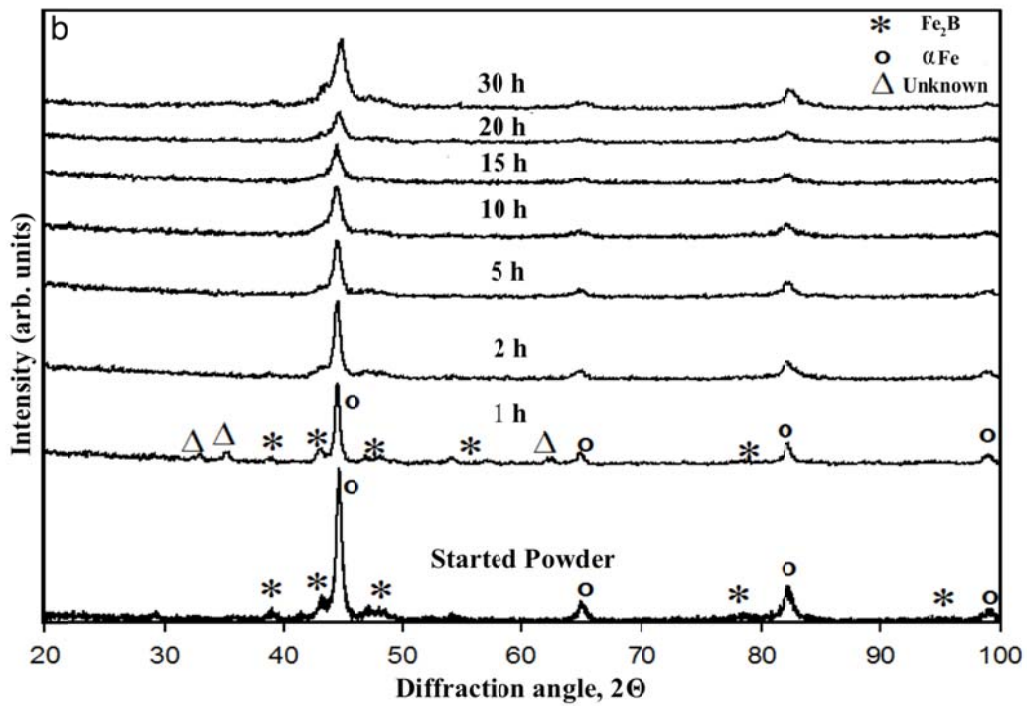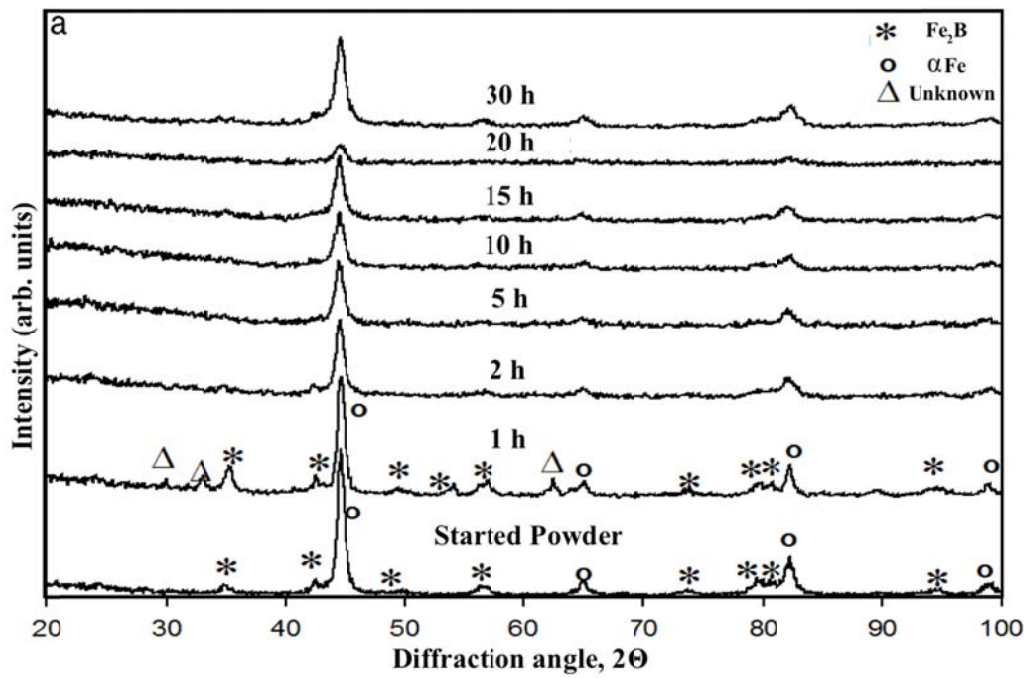
Figure 41 X-ray diffraction curves of (a) $Fe_{80}B_{20}$ and (b) $Fe_{85}B_{15}$ powders, which were produced using arc-melting method, pulverized in an agate mortar, and ground for 1, 2, 5, 10, 15, 20,30 and 60 hours in a ball mill.
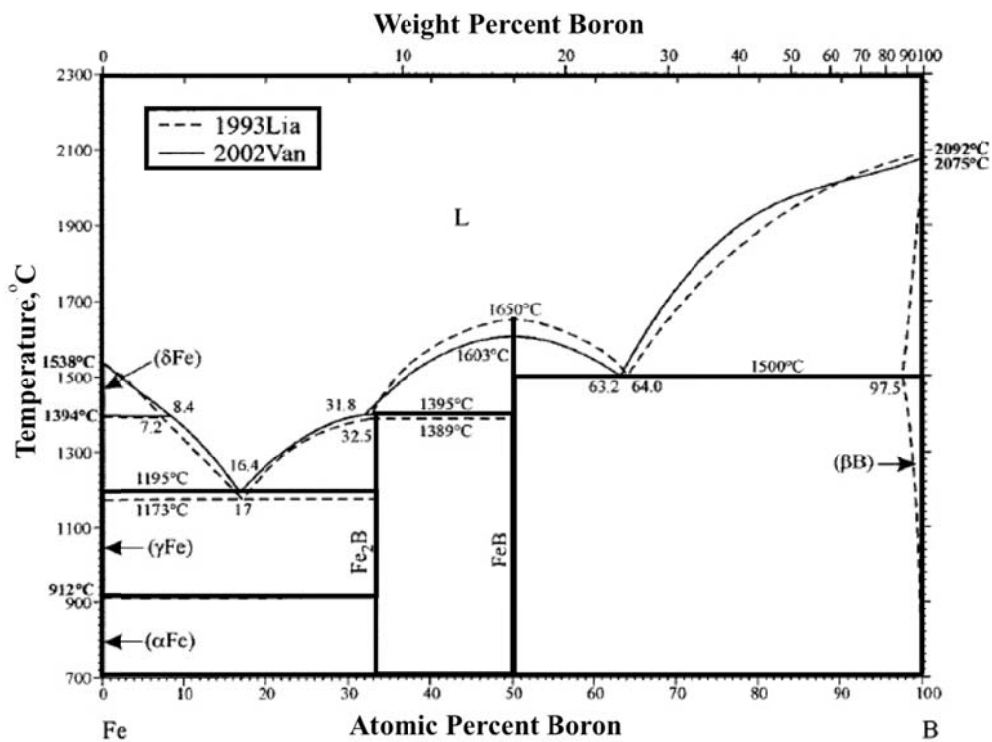
Figure 42 Fe-B binary phase diagram (Ishida, 1990)
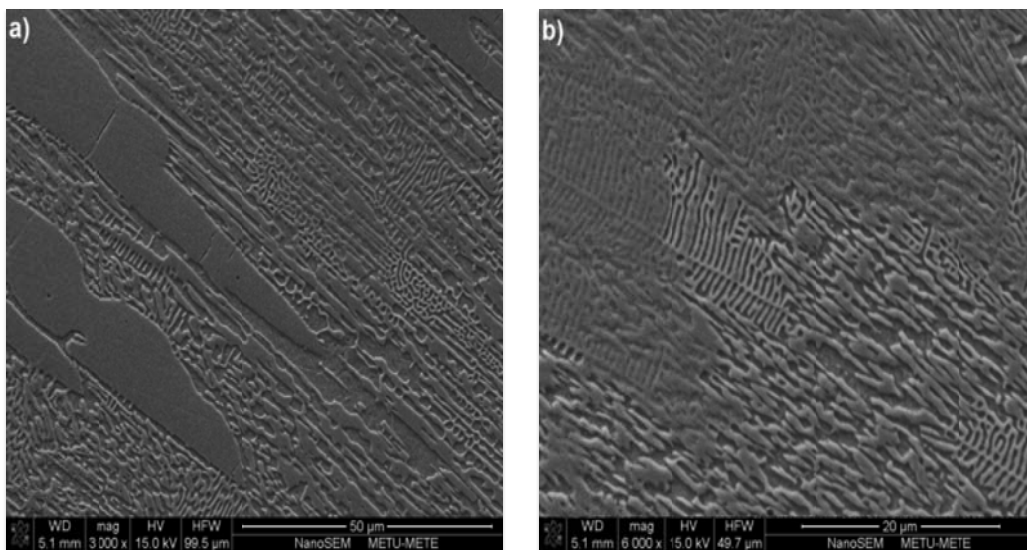
Figure 43 SEM micrographs of (a) $Fe_{80}B_{20}$ and (b) $Fe_{85}B_{15}$ alloys cast by arc melting. $Fe_{80}B_{20}$ alloy has both pro-eutectic Fe_2B intermetallic and eutectic phases; on the other hand, $Fe_{85}B_{15}$ has only eutectic structure.

Furthermore, in order to examine the solid-phase transformations and the different phases forming as a result of differences between cooling rates, the microstructures after arc melting have been studied figure 43 and x-ray analyes figure 44 have been carried out. The results of the structural investigations show that the structure obtained by equilibrium solidification and cooling has predominantly α-Fe and Fe_2B structure. This is in accord with the binary Fe-B equilibrium phase diagram (Ishida, 1990) figure 42. However, in the alloy which has been produced at high cooling rates by suction casting into a copper mold, in addition to α-Fe and Fe_2B equilibrium phases, non-equilibrium phase Fe_3B formed as can be seen from the X-ray results figure 44a. As can be seen in the X-ray results, in the powders that are subjected to ball milling, proportion of the phases forming as a result of solidification decreases in time figure 44. Furthermore, these x-ray results show that the Fe_2B and Fe_3B intermetallic phases formed initially has a tendency to disappear even after only one hour of ball milling, which in turn, results with stabilization of α-Fe nanoparticles with progressing ball milling times., in addition to the higher stability of α-Fe nanoparticles, with longer milling times (for example, 60 hours) lead to possible amorphous phase formation. The existence of amorphous phase is shown by the wide peak at low Bragg angles in X-ray analyses figure 44b and isochronal DSC thermograph figure 45.

In this thermograph, endothermic heat exchange belonging to the characteristic glass transition phenomenon and following exothermic heat release events due to crystallization from the amorphous phase are observed. Besides, in the DSC thermograph, the two endothermic heat exchange events observed at ~725 °C and ~900 °C, corresponds to Curie point (magnetic order) and $\alpha \rightarrow \gamma$ phase transition point. This can be taken as evidence to the formation and equilibration of α-Fe nanoparticles.
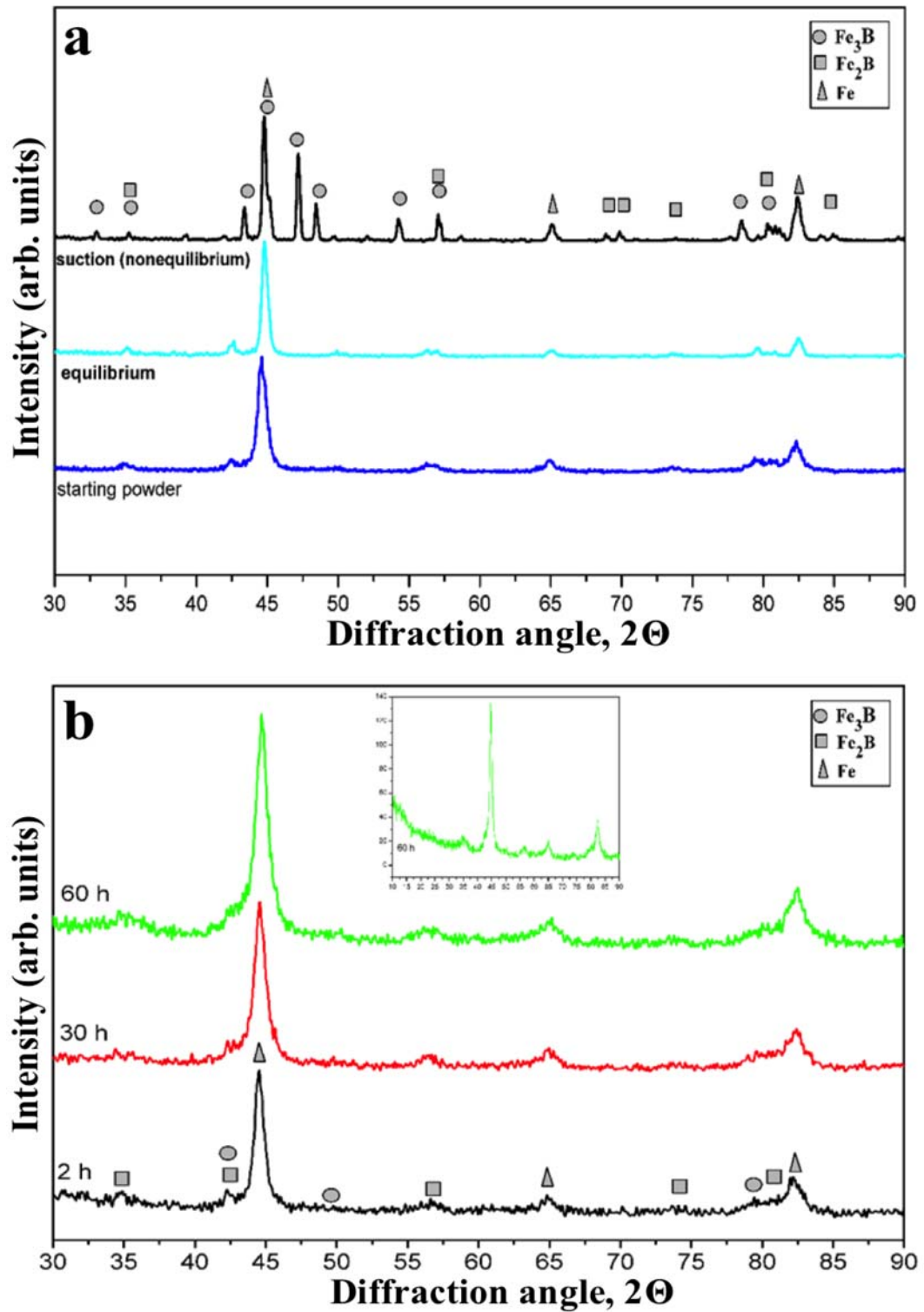
Figure 44 XRD results of initial powders (0 hour), the alloy produced by equilibrium cooling, and the alloy produced by suction casting method. b) XRD results of powders ground for 2 hours, 30 hours and 60 hours.

At the end of the experimental studies on these two Fe-B alloys, it is seen that α-Fe nanocrystals of high-energy ball milling operation are embedded in nanoparticles in an amorphous matrix.
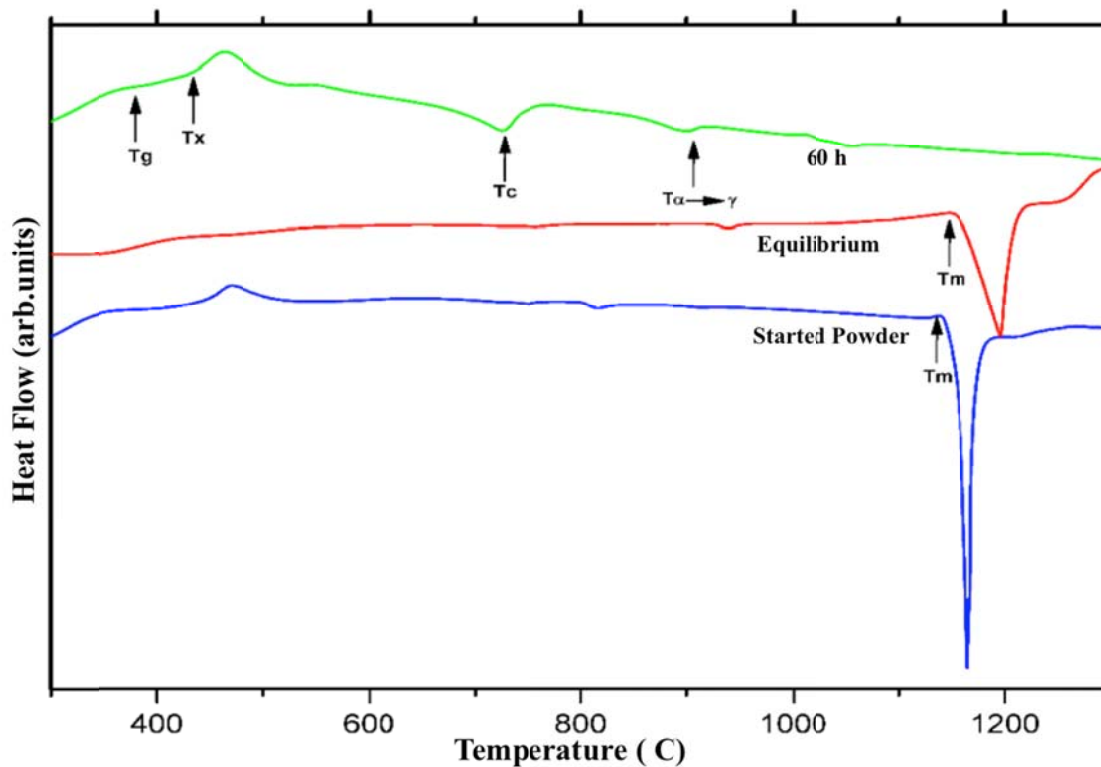
Figure 45 DSC analyses of the initial $Fe_{80}B_{20}$ powders, the alloy produced by equilibrium cooling and powders ground for 60 hours.

Scanning electron microscopy studies have been carried out in order to determine the morphology (spherical, cubic, stick, etc), size and distribution (if there is any agglomeration) of the particles after grinding, do their elemental analysis and inspect any phase formation and distribution in the microstructure and interfaces. The microstructures obtained are given in figure 46. Together with electron microscopy studies, elemental analyses figure 47 have been done to investigate the chemical

composition of the particles. However, the radiation of boron atom cannot be obtained in the EDX analysis (Energy Dispersive Analysis). This is because the characteristic radiation of B atom is too low. That's why the Fe-B atomic distributions are not studies using this method. A carbon peak due to the carbon tape, Al and Si peaks (about 2%) from the agate mortar and Cr and Mn impurity peaks (about 1%), which is considered to be from the stainless steel bowl and balls, are observed in all of the analyses. According to microstructure analyses, with increasing grinding times there is an observed decrease in particle sizes and starting after 5 hours of grinding, nano-sized particles have been observed in the powders. Furthermore, as the grinding time is increased, the proportion of these nano-sized particles increases significantly. In figure 48, SEM analyses of nanoparticles obtained at 0, 5, 30 and 60th hours. As can be seen in these photographs, particle size ranges between 35 and 150 nanometers. However, as these particles show magnetic behavior, the definition of photographs was a not high, higher magnification were not possible, and it is not certain whether there are particles smaller than 35 nanometers.
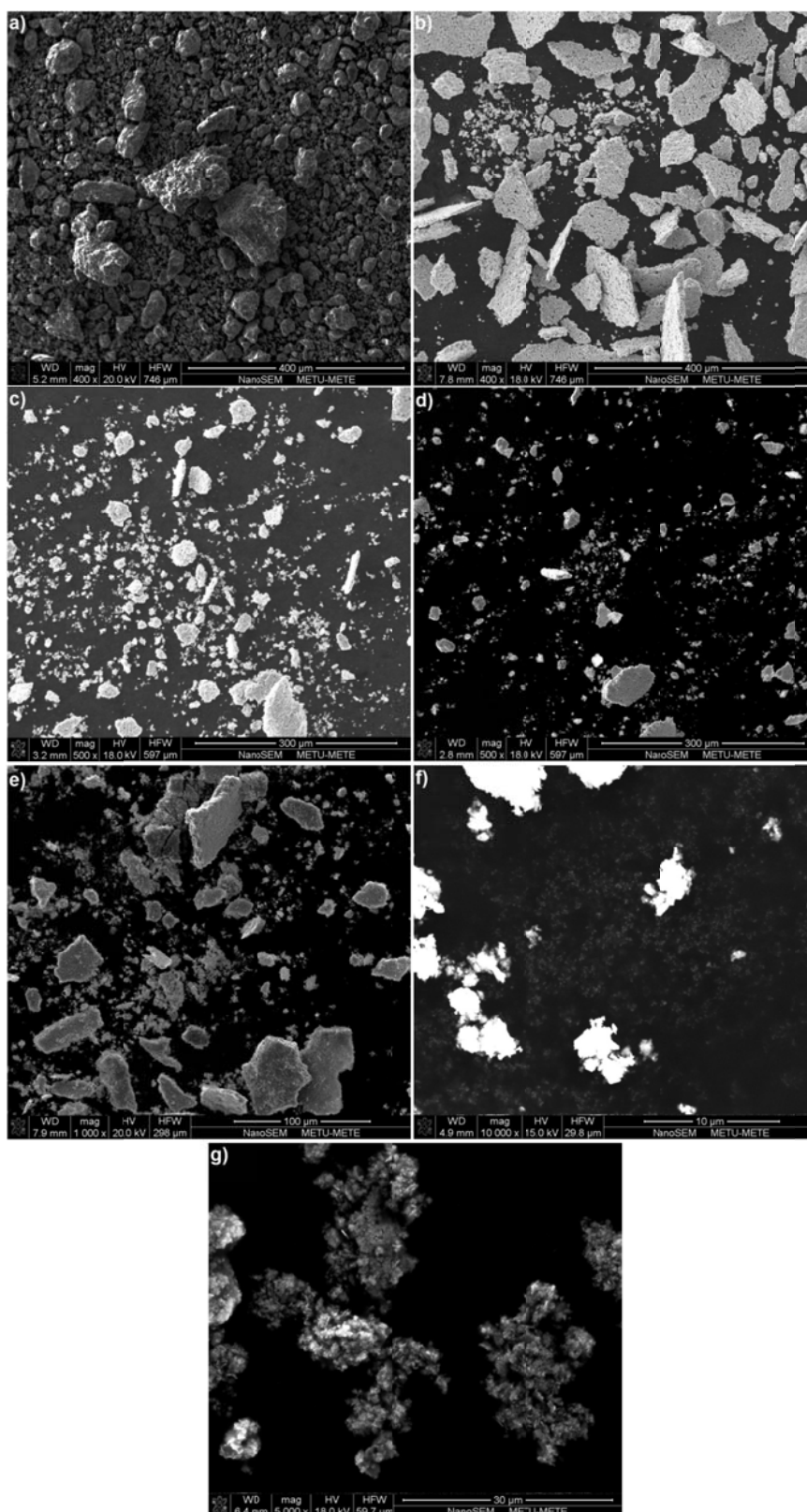
Figure 46 SEM micrographs of $Fe_{80}B_{20}$ powders (a) pulverized in jaw crasher and ground in ball mill for (b) 1 hr, (c) 2 hr, (d) 10 hr, (e) 15 hr, (f) 20 hr and (g) 30 h**r.**
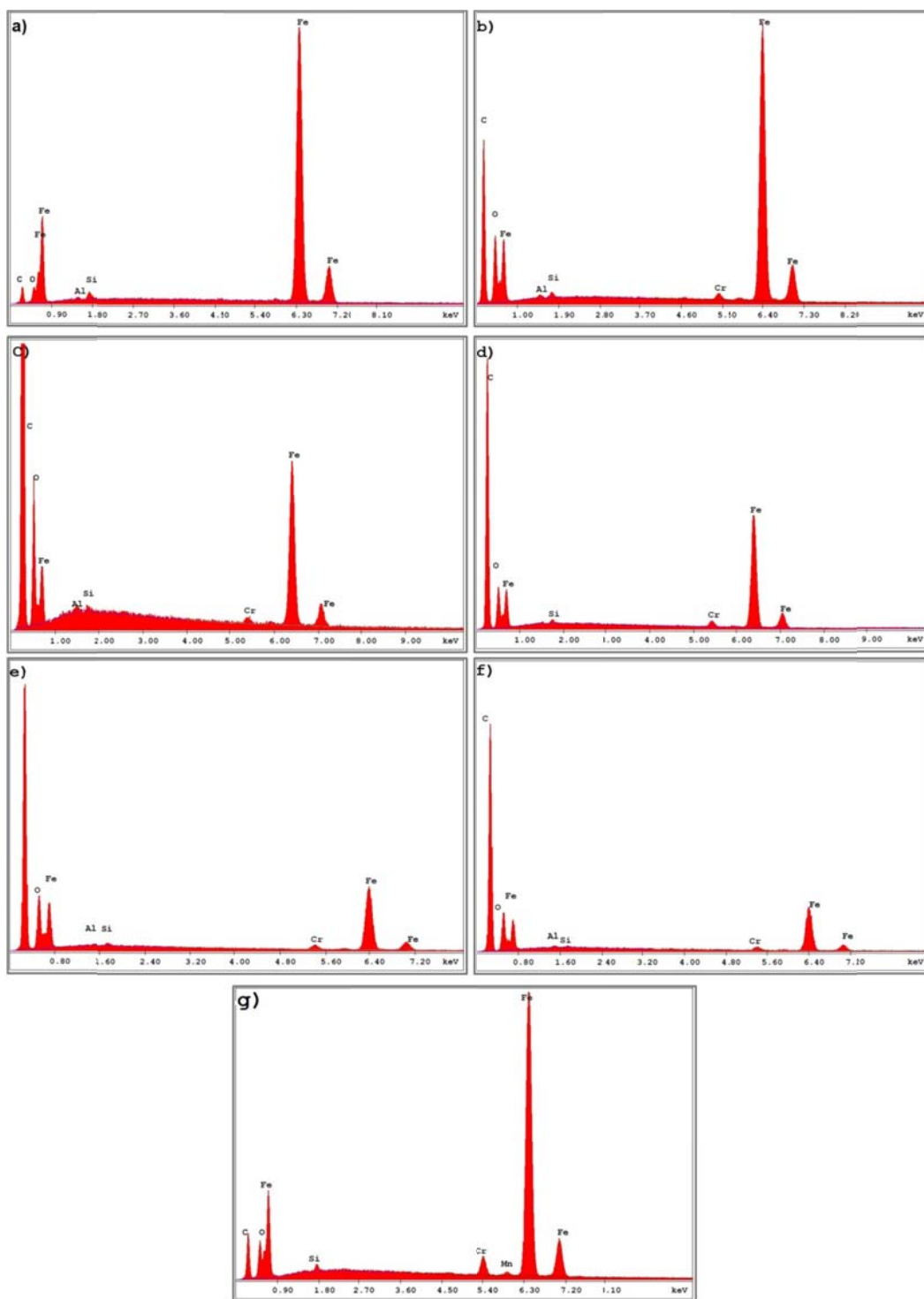
Figure 47 Elemental analysis curves for (a) initial $Fe_{80}B_2O$ powder, and $Fe_{80}B_{20}$ powders ground for (b) 1 hr (c) 5hr (d) 10 hr (e) 20 hr (g) 30 hr, (g) 60 hr.

95
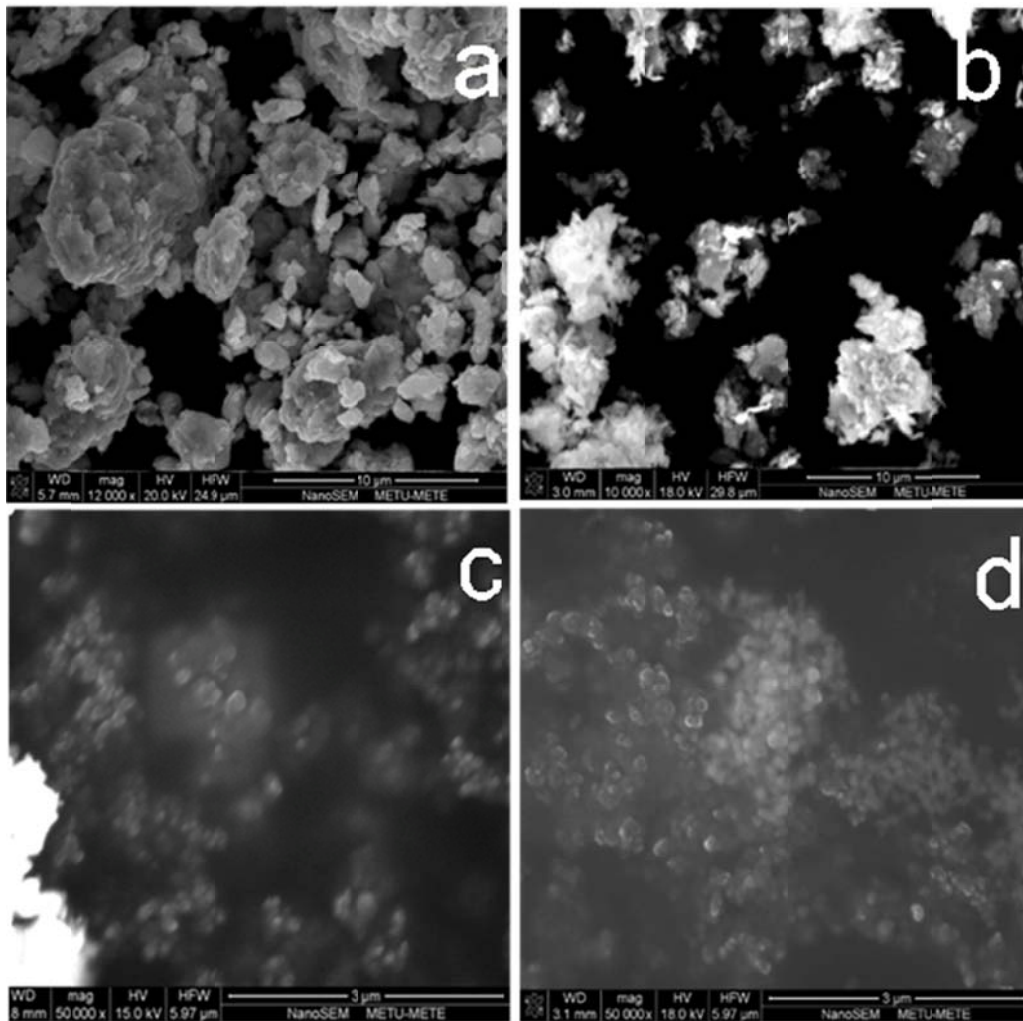
Figure 48 High magnification SEM micrographs of $Fe_{80}B_{20}$ powders ground for **(**a) 0 hr, (b) 5 hr, (c) 30 hr and d) 60 hr.

The effect of grinding time on the magnetic properties of the particles has been studied through the hysteresis curves in figure 50 and magnetic parameters Table 4 calculated from these curves. Powders ground for different time periods, all exhibit soft magnetic behavior with high saturation magnetization and high permeability. With increasing grinding times, saturation magnetization increased in the first hour of grinding; however, it decreased with further grinding. The reason the powders behave this way is related with their microstructure. The initial powders have spherical morphology and are sized in a range between 5 and 200 μm. However, as understood, after 1 hour of grinding, the powders gets finer and, by agglomeration,

they form plates around 10-20 μm thick and 50-300 μm large. When these plates are further inspected, it is observed that the plates are actually formed by agglomerates sized between 5 and 20 μm figure 49. The decrease in the remanent magnetization, Coercivity and squareness at the end of one hour grinding is thought to arise from the same reason. With longer grinding times, saturation magnetization is decreased, and remanent magnetization, Coercivity and squareness is increased. Again, as can be understood from the electron microscopy images, particle size gets smaller and proportion of nano-size particles gets higher. Furthermore, as it is seen in the x-ray results, as grinding times increases, amorphous phases form and it is believed to have composite structures by Fe-B amorphous structures and Fe crystals. The increasing slope of magnetization curves with increasing grinding times is based on this (Ishida, 1990). As known, as there are no magnetic domains in glassy magnetic materials, the "barrier" against magnetization changes is very low. The changes in magnetization at long grinding times are based on these reasons.
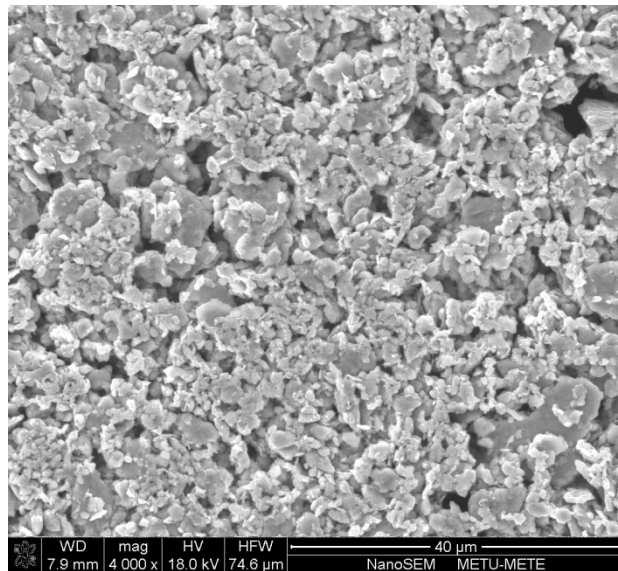
Figure 49 Close-up images of the plate structures formed by $Fe_{80}B_{20}$ powders ground for 1 hour.
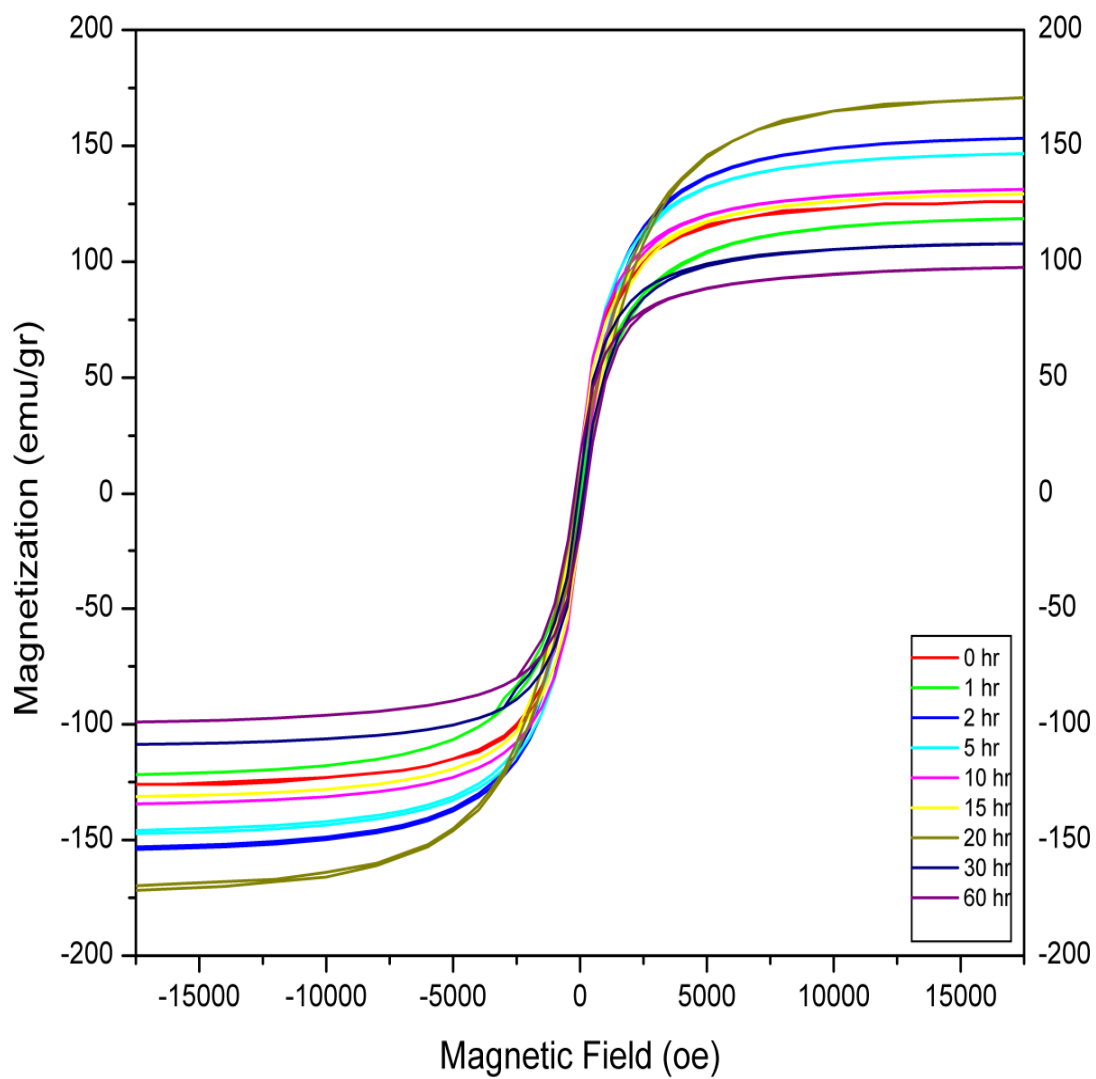
Figure 50 Hysteresis curves for initial powders (cast and pulverized in jaw crashers) and $Fe_{80}B_{20}$ powders ground for different times

Table 4 Magnetic properties of initial powders (cast and pulverized in jaw crashers) and $Fe_{80}B_{20}$ powders ground for different times.

Grinding Time (h)	Saturation Man., M_s (emu/gram)	Remanent Man., M_r (emu/gram)	Squareness, S (M_r/M_s)	Coercivity H_c (Oe)
Started Powder	171.33	7.81	0.046	121.34
1	199.07	2.33	0.019	35.34
2	153.86	13.97	0.091	145.21
5	147.07	14,38	0.097	145.21
10	147.86	16.09	0.121	156.24
15	129.74	15,75	0.121	173.33
20	172,40	3.87	0.031	38.68
30	108	7.39	0.068	174.42
60	98.4	16.5	0.168	214.043

The microstructural images of $Fe_{85}B_{15}$ powders ground in the second grinding bowl are given in figures 51 and 53. There is a significant decrease in particle size with increasing grinding time. Particularly after 5 hours of grinding, sub-micron and nano-sized particles are observed to form. Particle size ranges between 40 and 200 nm. It is not certain whether there are particles smaller than 40 nanometers. Carbon peak due to the carbon tape, oxygen peak thought to be due to oxides forming on the surface during drying, Al and Si peaks (about 2%) considered to be from the jaw crasher and finally Cr peaks considered to be from the stainless steel bowl and balls are observed in the elemental analyses curves given on figure 52. The impurity levels in the samples do not exceed 3%. The B concentration in the samples couldn't be determined for the reasons explained earlier.
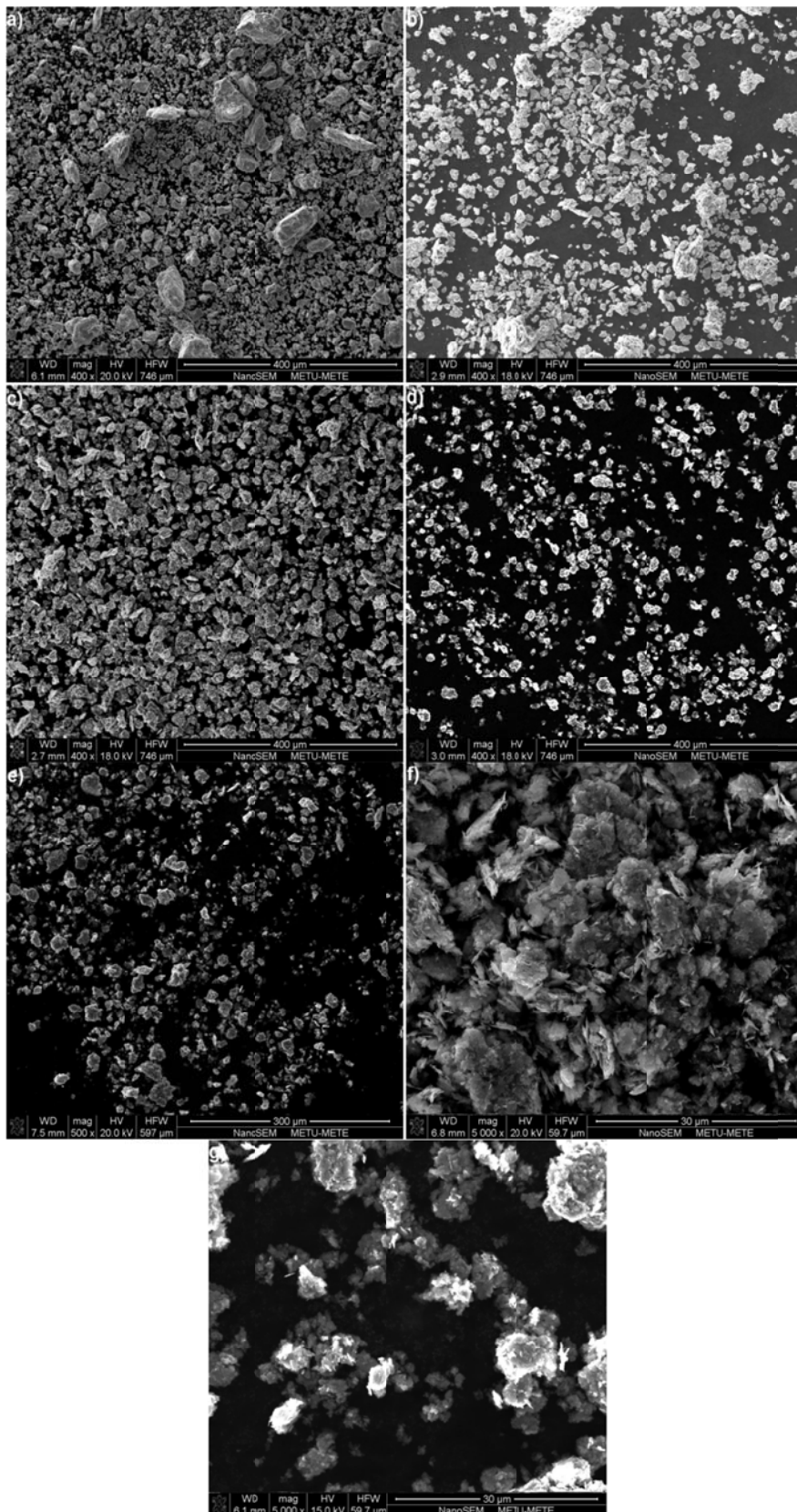
Figure 51 Electron micrographs of $Fe_{85}B_{15}$ powders (a) pulverized in jaw crasher and ground for (b) 1 hr, (c) 5 hr, (d) 10 hr, (e) 20 hr, (f) 30 hr and (g) 60 hr in ball mill.
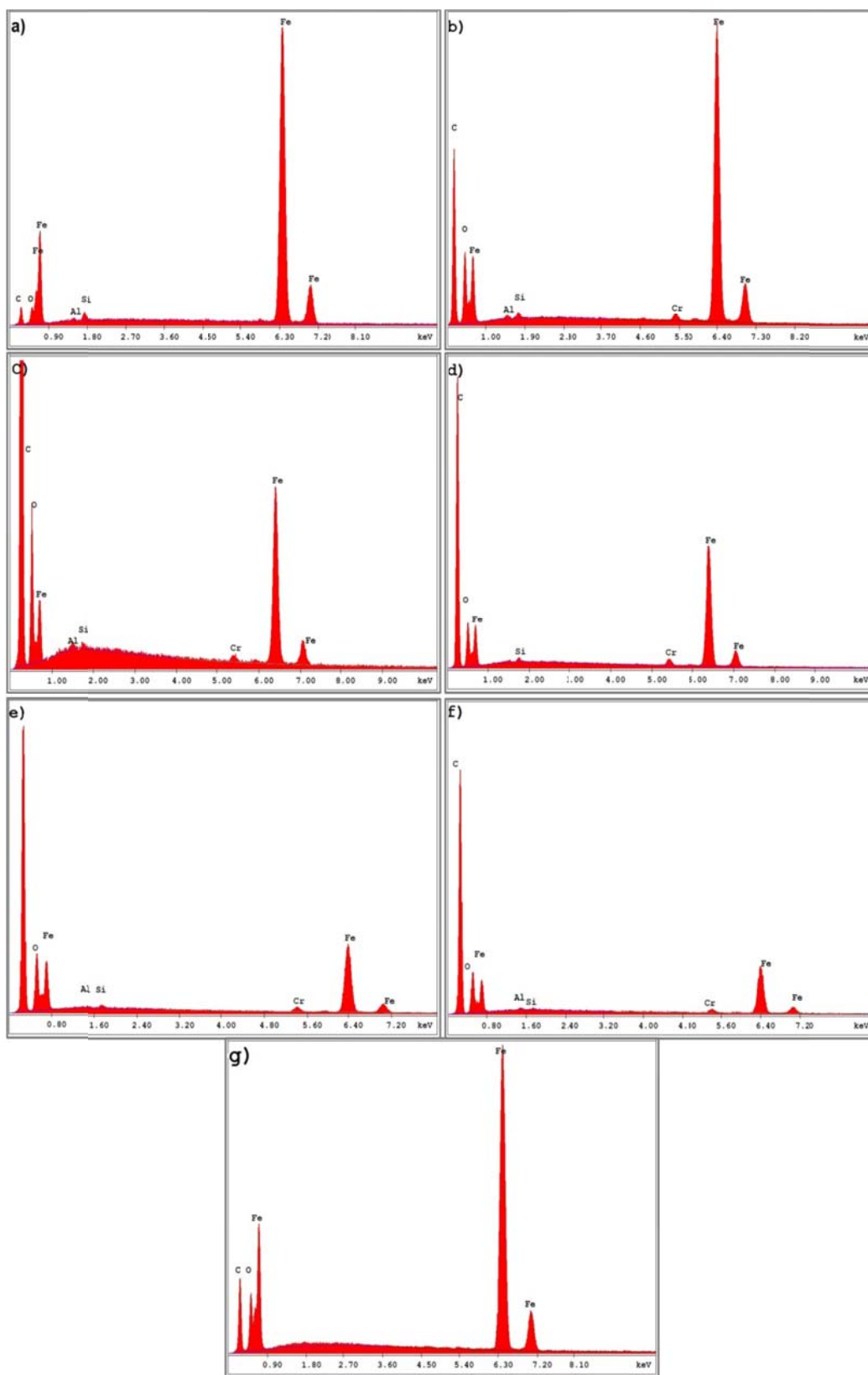
**Figure 52** Elemental analysis curves for $Fe_{85}B_{15}$ powders: (a) initial powder and powders ground for (b) 1 hr, (c) 5 hr, (d) 10 hr, (e) 20 hr, (f) 30 hr and (g) 60 hr
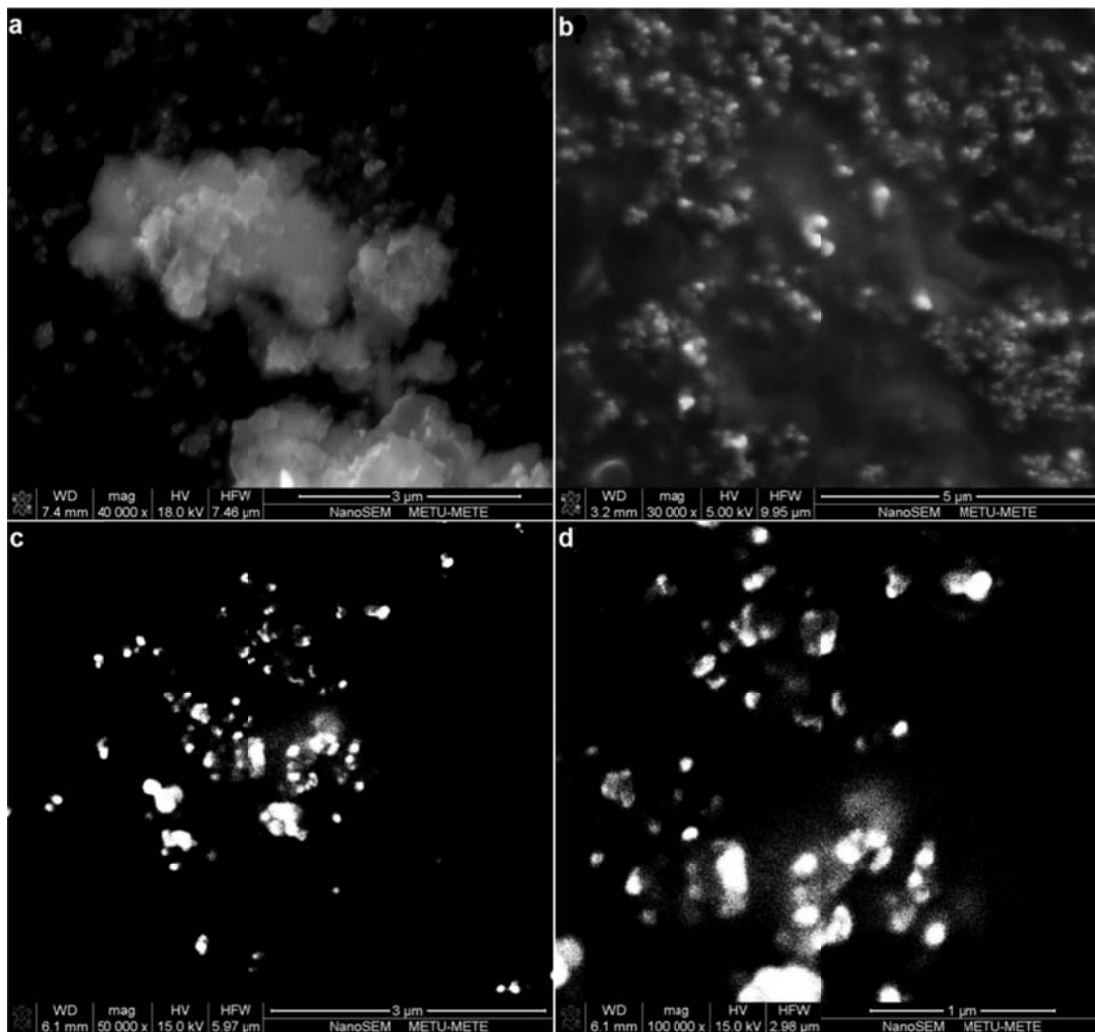
Figure 53 High-magnification SEM micrographs of $Fe_{85}B_{15}$ powders ground for (a) 5 hr, (b) 10 hr, (c) 30 hr, and (d) 60 hr.

The hysteresis curves for $Fe_{85}B_{15}$ powders are given in figure 54. As with $Fe_{80}B_{20}$ powders, the $Fe_{85}B_{15}$ powders too exhibit a soft magnet behavior with a high saturation magnetization and high permeability. Compared to $Fe_{80}B_{20}$ alloy, this alloy has a higher saturation magnetization. Compared to initial alloy, after one hour of grinding, significant decrease is observed in magnetic properties such as in saturation magnetization, remanent magnetization, Coercivity and squareness. This is though to be based on the Fe_2B phase clearly seen in x-ray analysis. The amount of this phase decreases with longer grinding times and disappears after the 5th hour. Furthermore, because of the x-ray results and the increasing slope in the

102

magnetization curve, amorphous phases are considered to form at the end of 2nd hour. The increase in the amount of this glass phase, the disappearance of the unstable phases in time, and nanoparticles starting forming after 5th hour are considered as the reasons why the magnetic parameters mentioned decreases after 5th hour.
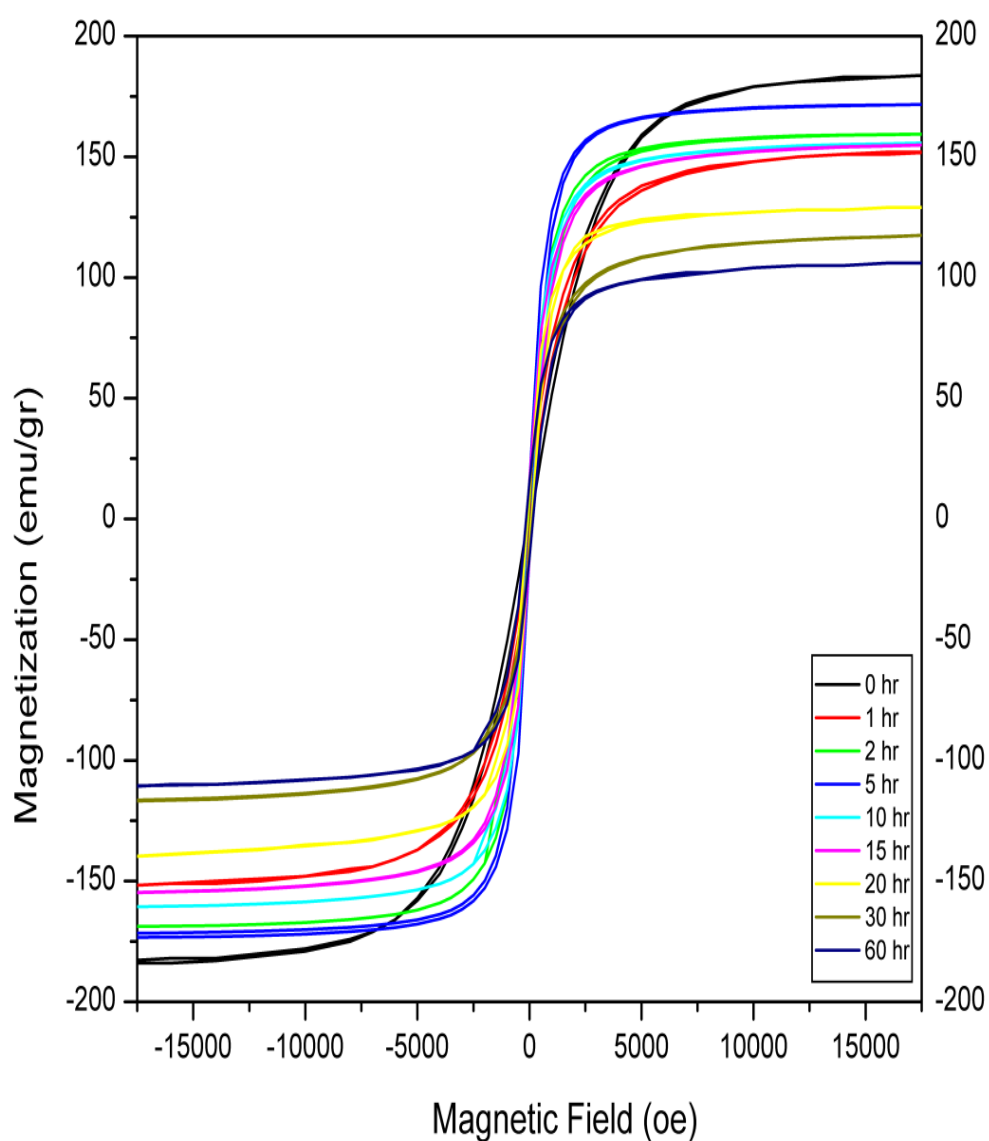
Figure 54 Hysteresis curves for the initial powders pulverized by jaw crashers after being cast, and $Fe_{85}B_{15}$ powders ground for different time periods

Table 5 Magnetic properties for the initial powders pulverized by jaw crashers after being cast, and $Fe_{85}B_{15}$ powders ground for different time periods

Grinding Time (h)	Saturation Man., M_s (emu/gram)	Remanent Man., M_r (emu/gram)	Squareness, S (M_r/M_s)	Coercivity H_c (Oe)
Started Powder	184.10	4.26	0.023	73.64
1	151.83	2.25	0.015	27.33
2	168.83	2.55	0.055	68.57
5	172.52	15.74	0.091	83.37
10	158.22	14.87	0.094	96.36
15	154.94	16.57	0.107	122.33
20	134.49	10.61	0.079	87.30
30	117	13.9	0.118	140.42

CHAPTER 5

CONCLUSION

In the Fe-B systems, amorphous structure was observed to maintain and considerably interesting results were obtained. For this system, the changes of surface energy with temperature are in agreement with the results of the Voronoi analyses.

B atoms in 2 nm $Fe_{85}B_{15}$ particles were observed to fled the surface and move towards the center at high temperatures. 2 nm particles exhibit a faceted structure while larger particles maintain their spherical structure at all temperatures.

As mentioned earlier, structural analyses (Voronoi analyses, radial distribution functions, surface energies and phase separations) have been done for the nanoparticles of $Fe_{85}B_{15}$ systems. As a result amorphous structure was maintained and considerably interesting results have been achieved. The atomic distributions in the particles exhibit a variation depending on temperature. In $Fe_{85}B_{15}$ particles, as the temperature is raised, B atoms move towards the inner parts and it is observed to have no B atoms left on the surface at above 1500 K leading to a core-shell structure. In $Fe_{85}B_{15}$ alloys, particles exhibit B-rich regions and Fe-rich regions at low temperatures, where Fe-rich regions have comparatively ordered arrangements and B-rich regions have a disordered structure.

In the experimental part of the study initially the focus was on determination of process parameters such as grinding times, type and amounts of solvents and the speed of rotation, and the effect of these parameters on particle size and shape and

magnetic properties. For this Fe powders were ground and the related parameters have been determined.

Two different compositions have been alloyed using arc melting and ground in separate grinding bowls. In the bowl, powders previously alloyed by arc melting and pulverized by crasher. After grinding for 1, 2, 5, 10, 15, 20, 30 and 60 hours, samples have been taken from the grinding bowls and magnetic measurements, X-ray analyses and SEM studies have been carried out.

As the grinding time increases, SEM analyses showed that number of sub-micron particles increased in all mixtures ground. In the analyses carried out, the size of the sub-micron particles have been observed to range between 35 and 100 nm. However, due to the magnetic nature of the particles, level of magnification or clarity desired was not achieved in SEM images. Hence, TEM studies are required for more detailed studies. Evaluations and preliminary studies carried out show that TEM study is also considerably difficult due to the magnetic behavior of the samples. Furthermore, nano-sized particles are observed not to get even smaller after they are formed, and to a great extent, they maintain their initial size. The reason for this is assumed to be the surfactants used. Therefore, it is agreed upon that better results could be achieved in the following studies by initially dry grinding for a certain period of time (not adding any surfactants), and later adding surfactants and continuing with wet grinding.

Furthermore, X-ray analyses show that amorphous-crystalline composite structures are formed in Fe-B system. It is observed that B-rich glassy alloys are formed together with Fe-rich crystalline structures in the system. This is in agreement with the simulation results. Simulations showed that B-rich regions prefer amorphous structures, while Fe-rich regions have a tendency towards crystalline structures. Simulations also showed that nanoparticles exhibited phase separation with Fe-rich crystalline regions and B-rich amorphous regions.

REFERENCES

AGUADO, A. & LÓPEZ, J. M. 2005. Molecular dynamics simulations of the meltinglike transition in Li_{13}Na_{42} and Na_{13}Cs_{42} clusters. *Physical Review B,* 71**,** 075415.

AKDENIZ, M. V., MEKHRABOV, A. O., YALÇIN, M., AYKOL, M. & YILDIRIM, M. *Tubitak 110M373 Final report.* 2013. Modelling of structure-property correlations, production via mechanical nanoalloying and characterization of intermetallic and metallic glass nanoalloys. Ankara: Middle East Technical University.

AMBLARD, J., BELLONI, J. & PLATZER, O. 1991. Radiolytic synthesis and electrocatalytic activity of bimetallic nanoaggregates grafted onto various electrodes. *de Chimie Physique et de Physico-Chimie Biologique,* 88**,** 835.

ANDREWS, M. P. & O'BRIEN, S. C. 1992. Gas-phase "molecular alloys" of bulk immiscible elements: iron-silver (FexAgy). *The Journal of Physical Chemistry,* 96**,** 8233-8241.

BALETTO, F. & FERRANDO, R. 2005. Structural properties of nanoclusters: Energetic, thermodynamic, and kinetic effects. *Reviews of Modern Physics,* 77**,** 371-423.

BALETTO, F., MOTTET, C. & FERRANDO, R. 2003. Growth of Three-Shell Onionlike Bimetallic Nanoparticles. *Physical Review Letters,* 90**,** 135504.

BARCARO, G., FORTUNELLI, A., ROSSI, G., NITA, F. & FERRANDO, R. 2006. Electronic and Structural Shell Closure in AgCu and AuCu Nanoclusters. *The Journal of Physical Chemistry B,* 110**,** 23197-23203.

BEKE, D. L., BAKKER, H. & LOEFF, P. I. 1991a. On the elastic mismatch in the order-disorder transformation and solid state amorphization of intermetallic compounds—II. Criteria for the solid-amorphous transformation in intermetallic compounds. *Acta Metallurgica et Materialia,* 39**,** 1267-1273.

BEKE, D. L., LOEFF, P. I. & BAKKER, H. 1991b. On the elastic mismatch in the order-disorder transformation and solid state amorphization of intermetallic

compounds—I. Estimation of the elastic mismatch energy during order-disorder transition. *Acta Metallurgica et Materialia,* 39**,** 1259-1266.

BELLONI, J. & MOSTAFAVI, M. 2008. Radiation-Induced Metal Clusters. Nucleation Mechanism and Chemistry. *Metal Clusters in Chemistry.* Wiley-VCH Verlag GmbH.

BELLONI, J., MOSTAFAVI, M., REMITA, H., MARIGNIER, J.-L. & MARIE-ODILE DELCOURT, A. 1998. Radiation-induced synthesis of mono- and multi-metallic clusters and nanocolloids. *New Journal of Chemistry,* 22**,** 1239-1255.

BINDER, W. H. 2005. Supramolecular Assembly of Nanoparticles at Liquid–Liquid Interfaces. *Angewandte Chemie International Edition,* 44**,** 5172-5175.

BINNS, C. 2001. Nanoclusters deposited on surfaces. *Surface Science Reports,* 44**,** 1-49.

BÖNNEMANN, H. & BRIJOUX, W. 1999. Potential Applications of Nanostructured Metal Colloids. *Metal Clusters in Chemistry.* Wiley-VCH Verlag GmbH.

BÖNNEMANN, H. & RICHARDS, RYAN M. 2001. Nanoscopic Metal Particles − Synthetic Methods and Potential Applications. *European Journal of Inorganic Chemistry,* 2001**,** 2455-2480.

BOZZOLO, G., FERRANTE, J., NOEBE, R. D., GOOD, B., HONECY, F. S. & ABEL, P. 1999. Surface segregation in multicomponent systems: Modeling of surface alloys and alloy surfaces. *Computational Materials Science,* 15**,** 169-195.

BRADLEY, J. S., VIA, G. H., BONNEVIOT, L. & HILL, E. W. 1996. Infrared and EXAFS Study of Compositional Effects in Nanoscale Colloidal Palladium−Copper Alloys. *Chemistry of Materials,* 8**,** 1895-1903.

BRAUNSTEIN, P., ORO, L. A. & RAITHBY, P. R. 1999. *Metal Clusters in Chemistry;,* Weinheim,, Wiley-VCH.

BRAUNSTEIN, P. & ROSÉ, J. 2008. Heterometallic Clusters in Catalysis. *Metal Clusters in Chemistry.* Wiley-VCH Verlag GmbH.

BRAYNER, R., CORADIN, T., FIEVET-VINCENT, F., LIVAGE, J. & FIEVET, F. 2005. Algal polysaccharide capsule-templated growth of magnetic nanoparticles. *New Journal of Chemistry,* 29**,** 681-685.

BROGLIA, R. A. 1994. The colour of metal clusters and of atomic nuclei. *Contemporary Physics,* 35**,** 95-104.

BURDA, C., CHEN, X., NARAYANAN, R. & EL-SAYED, M. A. 2005. Chemistry and Properties of Nanocrystals of Different Shapes. *Chemical Reviews,* 105**,** 1025-1102.

CANXIA, K., WEIPING, C., CUNCHENG, L., LIDE, Z. & HOFMEISTER, H. 2003. Ultrasonic synthesis and optical properties of Au/Pd bimetallic nanoparticles in ethylene glycol. *Journal of Physics D: Applied Physics,* 36**,** 1609.

CAO, G. 2004. *Nanostructures and Nanomaterials*, Imperial College Press.

CHAKK, Y., BERGER, S., WEISS, B. Z. & BROOK-LEVINSON, E. 1994. Solid state amorphization by mechanical alloying—An atomistic model. *Acta Metallurgica et Materialia,* 42**,** 3679-3685.

CHENG, D., WANG, W. & HUANG, S. 2006. The Onion-Ring Structure for Pd−Pt Bimetallic Clusters. *The Journal of Physical Chemistry B,* 110**,** 16193-16196.

CHENG, Y. & SCHIFFRIN, D. J. 1996. Electrodeposition of metallic gold clusters at the water/1,2-dichloroethane interface. *Journal of the Chemical Society, Faraday Transactions,* 92**,** 3865-3871.

COTTANCIN, E., LERMÉ, J., GAUDRY, M., PELLARIN, M., VIALLE, J. L., BROYER, M., PRÉVEL, B., TREILLEUX, M. & MÉLINON, P. 2000. Size effects in the optical properties of Au_{n}Ag_{n} embedded clusters. *Physical Review B,* 62**,** 5179-5185.

COWLAM, N. & CARR, G. E. 1985. Magnetic and structural properties of Fe-B binary metallic glasses. II. Magnetic neutron scattering experiments. *Journal of Physics F: Metal Physics,* 15**,** 1117.

DARBY, S., MORTIMER-JONES, T. V., JOHNSTON, R. L. & ROBERTS, C. 2002. Theoretical study of Cu–Au nanoalloy clusters using a genetic algorithm. *The Journal of Chemical Physics,* 116**,** 1536-1550.

DE HEER, W. A. 1993. The physics of simple metal clusters: experimental aspects and simple models. *Reviews of Modern Physics,* 65**,** 611-676.

DELOGU, F. 2010. A numerical investigation of the stability of nanometer-sized amorphous structures. *Intermetallics,* 18**,** 809-814.

DENG, J.-F., LI, H. & WANG, W. 1999. Progress in design of new amorphous alloy catalysts. *Catalysis Today,* 51**,** 113-125.

DUAN, Y. & KOLLMAN, P. A. 1998. Pathways to a Protein Folding Intermediate Observed in a 1-Microsecond Simulation in Aqueous Solution. *Science,* 282**,** 740-744.

DYSON, P. J. & MCINDOE, J. S. 2000. *Transition Metal Carbonyl Chemistry;,* Amsterdam, , Gordon & Breach: .

ECKERT, J., HOLZER, J., KRILL III, C. & JOHNSON, W. 1992. *Mater Sci Forum* 88-90**,** 505-12.

EGAMI, T. & WASEDA, Y. 1984. Atomic size effect on the formability of metallic glasses. *Journal of Non-Crystalline Solids,* 64**,** 113-134.

ERMAKOV, A., BARINOV, V. & YURCHIKOV, E. 1982. *Phys Met Metallogr,* 54**,** 90-96.

ERMAKOV, A., YURCHIKOV, E. & BARINOV, V. 1981. *Phys Met Metallogr,* 52**,** 50-8.

ESUMI, K., TANO, T., TORIGOE, K. & MEGURO, K. 1990. Preparation and characterization of bimetallic palladium-copper colloids by thermal decomposition of their acetate compounds in organic solvents. *Chemistry of Materials,* 2**,** 564-567.

FARADAY, M. 1857. The Bakerian Lecture: Experimental Relations of Gold (and Other Metals) to Light. *Philosophical Transactions of the Royal Society of London,* 147**,** 145-181.

FERNÁNDEZ BARQUÍN, L., YEDRA, A., KAUL, S. N., FDEZ-GUBIEDA, M. L., MOSSELMANS, J. F. W. & PANKHURST, Q. A. 2007. X-ray absorption analysis of core/shell magnetic (Fe;Co)–B nanoparticles of amorphous and crystalline structure obtained by chemical reduction. *Journal of Non-Crystalline Solids,* 353**,** 733-737.

FERRANDO, R., JELLINEK, J. & JOHNSTON, R. L. 2008. Nanoalloys: From Theory to Applications of Alloy Clusters and Nanoparticles. *Chemical Reviews,* 108**,** 845-910.

FERRER, D., TORRES-CASTRO, A., GAO, X., SEPÚLVEDA-GUZMÁN, S., ORTIZ-MÉNDEZ, U. & JOSÉ-YACAMÁN, M. 2007. Three-Layer Core/Shell Structure in Au−Pd Bimetallic Nanoparticles. *Nano Letters,* 7**,** 1701-1705.

FROMEN, M. C., MORILLO, J., CASANOVE, M. J. & LECANTE, P. 2006. Structure and chemical order in Co–Rh nanoparticles. *EPL (Europhysics Letters),* 73**,** 885.

GAFFET, E., FAUDOT, F. & HARMELIN, M. 1992. Metastable Phase Transition Induced by Ball-Milling in the Ge-Si System. *Materials Science Forum,* 88-90**,** 375-382.

HABERLAND, H. 1994. *Clusters of Atoms and Molecules*, Springer.

HARIKUMAR, K. R., GHOSH, S. & RAO, C. N. R. 1997. X-ray Photoelectron Spectroscopic Investigations of Cu−Ni, Au−Ag, Ni−Pd, and Cu−Pd Bimetallic Clusters†. *The Journal of Physical Chemistry A,* 101**,** 536-540.

HENGLEIN, A. & GIERSIG, M. 1994. Radiolytic Formation of Colloidal Tin and Tin-Gold Particles in Aqueous Solution. *The Journal of Physical Chemistry,* 98**,** 6931-6935.

HOANG, V. V. & DUY, T. P. 2011. Structural defects and thermodynamics of vitreous GeO2 nanoparticles. *Current Applied Physics,* 11**,** 303-310.

HOANG, V. V. & ODAGAKI, T. 2011. Glass Formation and Thermodynamics of Supercooled Monatomic Liquids. *The Journal of Physical Chemistry B,* 115**,** 6946-6956.

HOCKNEY, R. W. & EASTWOOD, J. W. 2010. *Computer Simulation Using Particles*, Taylor & Francis.

ISHIDA, T. N. A. K. 1990. Binary alloy phase diagrams. *ASM International,* Volume 2. .

JAYASURIYA, K. D., CAMPBELL, S. J., CALKA, A. & JING, J. 1993. A Mössbauer study of ball-milled CoFeSiB: II: with surfactants. *Nuclear*

Instruments and Methods in Physics Research Section B: Beam Interactions with Materials and Atoms, 76**,** 85-88.

JELLINEK, J. & KRISSINEL, E. B. 1996. NinAlm alloy clusters: analysis of structural forms and their energy ordering. *Chemical Physics Letters,* 258**,** 283-292.

JIANG, Z., YANG, H., WEI, Z., XIE, Z., ZHONG, W. & WEI, S. 2005. Catalytic properties and structures of nano-amorphous Ni–B alloys affected by annealing temperatures. *Applied Catalysis A: General,* 279**,** 165-171.

JING, J., CALKN, A. & CAMPBELL, S. J. 1991. Mechanical alloying of Fe-B. *Journal of Physics: Condensed Matter,* 3**,** 7413.

JING, J., KRÄMER, A., BIRRINGER, R., GLEITER, H. & GONSER, U. 1989. Modified atomic structure in a PdFeSi nanoglass: A Mössbauer study. *Journal of Non-Crystalline Solids,* 113**,** 167-170.

JOHNSON, B. F. G. 1980. *Transition Metal Clusters* New York, Wiley.

JOHNSTON, R. L. 1998. The development of metallic behaviour in clusters. *Philosophical Transactions of the Royal Society of London. Series A: Mathematical, Physical and Engineering Sciences,* 356**,** 211-230.

JOHNSTON, R. L. 2002. *Atomic and Molecular Clusters,* London, , Taylor and Francis.

JONES, R. A. L. 2003. - Amorphous materials: Glasses with liquid-like surfaces. - 2**,** - 646\\.

JORTNER, J. 1992. Cluster size effects. *Zeitschrift für Physik D Atoms, Molecules and Clusters,* 24**,** 247-275.

KACZMAREK, W. A., BRAMLEY, R., CALKA, A. & NINHAM, B. W. 1990. Magnetic properties of $Co_{70.4}Fe_{4.6}Si_{15}B_{10}$ surfactant assisted ball milled amorphous powders. *Magnetics, IEEE Transactions on,* 26**,** 1840-1842.

KAPFENBERGER C., A. B., PÃ¶TTGEN R. AND HUPPERTZ H. 2006. *Zeitschrift fuer Kristallographie* (149,1979-) 221, 477 - 481.

KIRKPATRICK, E. M., MAJETICH, S. A. & MCHENRY, M. E. 1996. Magnetic properties of single domain samarium cobalt nanoparticles. *Magnetics, IEEE Transactions on,* 32**,** 4502-4504.

KLIMOV, V. I. 2007. Spectral and Dynamical Properties of Multiexcitons in Semiconductor Nanocrystals. *Annual Review of Physical Chemistry,* 58**,** 635-673.

KNUTH, D. E. 1973. *The Art of Computer Programming, 1: Fundamental Algorithms*, Addison-Wesley.

KOLB, U., QUAISER, S. A., WINTER, M. & REETZ, M. T. 1996. Investigation of Tetraalkylammonium Bromide Stabilized Palladium/Platinum Bimetallic Clusters Using Extended X-ray Absorption Fine Structure Spectroscopy. *Chemistry of Materials,* 8**,** 1889-1894.

KRISSINEL, E. B. & JELLINEK, J. 1997a. 13-atom Ni-Al alloy clusters: Structures and dynamics. *International Journal of Quantum Chemistry,* 62**,** 185-197.

KRISSINEL, E. B. & JELLINEK, J. 1997b. 13-Atom NiAl alloy clusters: correlation between structural and dynamical properties. *Chemical Physics Letters,* 272**,** 301-312.

KUNZ, H. R. & GRUVER, G. A. 1975. The Catalytic Activity of Platinum Supported on Carbon for Electrochemical Oxygen Reduction in Phosphoric Acid. *Journal of The Electrochemical Society,* 122**,** 1279-1287.

LATA RAO, M. & SUNDAR MANOHARAN, S. 2004. Magnetism and magneto-transport studies in sonochemically prepared amorphous Co100−xPtx nano alloys. *Solid State Communications,* 129**,** 781-784.

LEE, S.-P. & CHEN, Y.-W. 1999. Selective Hydrogenation of Furfural on Ni−P, Ni−B, and Ni−P−B Ultrafine Materials. *Industrial & Engineering Chemistry Research,* 38**,** 2548-2556.

LI, H., LI, H., DAI, W. & QIAO, M. 2003. Preparation of the Ni-B amorphous alloys with variable boron content and its correlation to the hydrogenation activity. *Applied Catalysis A: General,* 238**,** 119-130.

LI, H., LIU, J., XIE, S., QIAO, M., DAI, W. & LI, H. 2008. Highly active Co–B amorphous alloy catalyst with uniform nanoparticles prepared in oil-in-water microemulsion. *Journal of Catalysis,* 259**,** 104-110.

LI, H., ZHAO, Q., WAN, Y., DAI, W. & QIAO, M. 2006. Self-assembly of mesoporous Ni–B amorphous alloy catalysts. *Journal of Catalysis,* 244**,** 251-254.

LIU, H. B., CANIZAL, G., SCHABES-RETCHKIMAN, P. S. & ASCENCIO, J. A. 2006. Structural Selection and Amorphization of Small Ni−Ti Bimetallic Clusters. *The Journal of Physical Chemistry B,* 110**,** 12333-12339.

LIU, W. & MCCORMICK, P. G. 1999. Synthesis of Sm2Co17 alloy nanoparticles by mechanochemical processing. *Journal of Magnetism and Magnetic Materials,* 195**,** L279-L283.

LLOYD, J. R. & LOVLEY, D. R. 2001. Microbial detoxification of metals and radionuclides. *Current Opinion in Biotechnology,* 12**,** 248-253.

LORDEIRO, R. A., GUIMARÃES, F. F., BELCHIOR, J. C. & JOHNSTON, R. L. 2003. Determination of main structural compositions of nanoalloy clusters of CuxAuy (x + y ≤ 30) using a genetic algorithm approach. *International Journal of Quantum Chemistry,* 95**,** 112-125.

LUTFUL, M. A., KULDIP, R. & RONALD, E. R. 1999. *Method for manufacturing oil-based ferrofluid.*

MABBETT, A. N. & MACASKIE, L. E. 2002. A new bioinorganic process for the remediation of Cr(VI). *Journal of Chemical Technology & Biotechnology,* 77**,** 1169-1175.

MACASKIE, L. E., BAXTER-PLANT, V. S., CREAMER, N. J., HUMPHRIES, A. C., MIKHEENKO, I. P., MIKHEENKO, P. M., PENFOLD, D. W. & YONG, P. 2005 Applications of bacterial hydrogenases in waste decontamination, manufacture of novel bionanocatalysts and in sustainable energy. *Biochemical Society Transactions* 33**,** 76–79.

MANN, S. 1996. *Biomimetic Materials Chemistry,* New York,, VCH.

MANN, S. 2001. *Biomineralization: Principles and Concepts in Bioinorganic Materials Chemistry,* Oxford,, Oxford University Press.

MARTIN, T. P. E. 1996. *Large Clusters of Atoms and Molecules,* Dordrecht,, Kluwer.

MASSOBRIO, C. 1990. MOLECULAR DYNAMICS STUDY OF AMORPHIZATION INDUCED BY CHEMICAL DISORDER IN CRYSTALLINE NiZr2. *J. Phys. Colloques,* 51**,** C4-55-C4-61.

MATTEI, G., MAURIZIO, C., MAZZOLDI, P., D'ACAPITO, F., BATTAGLIN, G., CATTARUZZA, E., DE JULIÁN FERNÁNDEZ, C. & SADA, C. 2005. Dynamics of compositional evolution of Pd-Cu alloy nanoclusters upon heating in selected atmospheres. *Physical Review B,* 71**,** 195418.

MERBACH, A. E. & TOTH, E. 2001. *The Chemistry of Contrast Agents in Medical Magnetic Resonance Imaging*, Wiley.

MERTIG, M., WAHL, R., LEHMANN, M., SIMON, P. & POMPE, W. 2001. Formation and manipulation of regular metallic nanoparticle arrays on bacterial surface layers: an advanced TEM study. *The European Physical Journal D - Atomic, Molecular, Optical and Plasma Physics,* 16**,** 317-320.

MILANI, P. & IANNOTTA, S. 1999. *Cluster Beam Synthesis of Nanostructured Materials,* Berlin,, Springer.

MINGOS, D. M. P. & WALES, D. J. 1990. *Introduction to Cluster Chemistry;*

, Englewood Cliffs, NJ, Prentice Hall:.

MIZUKOSHI, Y., FUJIMOTO, T., NAGATA, Y., OSHIMA, R. & MAEDA, Y. 2000. Characterization and Catalytic Activity of Core−Shell Structured Gold/Palladium Bimetallic Nanoparticles Synthesized by the Sonochemical Method. *The Journal of Physical Chemistry B,* 104**,** 6028-6032.

MOLENBROEK, A. M., HAUKKA, S. & CLAUSEN, B. S. 1998. Alloying in Cu/Pd Nanoparticle Catalysts. *The Journal of Physical Chemistry B,* 102**,** 10680-10689.

MURTY, B., NAIK, M., RAO, M. M. & RANGANATHAN, S. 1992. Glass forming composition range in the Al-Ti system by mechanical alloying. *Materials Forum,* 16**,** 19-26.

OKAMOTO, Y., NITTA, Y., IMANAKA, T. & TERANISHI, S. 1979. Surface characterisation of nickel boride and nickel phosphide catalysts by X-ray photoelectron spectroscopy. *Journal of the Chemical Society, Faraday Transactions 1: Physical Chemistry in Condensed Phases,* 75**,** 2027-2039.

OMURO, K. & HIROMI, M. 1995. Amorphization of Mechanically Alloyed Fe-C and Fe-N Materials with Additive Elements and their Concentration Dependence. *Materials Science Forum,* 179-181**,** 273-280.

PANKHURST, Q. A., BARQUÍN, L. F., WICKS, J. D., MCGREEVY, R. L. & GIBBS, M. R. J. 1997. Structural and magnetic anisotropy in amorphous alloy ribbons. *Journal of Physics: Condensed Matter,* 9**,** L375.

PAPELL, S. S. 1965. *Low viscosity magnetic fluid obtained by the colloidal suspension of magnetic particles.*

PETER, J. G., HUMPHREYS, F. J., RICHARD, B. & BEANLAND, R. 2001. *Electron Microscopy and Analysis*, Taylor & Francis.

PLATT, M. & DRYFE, R. A. W. 2005. Structural and electrochemical characterisation of Pt and Pd nanoparticles electrodeposited at the liquid/liquid interface: Part 2. *Physical Chemistry Chemical Physics,* 7**,** 1807-1814.

PLATT, M., DRYFE, R. A. W. & ROBERTS, E. P. L. 2002. Controlled deposition of nanoparticles at the liquid-liquid interface. *Chemical Communications***,** 2324-2325.

R. BELLISSENT, G. G., T. HYEON, S.M AGAZU, D. MAJOLINO, P. MIGLIARDO' AND K. S . SUSLICK 1995. Structural properties of amorphous bulk Fe, Co and Fe-Co binary alloys. *Physica Scripta,* T57**,** .

RAJESH, B., SASIREKHA, N., CHEN, Y.-W. & LEE, S.-P. 2007. Effect of Synthesis Parameters on the Characteristics of Fe−B Nanoalloys for Dehydrogenation of Ethanol. *Industrial & Engineering Chemistry Research,* 46**,** 2034-2041.

RAJESH, B., SASIREKHA, N., LEE, S.-P., KUO, H.-Y. & CHEN, Y.-W. 2008a. Investigation of Fe-P-B ultrafine amorphous nanomaterials: Influence of synthesis parameters on physicochemical and catalytic properties. *Journal of Molecular Catalysis A: Chemical,* 289**,** 69-75.

RAJESH, B., SASIREKHA, N., LEE, S.-P., KUO, H.-Y. & CHEN, Y.-W. 2008b. Investigation of Fe–P–B ultrafine amorphous nanomaterials: Influence of synthesis parameters on physicochemical and catalytic properties. *Journal of Molecular Catalysis A: Chemical,* 289**,** 69-75.

RAJESH, C. & MAJUMDER, C. 2006. Energy level reordering and stability of MPb12 clusters: An interplay between geometry and electronic structure. *Chemical Physics Letters,* 430**,** 101-107.

116

RAO, C. N. R., KULKARNI, G. U., THOMAS, P. J. & EDWARDS, P. P. 2000. Metal nanoparticles and their assemblies. *Chemical Society Reviews,* 29**,** 27-35.

REETZ, M. T., HELBIG, W. & QUAISER, S. A. 1995. Electrochemical Preparation of Nanostructural Bimetallic Clusters. *Chemistry of Materials,* 7**,** 2227-2228.

REMITA, S., MOSTAFAVI, M. & DELCOURT, M. O. 1996. Bimetallic AgPt and AuPt aggregates synthesized by radiolysis. *Radiation Physics and Chemistry,* 47**,** 275-279.

ROSENSWEIG, R. E. 1970. *Method of substituting one ferrofluid solvent for another*.

ROSSI, G., RAPALLO, A., MOTTET, C., FORTUNELLI, A., BALETTO, F. & FERRANDO, R. 2004. Magic Polyicosahedral Core-Shell Clusters. *Physical Review Letters,* 93**,** 105503.

RUBAN, A. V., SKRIVER, H. L. & NØRSKOV, J. K. 1999. Surface segregation energies in transition-metal alloys. *Physical Review B,* 59**,** 15990-16000.

RUSSELL, A. E. & ROSE, A. 2004. X-ray Absorption Spectroscopy of Low Temperature Fuel Cell Catalysts. *Chemical Reviews,* 104**,** 4613-4636.

SCHMID, G. 1999. Nanosized Clusters on and in Supports — Perspectives for Future Catalysis. *Metal Clusters in Chemistry.* Wiley-VCH Verlag GmbH.

SCHMID, G. 2005. General Introduction. *Nanoparticles.* Wiley-VCH Verlag GmbH & Co. KGaA.

SCHMID, G. & 1994. *Clusters and Colloids: From Theory to Applications; ,* Weinheim, , VCH:.

SCHMID, G., LEHNERT, A., MALM, J.-O. & BOVIN, J.-O. 1991. Ligand-Stabilized Bimetallic Colloids Identified by HRTEM and EDX. *Angewandte Chemie International Edition in English,* 30**,** 874-876.

SCHWARZ, R. B. & JOHNSON, W. L. 1983. Formation of an Amorphous Alloy by Solid-State Reaction of the Pure Polycrystalline Metals. *Physical Review Letters,* 51**,** 415-418.

SHEN, J., ZHANG, Q., LI, Z. & CHEN, Y. 1996. Chemical reaction for the preparation of Ni-P ultrafine amorphous alloy particles from aqueous solution. *Journal of Materials Science Letters,* 15**,** 715-717.

SINFELT, J. H. 1973. Supported "bimetallic cluster" catalysts. *Journal of Catalysis,* 29**,** 308-315.

SINFELT, J. H. 1983. *Bimetallic Catalysts: Discoveries, Concepts, and Applications,* New York, Wiley.

SOPU, D., ALBE, K., RITTER, Y. & GLEITER, H. 2009. From nanoglasses to bulk massive glasses. AIP.

SRIVASTAVA, S., SAMANTA, B., ARUMUGAM, P., HAN, G. & ROTELLO, V. M. 2007. DNA-mediated assembly of iron platinum (FePt) nanoparticles. *Journal of Materials Chemistry,* 17**,** 52-55.

STACHURSKI, Z. H. 2003. Strength and deformation of rigid polymers: structure and topology in amorphous polymers. *Polymer,* 44**,** 6059-6066.

STILLINGER, F. H. 1995. A Topographic View of Supercooled Liquids and Glass Formation. *Science,* 267**,** 1935-1939.

STONEHART, P. 1992. Development of alloy electrocatalysts for phosphoric acid fuel cells (PAFC). *Journal of Applied Electrochemistry,* 22**,** 995-1001.

SUMIYAMA, K., SUZUKI, K., MAKHLOUF, S. A., WAKOH, K., KAMIYAMA, T., YAMAMURO, S., KONNO, T. J., XU, Y. F., SAKURAI, M. & HIHARA, T. 1995. Structural evolution and magnetic properties of nano-granular metallic alloys. *Journal of Non-Crystalline Solids,* 192–193**,** 539-545.

SURYANARAYANA, C. 2001. Mechanical alloying and milling. *Progress in Materials Science,* 46**,** 1-184.

TAJIMA, S., HATTORI, T. & KATO, Y. 1995. Influence of milling conditions on magnetic properties of $Sm_2Fe_{17}N_3$ particles. *Magnetics, IEEE Transactions on,* 31**,** 3701-3703.

THOMAS, J. M., JOHNSON, B. F. G., RAJA, R., SANKAR, G. & MIDGLEY, P. A. 2002. High-Performance Nanocatalysts for Single-Step Hydrogenations. *Accounts of Chemical Research,* 36**,** 20-30.

TORIGOE, K. & ESUMI, K. 1993. Preparation of bimetallic silver-palladium colloids from silver(I) bis(oxalato)palladate(II). *Langmuir,* 9**,** 1664-1667.

TOSHIMA, N. & YONEZAWA, T. 1998. Bimetallic nanoparticles-novel materials for chemical and physical applications. *New Journal of Chemistry,* 22**,** 1179-1201.

TREGUER, M., DE COINTET, C., REMITA, H., KHATOURI, J., MOSTAFAVI, M., AMBLARD, J., BELLONI, J. & DE KEYZER, R. 1998. Dose Rate Effects on Radiolytic Synthesis of Gold−Silver Bimetallic Clusters in Solution. *The Journal of Physical Chemistry B,* 102**,** 4310-4321.

TURKEVICH, J., STEVENSON, P. C. & HILLIER, J. 1951. A study of the nucleation and growth processes in the synthesis of colloidal gold. *Discussions of the Faraday Society,* 11**,** 55-75.

UL HAQ, I. & MATIJEVIĆ, E. 1998. Preparation and properties of uniform coated inorganic colloidal particles. 12. Tin and its compounds on hematite. *In:* LAGALY, G. (ed.) *Horizons 2000 – aspects of colloid and interface science at the turn of the millenium.* Steinkopff.

V. GOIA, D. & MATIJEVIC, E. 1998. Preparation of monodispersed metal particles. *New Journal of Chemistry,* 22**,** 1203-1215.

VAN HOANG, V., ODAGAKI, T. & ENGEL, M. 2008. Cooling rate effects on structure and thermodynamics of amorphous nanoparticles. *Applied Surface Science,* 254**,** 7531-7534.

VARDEMAN, C. F. & GEZELTER, J. D. 2008. Simulations of Laser-Induced Glass Formation in Ag−Cu Nanoparticles. *The Journal of Physical Chemistry C,* 112**,** 3283-3293.

VERLET, L. 1967. - Computer "Experiments" on Classical Fluids. I. Thermodynamical Properties of Lennard-Jones Molecules. - 159**,** - 103.

WANG, C.-B. & ZHANG, W.-X. 1997. Synthesizing Nanoscale Iron Particles for Rapid and Complete Dechlorination of TCE and PCBs. *Environmental Science & Technology,* 31**,** 2154-2156.

WANG, J., JOHNSTON-PECK, A. C. & TRACY, J. B. 2009. Nickel Phosphide Nanoparticles with Hollow, Solid, and Amorphous Structures. *Chemistry of Materials,* 21**,** 4462-4467.

WATZKY, M. A. & FINKE, R. G. 1997. Nanocluster Size-Control and "Magic Number" Investigations. Experimental Tests of the "Living-Metal Polymer" Concept and of Mechanism-Based Size-Control Predictions Leading to the Syntheses of Iridium(0) Nanoclusters Centering about Four Sequential Magic Numbers†. *Chemistry of Materials,* 9**,** 3083-3095.

WEN, M., LI, L.-J., LIU, Q., QI, H.-Q. & ZHANG, T. 2008. The preparation of well-dispersed Ni–B amorphous alloy nanoparticles at room temperature. *Journal of Alloys and Compounds,* 455**,** 510-515.

WU, Z., LI, W., ZHANG, M. & TAO, K. 2007. Advances in chemical synthesis and application of metal-metalloid amorphous alloy nanoparticulate catalysts. *Frontiers of Chemical Engineering in China,* 1**,** 87-95.

XIE, S., QIAO, M., ZHOU, W., LUO, G., HE, H., FAN, K., ZHAO, T. & YUAN, W. 2005. Controlled Synthesis, Characterization, and Crystallization of Ni−P Nanospheres. *The Journal of Physical Chemistry B,* 109**,** 24361-24368.

YOSHIDA, S., YAMASHITA, H., FUNABIKI, T. & YONEZAWA, T. 1982. Hydrogenation of olefins over amorphous Ni-P and Ni-B alloys prepered by the rapid quenching method. *Journal of the Chemical Society, Chemical Communications***,** 964-965.

ZHANG, H. 1993. The quantification of criteria for predicting glass formation of binary transition metals by mechanical alloying. *Journal of Physics: Condensed Matter,* 5**,** L337.